Chapter 2

Electrodeposition of Graphitic Carbon Nitride (gCN) & gCN.MnO_2 Composite for investigating Electrocatalytic Dopamine oxidation.

This chapter investigates the electrodeposition of graphitic carbon nitride (gCN) and its further modification with MnO_2 to enhance the electrocatalytic activity. While the electrodeposition of gCN yields limited improvements in catalytic efficiency, significant enhancement is achieved through co-deposition with manganese dioxide (MnO_2). This chapter is organized into two primary sections, detailing two different modification methods and resulting outcomes.

In the first section, gCN is co-electrodeposited with manganese acetate in an in-situ process to form a composite of gCN.MnO_2 directly on the electrode surface. The resulting gCN.MnO_2 modified electrode demonstrates superior electrocatalytic activity compared to that of electrodeposited gCN or manganese acetate alone. To evaluate the catalytic efficacy of this composite, its surface was tested for dopamine electro-oxidation, which confirmed an enhanced catalytic response. Despite these promising results, the approach requires significant optimization due to practical challenges: gCN's insolubility in ethanol necessitates prolonged sonication (up to 16 hours), and handling indium tin oxide (ITO) substrates during electrodeposition introduces additional complexities.

To circumvent these limitations, the second section of this chapter presents an alternative strategy involving the direct synthesis of two gCN.Mn_xO_y composites. This approach allows for the straightforward preparation of gCN composites, minimizing the practical challenges associated with electrodeposition. These synthesized gCN.Mn_xO_γ composites are systematically characterized, electrodeposited, and evaluated for electrocatalytic performance. This alternative synthesis pathway offers a more efficient route for enhancing the catalytic capabilities of gCN, providing insights into optimized composite structures for potential electrochemical applications.

Chapter 2

First Part

2.1.1. Introduction

Graphitic carbon nitride (gCN), a polymeric metal-free semiconductor with a 2D layered structure [1], has emerged as a potential material for photo-catalysis, adsorption, energy storage [2–6] and optical and bio-chemical sensors [7–9]. gCN has been in the limelight because of its unique traits, specifically its graphene-like planar structure composed of sp^2-linked carbon and nitrogen. In addition to its impressive physicochemical stability, gCN's other benefits include its simple and inexpensive synthesis, and the ease of functionalization [10].

Furthermore, the N-rich triazine structural units with pyridinic and graphitic N species endows gCN with multiple electron donor sites for chemical and biological interactions. However, the poor conductivity and impeded charge transfer of gCN limits its application in electrochemical domains [11]. Several strategies have been opted to tune gCN for electrochemical applications to overcome the associated shortcomings. A significant improvement can be observed by tailoring the topography of bulk gCN. The improved photocatalytic and electrochemical properties have been previously achieved by exfoliating bulk gCN into nanosheets with smaller crystal sizes, increased surface area, and more defects [12,13]. In another approach, the chemical and physical characteristics of gCN are tailored by making its composites with metal oxide [14–16], carbon-based materials [17], and conducting polymer [18]. Engineering hybrid composites of gCN with localized heterojunction by constructing hierarchical porous and nano/micro-structures of chemically different components can substantially increase the surface area and facilitate charge transport characteristics. Transition metal oxides are specifically beneficial for electrochemical applications owing to the variety of structural diversity and various chemical oxidation states, which can promote redox reactions. Manganese is one of the transition metals that has garnered much attention due to its distinctive polymorphs

and associated properties. MnO_2, Mn_2O_3, Mn_3O_4, Mn_5O_8, MnOOH, and amorphous MnOx are some of the different types of manganese oxide (MnOx). Past literature reports MnO_X polymorphs as potential material for supercapacitors, electrochemical sensors, and photocatalytic reactions due to their low cost and abundant natural reserves [19–21]. However, MnO_2 typically exhibits modest levels of electrochemical activity, likely because of the material's poor interfacial contact, retarded electrical conductivity, super capacitive nature & formation of the electric double layer. Also, it often aggregates severely or even collapses when used alone, leading to inferior electrochemical performance, which greatly confines its widespread practical applications. Nevertheless, MnO_2 is known to be a great electron acceptor and thus is industrially relevant for aiding the oxidation of many organic molecules.

To deal with the associated problems of MnO_2 and gCN, herein, this manuscript introduces a synergistic combination of gCN.MnO_2 especially tailored for sensitive and selective voltammetric sensors for investigating biomolecule oxidation. In the synergistic combination, gCN will act as a 2D host structure providing an interface for MnO_2 nucleation. The lone pair of N in gCN layers will have an affinity for interaction with MnO_2 and thus is expected to result in stable composite formation[22,23]. On the other hand, MnO_2 will electrocatalyze the oxidation of biomolecules preferentially interacting with π-conjugated electrons of the gCN. Henceforth, in this work, we propose an unconventional approach to electrodeposit gCN on a conducting substrate and its *in*-situ decoration with MnO_2 nanostructures. To the best of our knowledge, this is the first systematic report to study and decipher the step-by-step mechanistic of gCN.MnO_2 electro-polymerization/deposition and its effect on the electrochemical performance. For meaningful voltammetric responses in terms of electrocatalytic ability and increased sensitivity, the formation of uniformly modified surfaces is of utmost importance.

Conventional drop cast method leads to uncontrolled surface accumulation of bulk materials, particle agglomeration, coffee rings, cracks during solvent evaporation there by causing the inhomogeneity in particle distribution[24,25]. In contrast to the previously used drop-casting method, the proposed electrodeposition strategy utilizes in-situ electrochemical exfoliation and surface functionalization resulting in uniform deposition of composites on the electrode surface with precise control over thickness. The electrodeposited films are expected to showcase better reproducibility since no drop is being cast on the electrode surface attenuating both the human error incurred during casting a sessile drop and anisotropy created during solvent evaporation.

For practical applicability of the designed electrode interface, the gCN.MnO_2 functionalized electrode has been used for sensing dopamine, one of the essential catecholamine neurotransmitters, as the test case. DA is a member of the family of excitatory chemical neurotransmitters [26]. It plays a vital role in communicating information between neurons relevant to attention, learning, cognition, memory, motion control, sleep, blood pressure regulation, and emotion [27,28]. It is significant to note that variations from healthy, normal levels of DA (10-1000 nM) [29,30] in urine and other body fluids might have symptoms of several disorders. A low DA level has been closely linked to illnesses including Parkinson's disease, bronchial asthma, anorexia, schizophrenia, attention deficit hyperactivity disorder (ADHD), Alzheimer's disease, Huntington’s disease, restless legs syndrome (RLS), and HIV infection[31–35]. These disorders can be minimized by external medicine like L-DOPA which also poses a threat of Dopamine overdose and it clinical implications [36]. However, because DA functions as a neurotransmitter associated with addiction and performance, use of illegal drugs for eventually increasing DA levels is also known in drug addiction cases which poses increased risk of depression,

hypertension, and aggressive crimes. It is well recognized that DA is an electrochemically active substance that can be electrochemically oxidized to produce dopamine-o-quinone (DAQ). As electroanalytical methods are ideal for point-of-care portable diagnostics, eliminating costly instruments setup and cumbersome processing. Consequently, electroanalytical monitoring of DA is of the utmost relevance. Therefore, the developed scaffold has been evaluated for qualitative and quantitative electrochemical analysis of dopamine.

2.1.2. Experimental

2.1.2.1 Materials

Indium tin oxide (ITO) coated glass pieces with a resistance of 18 Ω were procured from DTech Solutions (Kanpur, India). Analytical grade reagents including dopamine hydrochloride ($(HO)_2C_6H_3CH_2CH_2NH_2.HCl$), melamine ($C_3H_6N_6$), manganese (II) acetate tetrahydrate ($(CH_3COO)_2Mn.4H_2O$), ethanol (CH_3CH_2OH), potassium ferricyanide ($K_3Fe(CN)_6$), potassium chloride (KCl), uric acid ($C_5H_4N_4O_3$), melatonin ($C_{13}H_{16}N_2O_2$), dextrose anhydrous ($C_6H_{12}O_6$), sodium dihydrogen phosphate (H_2NaO_4P), ortho-phosphoric acid (H_3PO_4), disodium hydrogen phosphate (Na_2HPO_4) were purchased from Alfa Aesar. The chemicals were used as obtained without any further purification. 0.1 M Phosphate buffer was prepared following the method reported by Christian and Purdy. Deionized water from a Milli-Q ultrapure water purifier (Millipore, Billerica, MA) was used for preparing the stock solution and requisite test aliquots throughout the experimental procedures.

2.1.2.2 Synthesis of gCN

The graphitic carbon nitride (gCN) was synthesized by direct thermal polycondensation of melamine, with some modification as reported previously in the literature[37]. Briefly, 10 g of melamine powder was taken in an alumina crucible and placed inside a muffle

furnace. The furnace was progressively heated at a ramp rate of 6 ℃/min till 600 ℃, where the temperature was held constant for 6 h. After the furnace cooled down to room temperature, the crucible was taken out to collect a light-yellow coloured powder referred to as bulk gCN. The material so formed was grinded in a mortar pestle and used for further characterization.

To enhance the dispersion characteristics and surface area of the bulk gCN, its particle size was further reduced by mechanical exfoliation via ball milling. The ball milling was carried out using a Fritsch pulverisette 7 premium line planetary micro mill. A grinding bowl of 45 mL was used with 3 mm zirconia balls at 300 rpm for 10 cycles of 30 min each with 5 min pause time between the cycles. The ball-to-powder ratio of 10:1 by mass was used.

2.1.2.3 Characterization details

The crystallographic information of synthesized as well as ball-milled gCN was obtained using the X-ray Diffractometer (Rigaku miniflex 600, Japan) using Cu-ka radiation source. The surface functionalities of gCN were examined by performing Fourier-transform infrared (FTIR) spectroscopy in the wavenumber range of 550 – 4000 cm^{-1} with 4 cm^{-1} resolution using the Thermo ScientificTM Nicolet iD7 spectrometer. The surface and morphological information were extracted by employing ZEISS EVO scanning electron microscope performed at 20kV. K-Alpha, Thermo Fisher Scientific X-ray photon spectrophotometer equipped with a monochromatic Al Ka micro-focused X-ray source (100–4000 eV) was employed for elemental analysis of bare and modified electrode surfaces. Raman spectra were collected on a Research India Raman spectrometer equipped with a 785 nm laser excitation source at laser power 130 mW and an exposure time of 10s. NTEGRA Prima scanning probe microscope (NT-MDT Service & Logistics Ltd) was used to do the surface analysis.

2.1.2.4 Electrochemical measurements

A PalmSens3 voltammetric analyzer was used for all the electrochemical measurements. A three-electrode system consisting of Ag/AgCl (3M KCl), platinum wire, and ITO coated glass as the reference, counter, and working electrode, respectively, was used for all the electrochemical measurements. 1M KCl was used as a supporting electrolyte during the electrodeposition processes. The pH 7.4, phosphate buffer was used as the supporting electrolyte for all other studies.

2.1.2.4.1 Electrodeposition of gCN, MnO_2 and gCN.MnO_2 composite

Prior to electrodeposition, ITO coated glass slides were first ultrasonically cleaned in deionized water (DI), ethanol, and isopropyl alcohol. Afterward, the surface was rinsed with DI and dried in a hot-air oven maintained at 75 °C. For the electrodeposition, 5 mg/mL gCN suspension was prepared by dispersing 50 mg of ball-milled gCN in 10 mL of ethanol via bath sonication for 16 hours. From the prepared suspension, 500 uL was taken out and poured into an electrochemical cell already containing 1 mL of 1M KCl. The solution was finally made to 2 mL by adding the requisite volume of ethanol. The gCN was directly electrodeposited on the pre-cleaned ITO working electrode by scanning the potential between - 1000 mV and + 1600 mV at a scan rate of 100 $mV.s^{-1}$ in the prepared aliquot. The number of scans used for electrodeposition varied from 5 to 25 to decide the optimum number of scans required to get the desirable electrochemical response. After completing the requisite scans, the ITO was rinsed with double-distilled water and dried at room temperature. The electrodeposition protocols were optimized by measuring the CV and SWV peak current of 0.5 mM $K_3[Fe(CN)_6]$ using the gCN modified ITO prepared by varying the number of deposition CV cycles in the range of 5-25. The electrodeposited ITO is called gCN/ITO in the following text.

Similarly, the electrodeposition of MnO_2 was carried out by scanning the cyclic voltammetry potential between - 1000 mV and + 1600 mV at a scan rate of 100 $mV.s^{-1}$ in 1 mM manganese acetate solution prepared in 0.5 M KCl. The number of CV scans used for electrodeposition was optimized for attaining the best electrochemical response. For the electrodeposition of gCN.MnO_2 composite, 2 mL suspension was prepared using 500 µL of gCN, 200 µL of 10 mM manganese acetate solution, 300 µL of ethanol, and 1 mL of KCl. All the electrodeposition and optimization procedure were kept the same as used for gCN electrodeposition.

2.1.2.4.2 Electroanalytical technique and sample preparation

A comparative evaluation of the electrochemical response was used to decide the appropriate number of electrodeposition cycles. For the comparative evaluation, the cyclic voltammetric response of the individually modified scaffold was recorded from -0.2 V to +0.6 V at a scan rate of 100 mV/s in a solution composed of 1:1 volume ratio of 1 mM $K_3[Fe(CN)_6]$ and 1 M KCl.

Dopamine (DA) was taken as the test analyte for evaluating the applicability of the electrodeposited surface for voltammetric sensing applications. 5 mM stock solution of DA was prepared by dissolving the appropriate weight of solid DA in DI to conduct the qualitative and quantitative electroanalytical studies. The stock solution was stored in the dark to avoid any light-induced degradation of DA. DA solutions of different concentrations were then prepared using the dilution method. 1 mL of PB-7.4 was kept constant in all the aliquots, and the remaining 1 mL was composed of the required volume of DA stock solution and DI water. The electrochemical properties of dopamine were investigated using square wave voltammetry (SWV). The SW voltammograms were recorded in the 0 - 0.5 V voltage range, with a 6 mV step. The optimal amplitude and frequency were 25 mV and 10.0 Hz. After each SWV scan, the sensor surface was washed

with DI and stabilized by recording five SWVs in a buffer solution in the working potential range.

2.1.3. Results and Discussion

2.1.3.1 Physico-chemical characterization of the synthesised and ball-milled gCN

Several characterization techniques were employed to study the physical, chemical, and topographical characteristics of the synthesized material. The formation of gCN was first indicated from the powder X-ray diffraction (PXRD) patterns presented in **Figure 2.1.1(a).** The X-ray diffractogram of the gCN exhibited a sharp peak at ca. [38]corresponding to the (002) plane, which is the characteristic signature of the graphite-like stacked layer arrangements of the conjugated aromatic systems. Another small diffraction peak at 13.1° represents the in-plane aromatic structural packing. The d-spacing between the gCN layers was found to be ~ 0.33 nm, calculated using the theta values of the most intense peak. Furthermore, the XRD patterns of the ball-milled gCN were recorded and compared with the bulk gCN. It can be witnessed from the figure that ball-milled gCN exhibited substantially reduced peak intensities compared to bulk gCN. This manifests the pulverization and exfoliation of bulk gCN into thinner layers and smaller crystal sizes [39,40].

To further analyze the chemical structure of the bulk gCN and the changes incurred due to ball milling, Raman spectroscopy with a 785 nm excitation source was exploited. The Raman spectra of both gCN and ball-milled gCN in **Figure 2.1.1(b)** showcase peaks at 700, 760, and 1233 cm^{-1}, along with a broad band around 1412 cm^{-1}. In agreement with the FT-IR spectra, the band at 700 cm^{-1} can be assigned to the breathing mode of triazine rings, while the Raman mode at 760 cm^{-1} corresponds to the out-of-plane bending of the graphitic domain. The bands at 1233 and 1412 cm^{-1} can be assigned to C-N stretching mode [43,44]. After ball milling, all the Raman bands exhibit a slight decrease in intensity

except the one at 760 cm^{-1}. In fact, a considerable difference was observed in the relative intensity of 700 to 760 cm^{-1}. The intensity ratio I_{700}/I_{760} for ball-milled gCN was found to be 1.1 compared to 1.32 for the bulk gCN, indicating the structural perturbation and defect formation due to ball milling [44]. The perturbed crystal structure with increased defects and decreased crystal size of the ball-milled gCN was further supported by the increased full width at half maxima (FWHM) values corresponding to the peaks at 700 and 760 cm^{-1}. Both the peaks exhibited an increment of 12.5 cm^{-1} and 19.82 cm^{-1}, respectively, compared to the bulk gCN. The observations closely agree with the abovementioned XRD analysis [45].

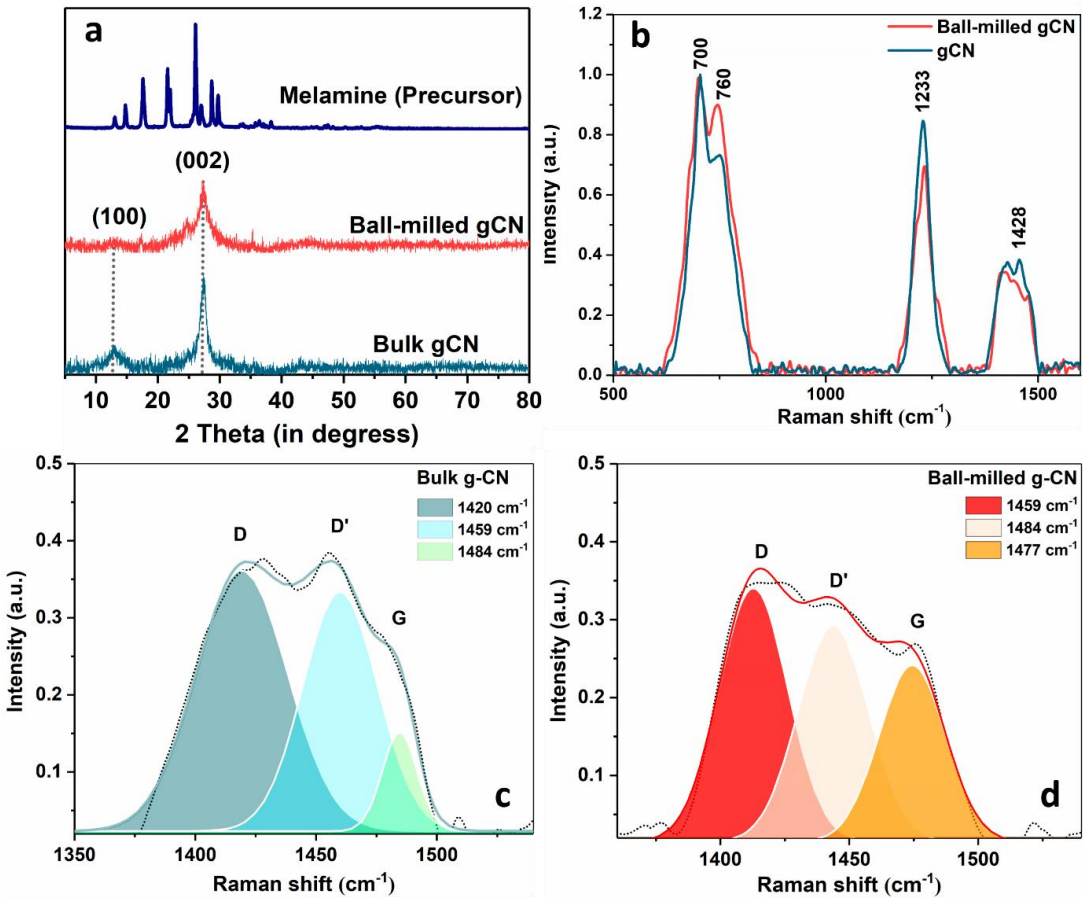

Figure 2.1.1: (a) XRD pattern of melamine, ball-milled gCN, bulk gCN. (b) Comparative Raman spectra of bulk gCN and ball-milled gCN. Deconvoluted Raman spectra of (c) bulk gCN, and (d) ball-milled gCN.

To further confirm the increased defects in the ball-milled gCN, the broad Raman bands centered at 1412 cm^{-1} were deconvoluted into distorted D and graphitic G bands (**Figure**

2.1.1(c-d)). The deconvoluted spectra of bulk gCN showcase three peaks at 1420, 1459, and 1484 cm^{-1} ascribed to the D, D', and G bands, respectively. Similar peaks were observed for the ball-milled gCN. However, the peaks were red-shifted by 8 cm^{-1} at 1412, 14 cm^{-1} at 1443, and 7 cm^{-1} at 1477 cm^{-1} compared to bulk gCN. These peculiar features univocally suggested that ball milling resulted in defect-rich and disordered gCN crystal structures.

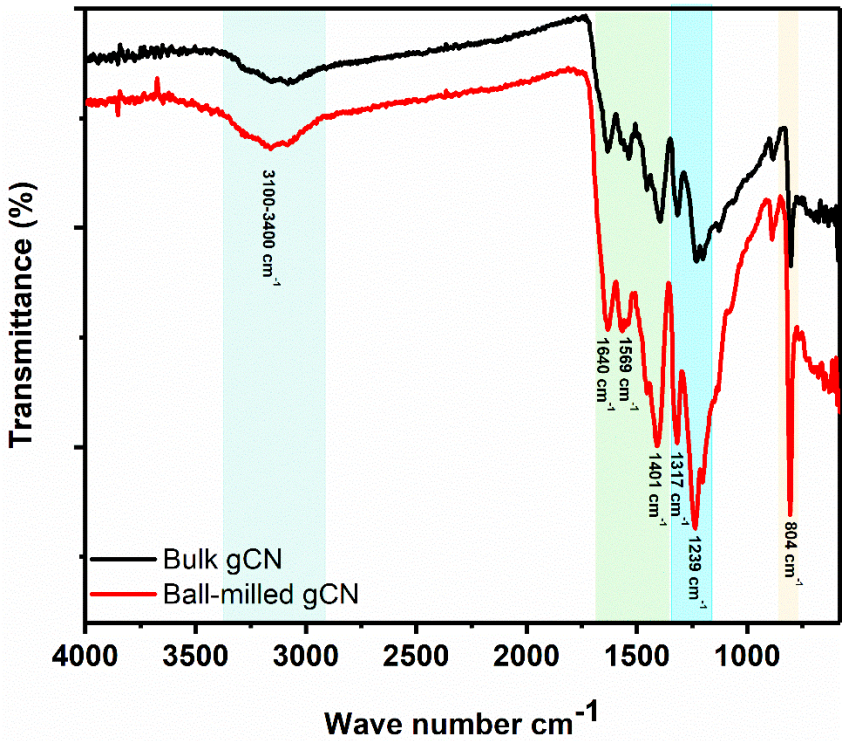

Figure 2.1.2: FTIR spectra of bulk gCN and ball-milled gCN.

FTIR spectroscopy was next utilized to understand the surface functionalities of the gCN in its bulk state. The FTIR spectrum of gCN and ball-milled gCN is shown in **Figure 2.1.2**. The spectra showcase a broad peak in the region of 3100 - 3400 cm^{-1}, enumerating the presence of -NH and -OH groups on the surface of the gCN. The -NH group indicates the free amino groups at the unpolymerised triazine rings. Whereas the -OH group correspond to the oxygen-containing surface contaminants like carbonates and water molecules adsorbed on the gCN surface. Multiple peaks between 1100 and 1600 cm^{-1} correspond to the various vibrations of the C-N bonds constituting the polymeric

arrangement of triazine rings. The stretching vibrations of C-N (-C)-C or C-NH-C are associated with the bands at 1317 and 1239 cm^{-1}. The aromatic C-N vibrations of stretching has been attributed to the intense bands at 1640, 1569, and 1401 cm^{-1}, demonstrating the effective formation of gCN. At the same time, the sharp peak at 804 cm^{-1} belongs to the characteristic out-of-plane bending/breathing vibration mode of the triazine units in the gCN framework [37,41,42]. The FTIR spectra of the ball-milled gCN also exhibited similar peaks with higher absorbance reflecting the increased disorder and defects.

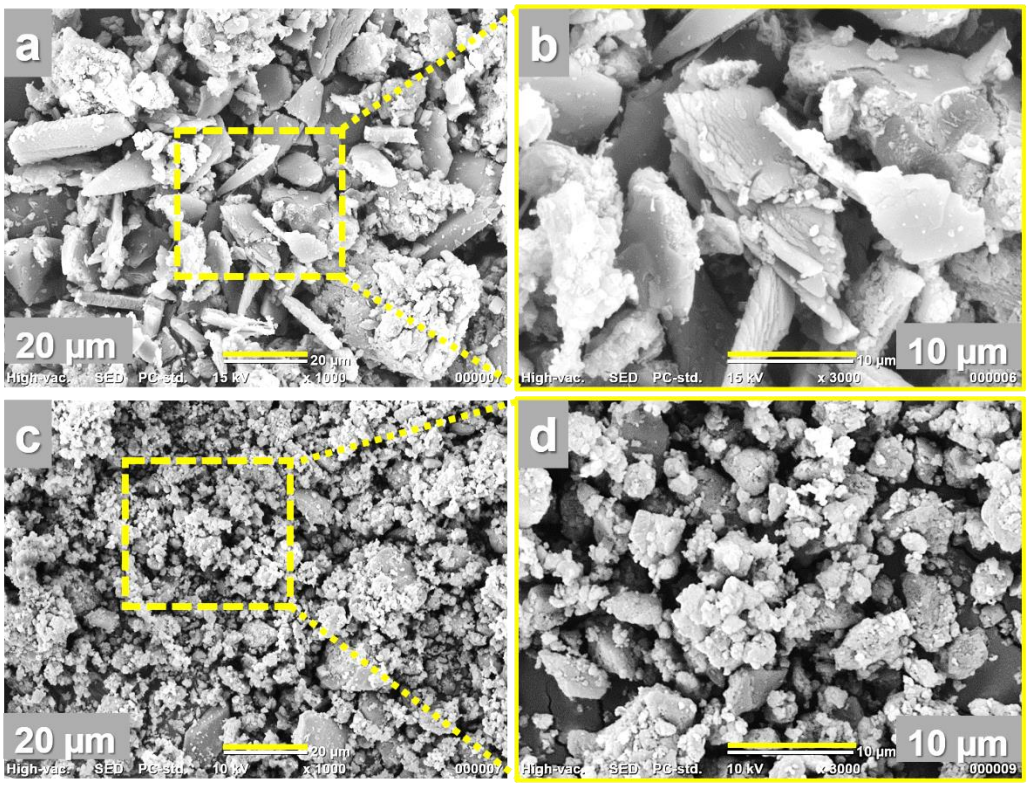

Figure 2.1.3: SEM images demonstrating surface morphology of (a,b) bulk gCN, and (c,d) ball-milled gCN.

Scanning electron microscopic (SEM) images of the bulk and ball-milled gCN were next recorded to visualize the structural changes. **Figure 2.1.3** represents the SEM images of gCN before (a, b) and after ball milling (c,d). It can be witnessed from the figure that the synthesized gCN exists in plate-like morphologies, which were pulverized to much smaller structures after ball-milling. The SEM images validate the conclusions drawn

from the XRD and Raman spectroscopy and confirm the smaller crystal structure of the ball-milled gCN with more edges and defects. The structural perturbation and increased surface area caused by ball milling are expected to be conducive to the electrochemical applications and therefore were investigated in detail.

2.1.3.2 gCN Electrodeposition and In-Situ Decoration with MnO_2 Nanostructure:

After the detailed material characterization, the possible benefits of bulk and ball-milled gCN for enhancing the electrochemical characteristics of a conducting scaffold were investigated. To date, several reports have documented the use of gCN modified surfaces and their application for developing electrochemical sensors. However, in all the previously reported publications, it has been simply drop-casted on the electrode surface. Nevertheless, drop-casting is associated with problems like non-uniform particle distribution, spreading issues complicated by human errors, and uncontrolled loading. The chemical instability of the immobilized material under experimental conditions is another issue that severely affects the reproducibility and reliability of the measurements. Therefore, in this work, a one-step electrochemical fabrication of MnO_2 decorated gCN has been attempted with the objective of developing a scaffold for sensitive and selective voltammetric detection of catecholamines. To the best of our knowledge, this is the first report describing the unconventional approach of controlled surface engineering of a substrate via the electrodeposition of MnO_2 decorated gCN and its sensing application. Therefore, the following sections will focus on understanding electrodeposition mechanisms and deciphering how experimental parameters affect electrochemical performance.

2.1.3.2.1 Mechanistic Understanding

The gCN electrodeposition/electropolymerization has been carried out using cyclic voltammetry in the gCN containing aliquots as per the details mentioned in the

experimental section. The first cyclic voltammograms showcase that the electropolymerization proceeded via the oxidation of free amino groups at ~ 0.6 V, followed by radical cation formation at ~1.3 V. The radical peak was observed only in the first cycle as it gets consumed while catalyzing further steps. Nevertheless, another peak at 0.75 V was observed after the first cycle, corresponding to triazine ring electropolymerization. With the increasing number of scans, the peak at 0.6 V corresponding to the oxidation of free amino groups of unpolymerized triazine rings decreases, and ultimately merges with the peak at 0.75 V, leading to a broad peak, shifting towards higher potentials (Inset of **Figure 2.1.4(a)**). The increased peak current and peak width at ~ 0.75 V indicate the successful electropolymerization of gCN using the unpolymerized triazine rings as monomers. With the increasing extent of polymerization, the free monomers should decrease, which supports the decreased contribution from the oxidation peak at 0.6 V. Thus, the successful surface functionalization with electropolymerized gCN was concluded from the CV curves[46]. XRD and HR-SEM also confirmed the effective surface functionalization via gCN and are discussed in the following sections.

Next, the mechanistic of in-situ formation and electrodeposition of MnO_2 nanostructures from the Mn^{2+} solution was deciphered through the peaks observed in the cyclic voltammograms (**Figure 2.1.4(b)**). Under the conditions used in the experiment, the electro-oxidation of Mn^{2+} to MnO_2 is reported to proceed via electrochemically induced chemical reactions (ECE mechanism; two electrochemical steps separated by a chemical step).

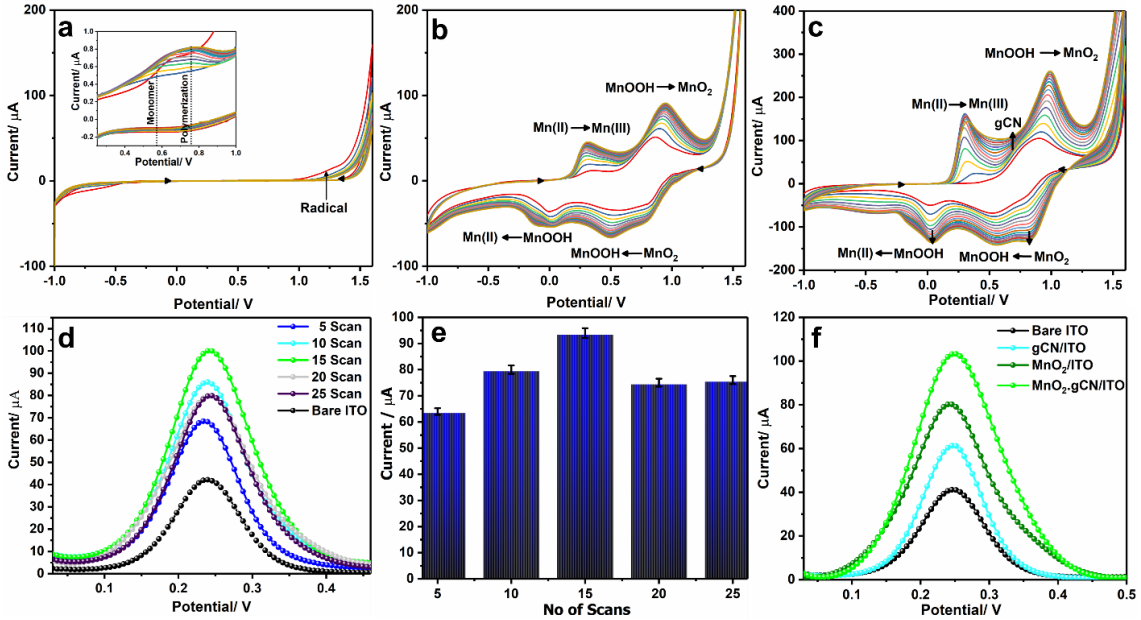

Figure 2.1.4: (a-c) Cyclic voltammograms observed for electrodeposition of (a) gCN (b) MnO_2 and (c) gCN.MnO_2 composite. (d) Square wave voltammograms (e) bar diagram of current response observed using gCN.MnO_2/ITO for 0.5 mM $K_3Fe(CN)_6$ in KCl as a function of different number of electrodeposition scans. (f) Comparative square wave voltammograms recorded for 0.5 mM $K_3Fe(CN)_6$ in KCl at Bare ITO (black), gCN/ITO (cyan), MnO_2/ITO (olive) and MnO_2.gCN/ITO (green).

Validating the previously reported data, the observed cyclic voltammogram manifested similar peaks corresponding to Mn(II) oxidation to Mn(III) at 0.3 V. The Mn(III) so formed being metastable chemically hydrolyses to MnOOH. On further application of potential, MnOOH oxidizes to MnO_2 on the ITO substrate exhibiting a peak centered at 0.9 V. In the reverse sweep, the reduction of MnO_2 to MnOOH and Mn^{2+} takes place corresponding to the peak at 0.9 V, 0.4 V, and 0 V, respectively[47–51]. The observed currents for the respective peaks increased with the increasing number of deposition cycles indicating the successful electrodeposition of conducting MnO_2 on the ITO surface. The mechanism is represented in the equation as follows:

ECE mechanism

$Mn^{2+} \longrightarrow Mn^{3+} + e^-$ (Electrochemical Oxidation at 0.3 V)

$Mn^{3+} + 2H_2O \longrightarrow MnOOH + 3H^+$ (Hydrolysis in a chemical process)

$MnOOH \longrightarrow MnO_2 + H^+ + e^-$ (Electrochemical Oxidation at 0.9 V)

Finally, the one-step electrodeposition of MnO_2 decorated gCN on the ITO surface was attempted. To do so, cyclic voltammetry was carried out in a solution containing both the gCN, and Mn^{2+} and the resulting voltammograms are presented in **Figure 2.1.4(c)**. As visible from the figure, the current responses were substantially higher than the individual responses of gCN and MnO_2, respectively. Furthermore, with the co-existence of gCN and MnO_2, the electropolymerization peak of gCN was found to merge with the oxidation peak of MnOOH, resulting in a broad peak centered at ~ 0.7 V. It is worth mentioning that in the presence of gCN, the peak of MnOOH was slightly shifted to higher potentials which could be because of the stabilization of Mn^{3+} (or MnOOH) species by gCN. Ascribed to this stabilization, it is expected that the Mn^{3+} (or MnOOH) specie can stably exist for a longer period of time, and thus a little more work needs to be done for its further oxidation to Mn^{+4} (MnO_2). The increased stability of Mn^{3+} (or MnOOH) was also inferred from the reverse cycle showcasing increased contribution from the MnO_2 to MnOOH and MnOOH to Mn(II) peaks compared to the side peaks observed in the absence of gCN. We propose that the increased current is because of the synergistic interactions between the Mn^{3+} (or MnOOH) and the lone pair of nitrogen and surface oxygen groups of gCN, which provided additional stability to the otherwise unstable Mn^{3+}/MnOOH ions. The peak current corresponding to all the peaks increased with every scan indicating the formation of MnO_2 decorated gCN with substantially improved electrochemical characteristics.

2.1.3.2.2 Protocol Optimization

The extent of surface functionalization via electrodeposition is a function of the number of CV scans, which in turn dictates the electrochemical response. Therefore, the electrochemical response of the gCN and MnO_2.gCN/ITO was monitored by varying the number of CV cycles. For comparative evaluation, the CV and SWV peak current of 0.5

mM $K_3[Fe(CN)_6]$ was recorded using the gCN/ITO and MnO_2.gCN/ITO prepared by employing a different number of CV scans in the range of 5-25. **Figure 2.1.4(d & e)** demonstrates that the peak current increased with increasing deposition cycles till 15 scans. After the 15^{th} scan, a slight decrease in the peak current was observed because the thicker surface layer created a mechanical barrier between the electrode surface and the analyte, leading to capacitive current and impeded electron transfer. Therefore, 15 scans were finalized for the optimized surface modification protocol and used for all the further measurements.

Furthermore, the electrochemical response of bare ITO, gCN/ITO, MnO_2/ITO, gCN.MnO_2/ITO were compared. As visible from the **Figure 2.1.4(f)**, gCN.MnO_2 exhibited the highest peak current compared to all the other surface modified scaffolds prepared following the optimized protocol. An increment of ~ 2.75 fold was witnessed compared to the bare ITO. These findings demonstrate that there are more electrochemically active spots on the gCN.MnO_2/ITO facade that facilitates the electron transfer and results in the substantial improvement in current. Henceforth, gCN.MnO_2/ITO scaffold has been extensively characterised and investigated for electrochemical applications.

2.1.3.2.3 Surface Characterization

Motivated by the electrochemical affirmations, the step-by-step changes in the surface topography were further visualized using HR-SEM. The microscopic images of the bare ITO, gCN/ITO, MnO_2/ITO, gCN.MnO_2/ITO and EDX of gCN.MnO_2/ITO are presented in **Figure 2.1.5 (a-i)**. As the figure shows, the smooth plate-like growth was observed on the gCN/ITO surface. On the other hand, MnO_2/ITO showcased microscopically open 3D worm-like structures of dimensions in the range of 10-20 nm (width). Interestingly, gCN.MnO_2 exhibited gCN plate-like structures decorated with nanoworms of MnO_2. The

visible surface decoration of gCN with MnO_2 nanostructures was further supported by the elemental mapping, univocally demonstrating the uniform surface distribution of Mn and O over carbon and nitrogen.

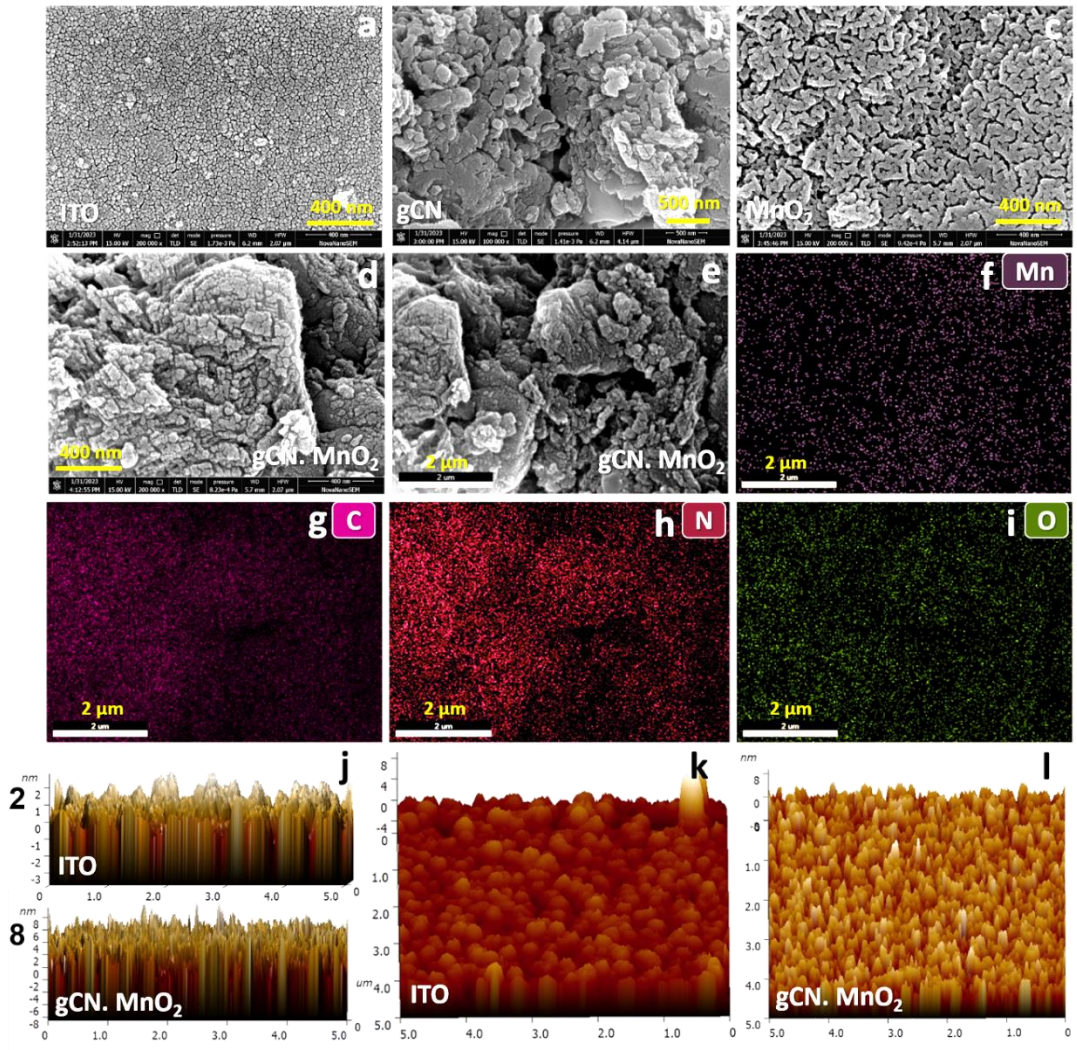

Figure 2.1.5: HR-SEM images of (a) Bare ITO, (b) gCN/ITO, (c) MnO_2/ITO, (d) gCN.MnO_2/ITO. (e-h) represents the gCN.MnO_2/ITO region used for elemental mapping of Mn, C, N and O, respectively. (j) Comparative AFM surface profile at 5 µm resolution for ITO and gCN.MnO_2/ITO. 3D AFM surface profile of (k) ITO, and (l) gCN.MnO_2/ITO.

The atomic force micrographs (AFM) shown in **Figure 2.1.5 (j-l)** demonstrate the pronounced coarse and prickly surface profile of the gCN.MnO_2/ITO compared to bare ITO. From the AFM analyses of the peak profile, an average height of 9.551 nm was observed for gCN.MnO_2/ITO compared to 1.472 nm exhibited by ITO. The increased peak height accounts for 7-8 nm thick electrodeposited gCN.MnO_2 layer on the ITO

scaffold. The consequential increase in the nanoscale roughness was also witnessed after electrodeposition. As a result of electrodeposition, the average roughness increased from 0.858 nm to 1.897 nm.

After visual confirmation, the surface/chemical functionalities corresponding to MnO_2 and gCN were further investigated using X-ray diffraction (XRD). **Figure 2.1.6(a-b)** illustrates the X-ray diffraction (XRD) peaks observed for four different samples: indium tin oxide (ITO), gCN-coated ITO (gCN/ITO), MnO_2-coated ITO (MnO_2/ITO), and gCN.MnO_2-coated ITO (gCN.MnO_2/ITO). The ITO displays distinct X-ray diffraction (XRD) peaks at 21.6°,30.0°,35.0°,50.4° and 59.9° corresponding to (211), (222), (400), (440), and (622) planes, respectively[52]. These peaks are marked with an asterisk (*) for identification purposes. An additional peak at 28.1°, denoted by the symbol #, corresponding to the (002) plane of the gCN confirms the electrodeposition of gCN on the ITO substrate[53]. Electrodeposition of MnO_2 on the ITO surface results in three additional XRD peaks at 28.1°,40.2° and 58.2° represented by Ψ, corresponding to the planes of MnO_2 (310), (002), and (312), respectively[38]. Interestingly, gCN.MnO_2/ITO exhibited characteristic XRD peaks of both gCN and MnO_2 consistently at the same 2Θ values. X-ray powder diffraction (XRD) analysis supports the conclusion that the gCN/MnO_2 layer on the ITO surface has been electro functionalized. XPS was ultimately employed to confirm the structural characteristics of the electrodeposited gCN.MnO_2 composite **(Figure 2.1.6(c-j))**. **Figure 2.1.6(c and d)** depicts the full survey XPS spectra corresponding to bare ITO and gCN.MnO_2/ITO. The In and Sn peak intensity in coated ITO was significantly lower than uncoated ITO, confirming the presence of an additional top layer on the scaffold. Furthermore, the gCN.MnO_2/ITO had an additional peak corresponding to Mn, suggesting the manganese containing top layer. Detailed analysis was done using the high-resolution deconvoluted XPS spectra.

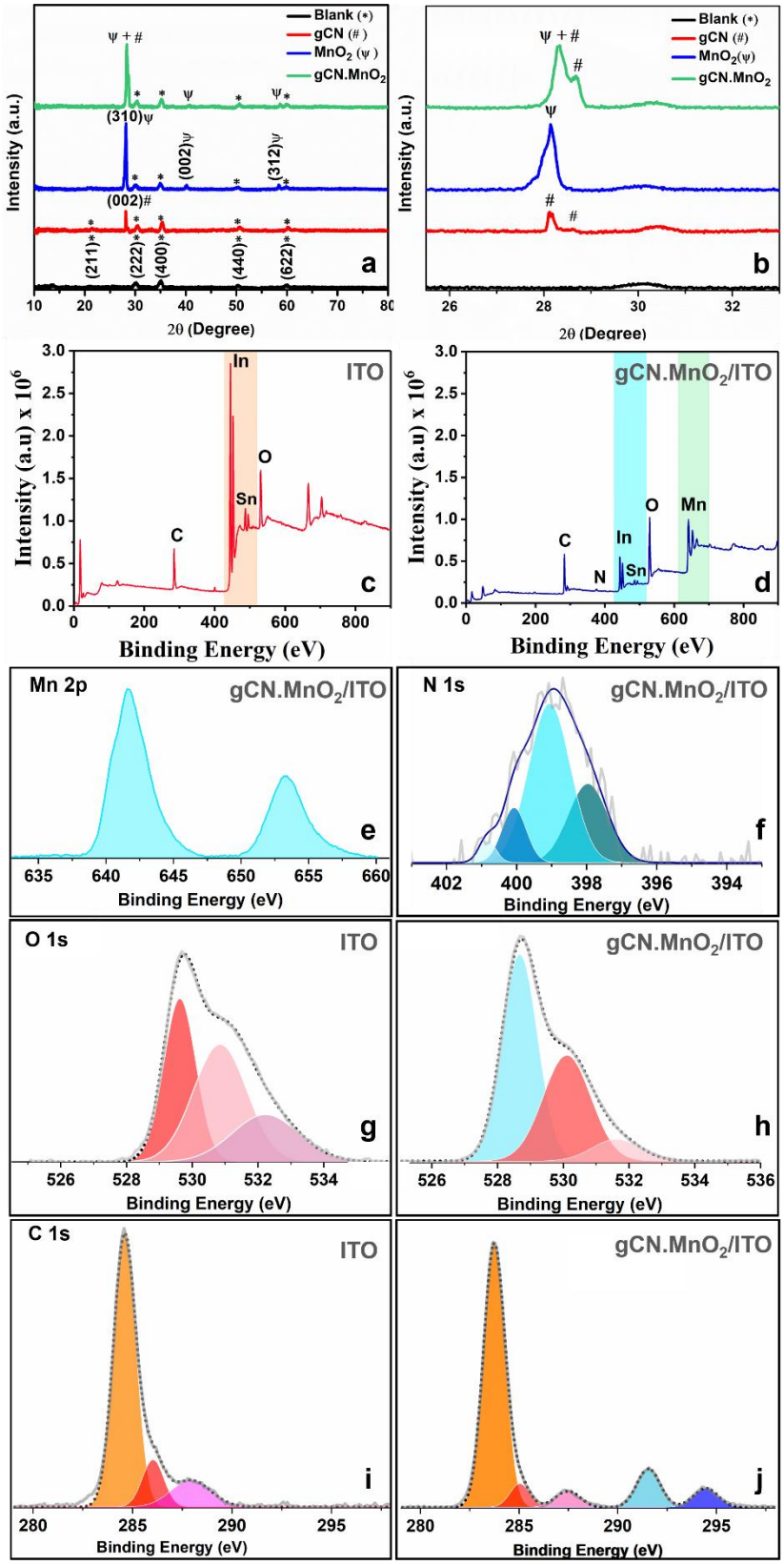

Figure 2.1.6: (a,b) X-ray diffractogram of coated and uncoated ITO. X-ray photoelectron spectra of (c) ITO (full survey), (d) gCN.MnO_2/ITO (full survey). (e) Mn 2p for gCN.MnO_2/ITO, (f) deconvoluted N1s spectra for gCN.MnO_2/ITO. Deconvoluted O1s spectra for (g) ITO, (h) gCN.MnO_2/ITO. Deconvoluted C1s spectra for (i) ITO, and (j) gCN.MnO_2/ITO. The light grey line in the XPS plots represents the raw data whereas the black dotted line represents the fitted data.

The Mn 2p spectra showcase two significant signals at 641.7 eV and 653.3 eV corresponding to Mn 2p3/2 and Mn 2p1/2 **(Figure 2.1.6(e))**. The difference of 11.6 eV in the spin energy between Mn 2p3/2 and Mn 2p1/2 was attributed to the presence of Mn^{4+}, confirming the electrodeposition of MnO_2 containing surface layer. The peak at 528.6 eV in coated ITO for O1s XPS spectra further indicates the Mn-O bond of MnO_2 **(Figure 2.1.6(g-h))** [54–58]. The other two peaks at 529.6 and 530.8 eV were also observed for the bare ITO and can be assigned to In-O and Sn-O. Furthermore, the N 1s spectrum displayed four signals originating from the different nitrogen environments in the triazine structural unit of gCN at the binding energies of 398.7 eV, 399.6 eV, 400.2 eV, and 400.7 eV, respectively **(Figure 2.1.6(f))**.

The peak at 398.7 eV is attributed to N atoms, sp^2-bonded to two carbon atoms (C=N-C). The peak at 399.6 eV corresponds to N atoms trigonally bonded to three sp^2 carbon atoms in the C–N network ($N-(C)_3$). The peak at 400.2 can be assigned to N-H groups of open ends in the graphitic carbon nitride network [22,59–61]. The presence of gCN was indicated by the additional two peaks in the C1s spectra corresponding to graphitic sp^2 (C=C) and s-triazine unit (N-C=N) at 291.5 eV and 294.4 eV, respectively **(Figure 2.1.6(i-j))**. The XPS data supports the conclusions drawn from XRD and HR-SEM and manifests the electrodeposition of gCN and MnO_2 containing surface layer on the ITO scaffold.

Next the changes in the surface was characterised electrochemically. The electroactive surface area of the bare ITO and MnO_2.gCN/ITO was experimentally determined. To do so, the cyclic voltammograms of the bare and MnO_2.gCN/ITO were recorded in an equimolar mixture of 1 mM $K_3[Fe(CN)_6]$ solution and 1 M KCl at various scan rates between 10 to 100 mVs^{-1}. Both the voltammograms (**Figure 2.1.7**) showcase a reversible redox couple corresponding to the diffusion-controlled oxidation and reduction of the

Fe^{2+}/Fe^{3+} couple. With the increase in scan rate, no observable potential shift was noticed, manifesting the involvement of a diffusion-controlled reversible redox process. The electrochemically active area of the unmodified and modified electrode was calculated using the Randles-Sevcik equation[62]:

$$I_p = 2.69 \times 10^5 \, n^{3/2} \, A D^{1/2} C \, \upsilon^{1/2}$$

Where I_p is the peak current (μA), n is the number of electrons transferred, A is the electro-active area (cm^2), D is the diffusion coefficient of $[Fe(CN)_6]^{3-}$ in KCl solution ($cm^2 \, s^{-1}$), C is the probe molecule concentration (μM), and υ is the scan rate ($V \, s^{-1}$).

From the slope of I_p vs. $\upsilon^{1/2}$ linear plots, the active area of the bare electrode was calculated to be 0.180 cm^2, whereas the area of the modified electrode was determined to be 0.246 cm^2. In agreement with the AFM analysis, this relative measurement suggests the electrodeposition of gCN.MnO_2 results in an increment of ~ 36% in the electroactive surface area, which very well explains the improvement in the electrochemical responses.

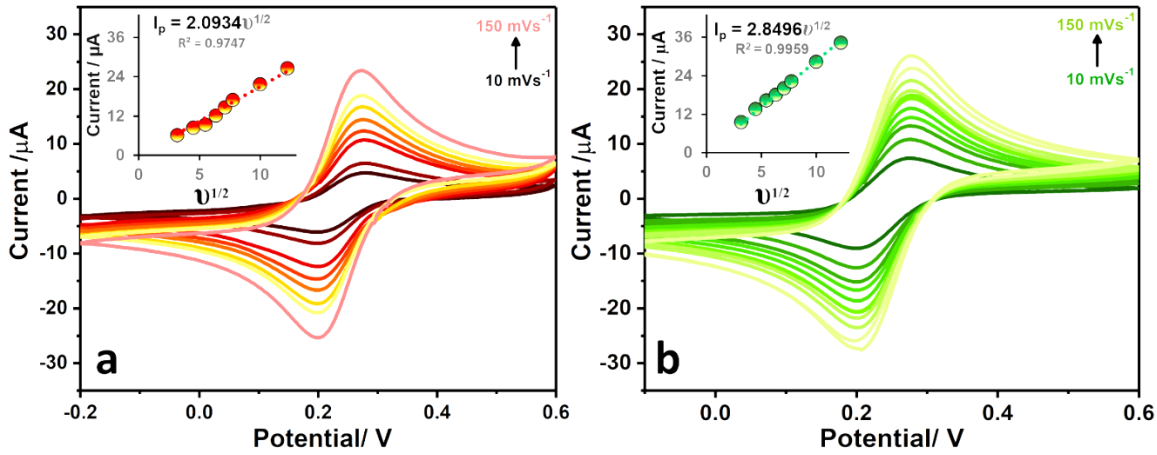

Figure 2.1.7: Cyclic voltammograms observed for 0.5 mM solution of $K_3[Fe(CN_6)]$ with varying scan rate from 10-150mV/s^{-1} recorded using (a) ITO and (b) gCN.MnO_2/ITO. Insets represents the corresponding I_p vs. $\upsilon^{1/2}$ linear plots.

2.1.3.3 Voltammetric Sensing of Dopamine as the Test Case

From the in-depth comparative surface and electrochemical characterizations, it's clear that the active interaction of Mn^{x+} with the nitrogen lone pair present in gCN facilitates the electron transfer process and credits substantially improved electrochemical activity

to the gCN.MnO_2/ITO. This gCN.MnO_2 modified scaffold is well suited for sensitive and selective electrochemical sensor applications. The suitability can be explained on the basis of enhanced surface area, functional groups, and availability of π- electrons required for the favorable interaction with electroactive analytes like biomarkers, catechols, creatinine, hydrocortisone, toxic organic dyes, and many more. Therefore, here in this section, the pragmatic applicability of the uniquely engineered gCN.MnO_2/ITO has been tested for the voltammetric sensing of dopamine (DA), a primary catecholamine neurotransmitter.

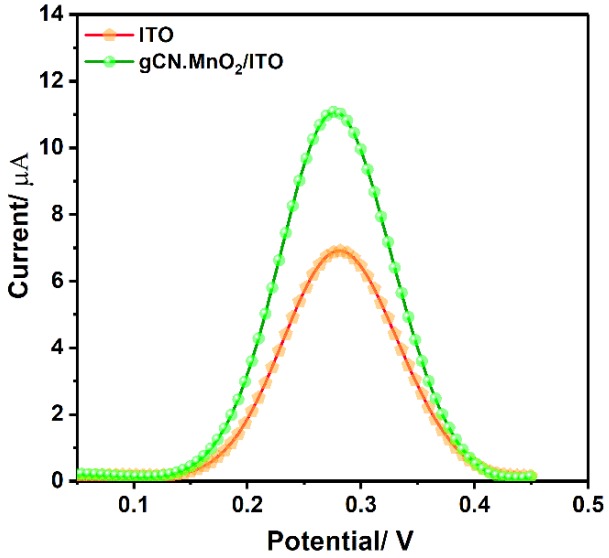

Figure 2.1.8: A comparative Square Wave Voltammograms of 150 µM of DA observed in PB 7.4 buffer at bare ITO (Saffron) and gCN.MnO_2 coated ITO (Green).

Square wave voltammetry was used to assess the electrochemical characteristic of dopamine. **Figure 2.1.8** illustrates the electro-oxidation of 150 µM DA exhibiting a peak at 0.28 V on both the bare and gCN.MnO_2/ITO. However, a significant difference in the peak current was observed. The gCN.MnO_2/ITO resulted in a peak current of ~13 µA compared to 7 µA recorded for the bare ITO. The ~2-fold increase in the peak current for the same concentration of DA hinted toward possibly high sensitivity of the gCN.MnO_2/ITO. It was accounted on the basis of the synergistic contribution from the

π-π interactions between the aromatic structures of the gCN and DA molecules, enhanced surface area, and facilitated electron transfer at the gCN.MnO_2 composite.

The peak current corresponding to 0.27 V was found to increase linearly with the increasing DA concentration in the range of 5 µM - 500 µM as shown in **Figure 2.1.9** By plotting I_p vs. concentration, the following regression equations were found to represent the effect of DA concentration on the peak current.

These expressions are the basis of the quantitative estimation of DA.

$\boldsymbol{I_p}$ (μA) = 0.0681**C** [0-300 µM]; R^2 = 0.9984……..**:** gCN.MnO_2/ITO

$\boldsymbol{I_p}$ (μA) = 0.0562**C** [0-300 µM]; R^2 = 0.9983……..**:** ITO

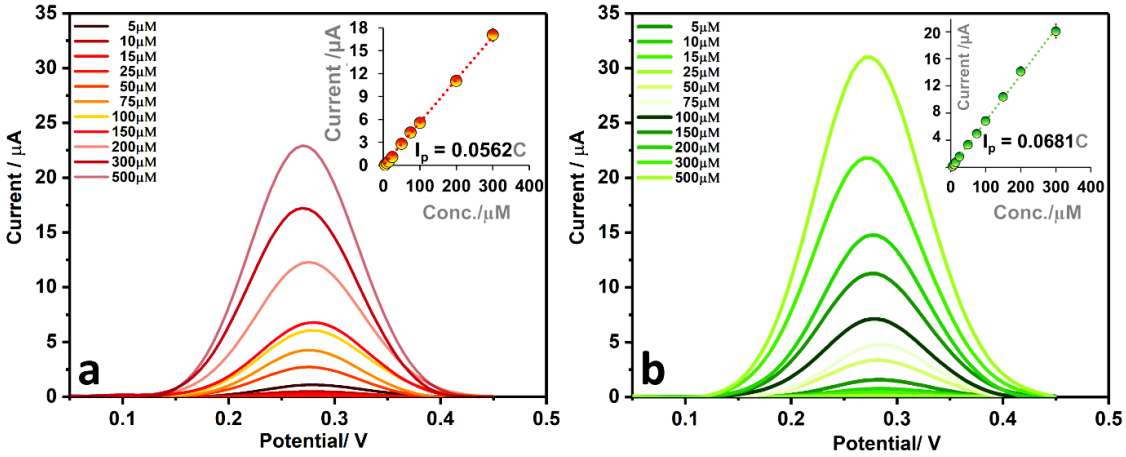

Figure 2.1.9: Concentration-dependent study: Square wave voltammogram recorded for 5 µM, 10 µM, 15 µM, 25 µM, 50 µM, 75 µM, 100 µM, 150 µM, 200 µM, 300 µM, 500 µM DA concentration using (a) bare ITO and (b) gCN.MnO_2/ITO. Insets include the corresponding calibration plots for DA concentration from 5 µM to 300 µM.

The slope of the linear regression equation indicates the sensitivity of the developed sensor. As can be seen, gCN.MnO_2 demonstrated ~22 % more sensitivity compared to bare. Furthermore, LOD was calculated using 3σ/b where 'σ' corresponds to the standard deviation of five blank readings and 'b' denotes the slope of the regression equation. It was observed that a LOD of 20 nM was obtained for gCN.MnO_2 compared to 110 nM for bare ITO. The improved sensitivity manifests the gCN.MnO_2/ITO is an efficient scaffold for voltammetric sensing applications. Interestingly, the proposed gCN.MnO_2

scaffold exhibits superior performance compared to previously reported DA electrochemical sensors developed using gCN and related surface modifiers **(Table 2.1.1)**. Additionally, all the reported methodologies include individual synthesis of constituting materials followed by mixing and drop-casting the prepared material. In contrast, the proposed protocol reports in-situ synthesis in a single step, making it more practical and scalable.

Table 2.1.1: Comparison of the proposed gCN.MnO_2/ITO scaffold with the reported DA electrochemical sensors developed using gCN, metal oxides and related surface modifiers

Electrode Material	***Technique***	***Linear range (µM)***	***LOD (µM)***	***Modification method***	***Ref.***
g-C_3N_4/Co/GCE	DPV	2-400	0.4	Multistep Synthesis + Drop cast	[63]
CSO-gCN/GCE	DPV	100-400	29	Multistep Synthesis + Drop cast	[64]
CNNS-GO/GCE	DPV	1-20	0.096	Multistep Synthesis + Drop cast	[65]
C_3N_4-GO/GCE	DPV	0.25-320	0.07	Multistep Synthesis + Drop cast	[66]
MnO_2NFs/NG/GCE	SDLSV	0.1-10 10-100	0.039	Multistep Synthesis + Drop cast	[67]
Mn_3O_4-graphite electrode	DPV	10-70	0.1	Multistep Synthesis + Drop cast	[68]
Pt/rGO/MnO_2NFs/GCE	DPV	1.5-215.56	0.1	Multistep Synthesis + Drop cast	[69]
gCN.MnO_2/ITO	SWV	5-500	0.02	Single step *in*-situ electrodeposition	This work

Though increased surface area and surface functionalities are beneficial for electron transfer, nevertheless, it can also promote surface adsorption leading to undesirable capacitive current and surface fouling. Therefore, the impact of surface modification on

the nature of the mass-transfer process involved in the oxidation of DA was investigated by carrying out the frequency study. The square wave voltammograms were recorded for 150 µM DA in pH-7.4 buffer with varying frequencies from 5 to 50 Hz. The observed variation of peak current in response to the frequency was found to be related by the following regression equations (**Figure 2.1.10**):

I_p (μA) = 0.1010f [2-50 Hz] + 4.695 R^2 = 0.9656 ……...**:** ITO

I_p (μA) = 0.8807$f^{½}$ [2-50 Hz] + 3.102 R^2 = 0.9828……..**:** ITO

I_p (μA) = 0.1092f [2-50 Hz] + 8.119 R^2 = 0.8817……**:** gCN.MnO_2/ITO

I_p (μA) = 0.9873$f^{½}$ [2-50 Hz] + 6.239 R^2 = 0.9763……..**:** gCN.MnO_2/ITO

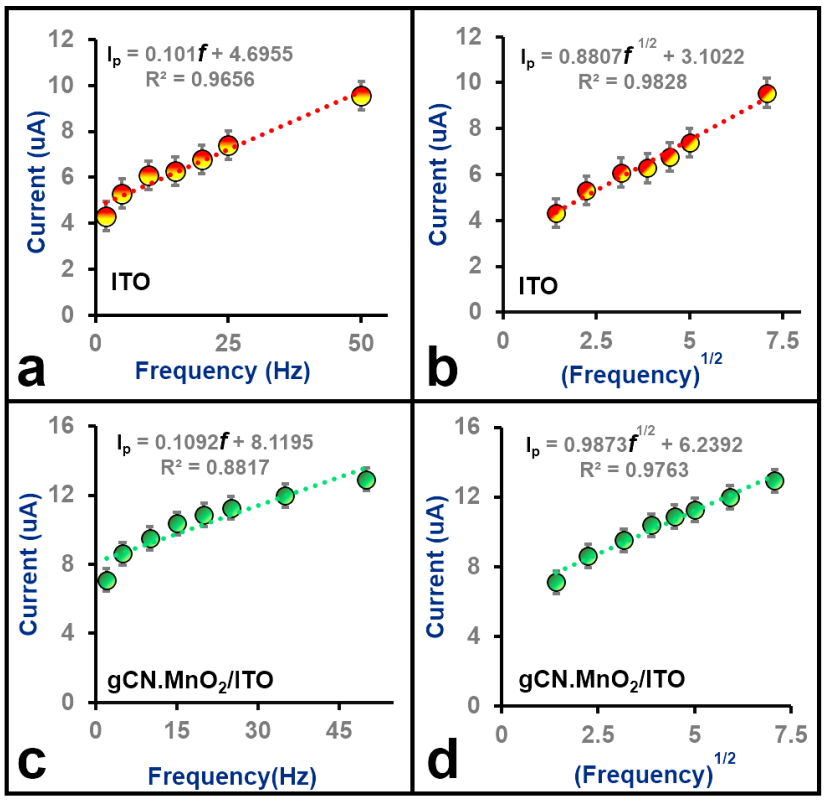

Figure 2.1.10: The linear relation between I_p Vs (f) and I_p Vs (f) ^{½} recorded in 150 µM DA in pH-7.4 buffer with increasing frequencies from 5-50 Hz using bare ITO (a,b) and gCN.MnO_2/ITO (c,d).

Both the modified and unmodified scaffolds demonstrate a more linear variation of I_p vs. $(f)^{1/2}$ compared to I_p vs. f. Obeying the Randles Sevcik equation, the linearity of I_p vs. $(f)^{1/2}$ indicates the involvement of diffusion-controlled mass transfer without any added

adsorption complications[70]. Therefore, this study rules out any unfavourable consequence associated with the enhanced electroactive area and added surface functionalities of the gCN.MnO_2/ITO.

After evaluating the sensitivity, the selectivity of the developed scaffold was next investigated. It is known that uric acid (UA), dextrose, and melatonin are frequently found in body fluids, making it challenging to estimate DA in the real complex matrix. Higher levels of these metabolites can interfere with the desired electrochemical process, altering the position of the oxidation peak potential, and peak current and impairing sensor selectivity. Therefore, interference studies have been conducted to ensure the selectivity of the proposed approach. To do so, the peak current corresponding to the oxidation of 150 µM DA at ~0.27 V was measured in presence and absence of three potential interfering molecules, dextrose, UA, and melatonin. The observed peak current corresponding to DA, DA + 5-fold Mel, DA+ 5-fold UA, and DA+ 5-fold dextrose has been represented in the bar diagram. From **Figure 2.1.11(a)**, it can be clearly seen that no substantial deviation was observed in the current response of DA in the presence of 5-fold higher concentration of other metabolites. However, when the concentration of interferant was increased to 10-folds, a maximum deviation of 3.5 % was observed in the presence of UA. Thus, based on the above measurements, it can be firmly concluded that the gCN.MnO_2/ITO can be efficiently used for the sensitive and selective quantification of DA even in a complex matrix.

Therefore, the developed sensor was confidently employed to assay the DA content in the commercially available injection (Domin, Neon Laboratories Limited, India) **(Figure 2.1.11(c))**. The observed and expected DA concentration values are listed in **Table 2.1.2** and found to be in close agreement showcasing a maximum deviation of 3.4 %.

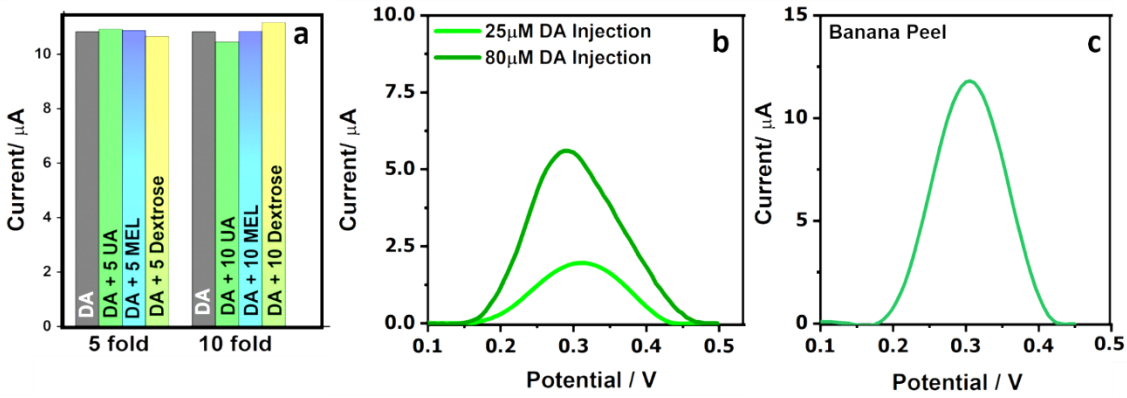

Figure 2.1.11: (a) Bar diagram representing the peak currents observed from square wave voltammograms recorded for fixed concentration of DA (150μM) in presence of 5-fold and 10-fold higher concentration of Uric acid, Melatonin and Dextrose using gCN.MnO_2/ITO. Observed square wave voltammograms representing presence of DA in (b) pharmaceutical sample and (c) banana peel.

Table 2.1.2: Determination of DA content in commercially available IV injection.

Sample	*Used Conc.*	*Observed Conc.*	*Error %*
Domin, Neon Laboratories Ltd	25 μM	25.9 μM	3.6
Domin, Neon Laboratories Ltd	80 μM	82.4 μM	3.0

The suitability of the developed sensor for determining DA content in the Banana Peel was also assessed. To prepare the test sample, the banana peel was crushed into a thin paste and then diluted with 2 mL of pH-7 buffer. After filtration, the supernatant was used right away for electrochemical analysis. The presence of DA was confirmed by an oxidation peak of DA at ~ 2.9 V as shown in **Figure 2.1.11(c)**. Using the calibration plot, the concentration of DA was found to be 175 μM which was validated by a parallel quantitative estimation using UV- spectrometer showing it to be 173.27 μM.

2.1.3.4 Stability and Reproducibility Studies

The stability of the MnO_2.gCN scaffold was evaluated by examining the changes in its electrochemical behavior upon excessive cycling in the pH-7.4 buffer. **Figure 2.1.12(a)** indicates the considerable resilience of the MnO_2.gCN scaffolds over 200 cycles. The absence of a substantial change in the blank voltammograms confirms the stability of the engineered surface for repeated applications. By taking periodic square wave voltammograms in $K_3[Fe(CN)_6]$ solution, the time-dependent stability and repeatability

of the sensing surface have also been studied **(Figure 2.1.12(b))**. The sensor surface exhibits a negligible current reduction when exposed to air in a laboratory for one month. The data indicate that the engineered scaffold is exceptionally stable for an extended period of time and does not necessitate additional storage measures. However, storing the electrodes in a dry environment or a box packed with nitrogen will extend their lifespan.

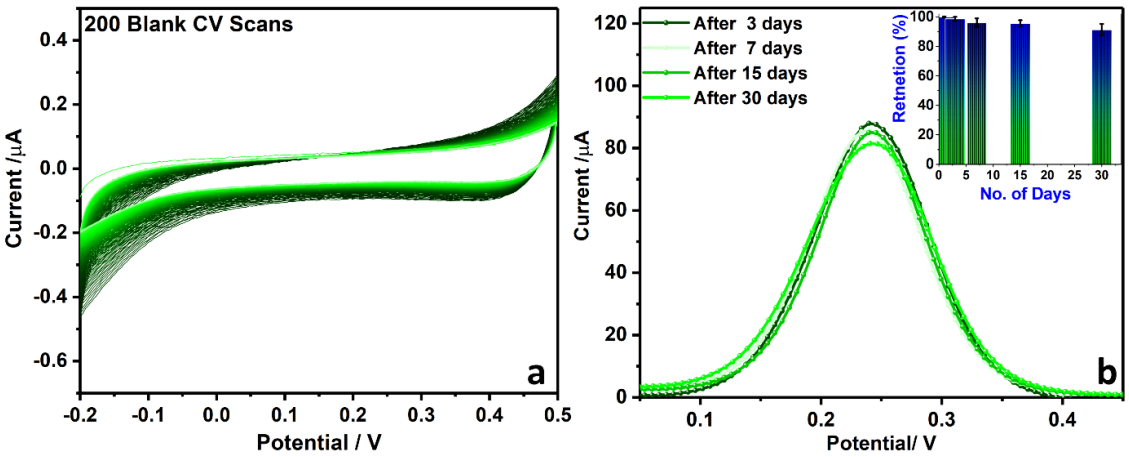

Figure 2.1.12: (a) Continuous 200 cycle voltammograms recorded in PB-7 using gCN.MnO_2/ITO (b) SWV recorded in 0.5 mM solution of $K_3[Fe(CN_6)]$ using gCN.MnO_2/ITO scaffolds at different time intervals.

2.1.4. Conclusions

Voltammetric sensors rely primarily on interfacial electrochemistry. A rationally tailored interface can manoeuvre selectivity and sensitivity to the voltammetric sensor. Therefore, surface-modified conducting scaffolds are one of the crucial components of any electrochemical sensor. Henceforth, the presented investigation proposed a robust and eccentric approach to tailor MnO_2 nanostructure decorated gCN modified scaffold for the voltammetric applications. The proposed scaffold is prepared via facile one-step electrodeposition with precise control over film thickness in contrast to the conventional drop-casting methodology. The successful deposition and resulting topography and surface changes have been concluded through detailed microscopic and spectroscopic tools. It was concluded that electrodeposition is an effective strategy for fabricating gCN functionalised surfaces. The fabricated gCN.MnO_2/ITO exhibits intimate interfacial

contacts, promoting charge transfer and mass transport as inferred from the comparative electrochemical responses. Consequently, the gCN.MnO_2/ITO electrode demonstrates a remarkable capability to analyze dopamine as the test case through its electrochemical oxidation at ~0.27 V using square wave voltammetry. A 22 % enhancement in the sensitivity and a detection limit of 20 nM was observed for gCN.MnO_2 deposited ITO. In addition to high sensitivity, the gCN.MnO_2 showcases appreciable selectivity, repeatability, and stability. Impressively, the obtained electrode endows a remarkable performance in assaying dopamine in pharmaceutical and food samples with an error of < 3%. From the in-depth surface, chemical, and electrochemical characterization, it has been manifested that the introduced, unconventional surface functionalization protocol holds the potential to revolutionize the use of gCN for electrochemical systems and the fabrication of localized heterojunctions. We believe this comprehensive study can further enrich the characteristics and applications of selective and sensitive surface-modified voltammetric sensors. However, to harness the wide-spread ability of the proposed strategy, it should further be studied using commercial electrodes like screen-printed electrodes, microelectrodes.

2.1.5. References

[1] P. Suja, J. John, T.P.D. Rajan, G.M. Anilkumar, T. Yamaguchi, S.C. Pillai, U.S. Hareesh, Graphitic carbon nitride (g-C3N4) based heterogeneous single atom catalysts: synthesis, characterisation and catalytic applications, J. Mater. Chem. A. 11 (2023) 8599–8646. https://doi.org/10.1039/D2TA09776A.

[2] P. Niu, J. Dai, X. Zhi, Z. Xia, S. Wang, L. Li, Photocatalytic overall water splitting by graphitic carbon nitride, InfoMat. 3 (2021) 931–961. https://doi.org/10.1002/inf2.12219.

[3] R. Sharma, M. Almáši, S.P. Nehra, V.S. Rao, P. Panchal, D.R. Paul, I.P. Jain, A.

Sharma, Photocatalytic hydrogen production using graphitic carbon nitride (GCN): A precise review, Renew. Sustain. Energy Rev. 168 (2022). https://doi.org/10.1016/j.rser.2022.112776.

[4] O. Iqbal, H. Ali, N. Li, M.Z. Ansari, A.I. Al-Sulami, K.F. Alshammari, H.S.M. Abd-Rabboh, Y. Al-Hadeethi, T.A. Taha, A. Zada, Z. Wang, A. Hayat, A Review on the Synthesis, Properties, and Characterizations of Graphitic Carbon Nitride (g-C3N4) for Energy Conversion and Storage Applications, Mater. Today Phys. (2023) 101080. https://doi.org/10.1016/J.MTPHYS.2023.101080.

[5] P. Gao, J. wen Li, J. Zhang, G. Wang, Computational exploration of magnesium-decorated carbon nitride (g-C3N4) monolayer as advanced energy storage materials, Int. J. Hydrogen Energy. 46 (2021) 21739–21747. https://doi.org/10.1016/J.IJHYDENE.2021.04.049.

[6] B. Das, L.P. Rao Pala, M.K. Mohanta, M. Devi, D. Chakraborty, N.R. Peela, M. Qureshi, S.S. Dhar, Organic–inorganic hybrid photocatalyst consisting of a highly conjugated metal complex and graphitic carbon nitride for efficient hydrogen evolution and Cr(VI) reduction, J. Mater. Chem. A. 10 (2022) 23691–23703. https://doi.org/10.1039/D2TA05200H.

[7] M.H. Chan, R.S. Liu, M. Hsiao, Graphitic carbon nitride-based nanocomposites and their biological applications: A review, Nanoscale. 11 (2019) 14993–15003. https://doi.org/10.1039/c9nr04568f.

[8] M.L. Yola, N. Atar, Development of molecular imprinted sensor including graphitic carbon nitride/N-doped carbon dots composite for novel recognition of epinephrine, Compos. Part B Eng. 175 (2019) 107113. https://doi.org/10.1016/j.compositesb.2019.107113.

[9] R. Motaghed Mazhabi, L. Ge, H. Jiang, X. Wang, A facile photoelectrochemical

sensor for high sensitive ROS and AA detection based on graphitic carbon nitride nanosheets, Biosens. Bioelectron. 107 (2018) 54–61. https://doi.org/10.1016/J.BIOS.2018.02.008.

[10] G. Kesavan, S.M. Chen, Highly sensitive electrochemical sensor based on carbon-rich graphitic carbon nitride as an electrocatalyst for the detection of diphenylamine, Microchem. J. 159 (2020) 105587. https://doi.org/10.1016/j.microc.2020.105587.

[11] J. Lv, C. Li, S. Feng, S.M. Chen, Y. Ding, C. Chen, Q. Hao, T.H. Yang, W. Lei, A novel electrochemical sensor for uric acid detection based on PCN/MWCNT, Ionics (Kiel). 25 (2019) 4437–4445. https://doi.org/10.1007/S11581-019-03010-8.

[12] F. Yang, S. Wang, Z. Li, Y. Xu, W. Yang, C. Yv, D. Yang, Y. Xie, W. Zhou, Polydopamine/defective ultrathin mesoporous graphitic carbon nitride nanosheets as Z-scheme organic assembly for robust photothermal-photocatalytic performance, J. Colloid Interface Sci. 613 (2022) 775–785. https://doi.org/10.1016/j.jcis.2022.01.012.

[13] J. Plaza, A. Arencibia, M.J. López-Muñoz, Optimization of thermal exfoliation of graphitic carbon nitride for methylparaben photocatalytic degradation under simulated solar radiation, J. Mater. Chem. A. 11 (2023) 9922–9930. https://doi.org/10.1039/D3TA01109G.

[14] K. Atacan, M. Özacar, Construction of a non-enzymatic electrochemical sensor based on CuO/g-C3N4 composite for selective detection of hydrogen peroxide, Mater. Chem. Phys. 266 (2021). https://doi.org/10.1016/J.MATCHEMPHYS.2021.124527.

[15] N. Gupta, K. Todi, T. Narayan, B.D. Malhotra, Graphitic carbon nitride-based

nanoplatforms for biosensors: design strategies and applications, Mater. Today Chem. 24 (2022) 100770. https://doi.org/10.1016/J.MTCHEM.2021.100770.

[16] R. Umapathi, C. Venkateswara Raju, S. Majid Ghoreishian, G. Mohana Rani, K. Kumar, M.H. Oh, J. Pil Park, Y. Suk Huh, Recent advances in the use of graphitic carbon nitride-based composites for the electrochemical detection of hazardous contaminants, Coord. Chem. Rev. 470 (2022) 214708. https://doi.org/10.1016/j.ccr.2022.214708.

[17] L. Qu, G. Zhu, J. Ji, T.P. Yadav, Y. Chen, G. Yang, H. Xu, H. Li, Recyclable Visible Light-Driven O-g-C 3 N 4 /Graphene Oxide/N-Carbon Nanotube Membrane for Efficient Removal of Organic Pollutants, ACS Appl. Mater. Interfaces. 10 (2018) 42427–42435. https://doi.org/10.1021/acsami.8b15905.

[18] E. Murugan, A. Dhamodharan, Separate and simultaneous determination of vanillin, theophylline and caffeine using molybdenum disulfide embedded polyaniline/graphitic carbon nitrite nanocomposite modified glassy carbon electrode, Diam. Relat. Mater. 120 (2021). https://doi.org/10.1016/J.DIAMOND.2021.108684.

[19] R. Yang, Y. Fan, R. Ye, Y. Tang, X. Cao, Z. Yin, Z. Zeng, MnO2-Based Materials for Environmental Applications, Adv. Mater. 33 (2021) 1–53. https://doi.org/10.1002/adma.202004862.

[20] M. Diantoro, I. Istiqomah, Y. Al Fath, N. Nasikhudin, Y. Alias, W. Meevasana, Potential of MnO2-based composite and numerous morphological for enhancing supercapacitors performance, Int. J. Appl. Ceram. Technol. (2023). https://doi.org/10.1111/IJAC.14377.

[21] Q.-Z. Zhang, D. Zhang, Z.-C. Miao, X.-L. Zhang, S.-L. Chou, -Z Q Zhang, D. Zhang, X.-L. Zhang, -C Z Miao, -L S Chou, Research Progress in MnO2–Carbon

Based Supercapacitor Electrode Materials, Small. 14 (2018) 1702883. https://doi.org/10.1002/SMLL.201702883.

[22] G. Elmacı, A.S. Ertürk, M. Sevim, Ö. Metin, MnO2 nanowires anchored on mesoporous graphitic carbon nitride (MnO2@mpg-C3N4) as a highly efficient electrocatalyst for the oxygen evolution reaction, Int. J. Hydrogen Energy. 44 (2019) 17995–18006. https://doi.org/10.1016/j.ijhydene.2019.05.089.

[23] M. Keerthi, S. Manavalan, S.-M. Chen, P.-W. Shen, A Facile Hydrothermal Synthesis and Electrochemical Properties of Manganese dioxide@graphitic Carbon Nitride Nanocomposite toward Highly Sensitive Detection of Nitrite, J. Electrochem. Soc. 166 (2019) B1245–B1250. https://doi.org/10.1149/2.0251914JES.

[24] A. Kaliyaraj Selva Kumar, Y. Zhang, D. Li, R.G. Compton, A mini-review: How reliable is the drop casting technique?, Electrochem. Commun. 121 (2020) 106867. https://doi.org/10.1016/J.ELECOM.2020.106867.

[25] W. Abbasi, Electrode Modification Through Chemical and Electrochemical Deposition of Polytyramine Film for Biosensing Application, (n.d.). www.ijert.org (accessed July 30, 2023).

[26] M. Razavi, A. Barras, M. Ifires, A. Swaidan, M. Khoshkam, S. Szunerits, M. Kompany-Zareh, R. Boukherroub, Colorimetric assay for the detection of dopamine using bismuth ferrite oxide (Bi2Fe4O9) nanoparticles as an efficient peroxidase-mimic nanozyme, J. Colloid Interface Sci. 613 (2022) 384–395. https://doi.org/10.1016/j.jcis.2022.01.041.

[27] Y. Yang, H. Wang, Y. Wu, X. Yu, Dual recognition strategy for selective fluorescent detection of dopamine and antioxidants based on graphite carbon nitride in human blood serum, Spectrochim. Acta - Part A Mol. Biomol. Spectrosc.

265 (2022) 120385. https://doi.org/10.1016/j.saa.2021.120385.

[28] S.K. Yadav, Rosy, M. Oyama, R.N. Goyal, A Biocompatible Nano Gold Modified Palladium Sensor for Determination of Dopamine in Biological Fluids, J. Electrochem. Soc. 161 (2014) H41–H46. https://doi.org/10.1149/2.083401jes.

[29] X. Liu, J. Liu, Biosensors and sensors for dopamine detection, View. 2 (2021) 20200102. https://doi.org/10.1002/VIW.20200102.

[30] A.J. Steckl, P. Ray, Stress Biomarkers in Biological Fluids and Their Point-of-Use Detection, ACS Sensors. 3 (2018) 2025–2044. https://doi.org/10.1021/ACSSENSORS.8B00726.

[31] J. Zhou, W. Wang, P. Yu, E. Xiong, X. Zhang, J. Chen, A simple label-free electrochemical aptasensor for dopamine detection, RSC Adv. 4 (2014) 52250–52255. https://doi.org/10.1039/C4RA08090D.

[32] S. Elhag, Z.H. Ibupoto, X. Liu, O. Nur, M. Willander, Dopamine wide range detection sensor based on modified Co3O 4 nanowires electrode, Sensors Actuators, B Chem. 203 (2014) 543–549. https://doi.org/10.1016/j.snb.2014.07.028.

[33] R.N. Aurora, D.A. Kristo, S.R. Bista, J.A. Rowley, R.S. Zak, K.R. Casey, C.I. Lamm, S.L. Tracy, R.S. Rosenberg, The Treatment of Restless Legs Syndrome and Periodic Limb Movement Disorder in Adults—An Update for 2012: Practice Parameters with an Evidence-Based Systematic Review and Meta-AnalysesAn American Academy of Sleep Medicine Clinical Practice Guideline, Sleep. 35 (2012) 1039–1062. https://doi.org/10.5665/SLEEP.1988.

[34] A. Swaidan, A. Barras, A. Addad, J.F. Tahon, J. Toufaily, T. Hamieh, S. Szunerits, R. Boukherroub, Colorimetric sensing of dopamine in beef meat using copper sulfide encapsulated within bovine serum albumin functionalized with copper

phosphate (CuS-BSA-Cu3(PO4)2) nanoparticles, J. Colloid Interface Sci. 582 (2021) 732–740. https://doi.org/10.1016/j.jcis.2020.08.057.

[35] K. Promsuwan, A. Soleh, K. Saisahas, J. Saichanapan, P. Kanatharana, P. Thavarungkul, C. Guo, C.M. Li, W. Limbut, Discrimination of dopamine by an electrode modified with negatively charged manganese dioxide nanoparticles decorated on a poly(3,4 ethylenedioxythiophene)/reduced graphene oxide composite, J. Colloid Interface Sci. 597 (2021) 314–324. https://doi.org/10.1016/j.jcis.2021.03.162.

[36] D.E. Vaillancourt, D. Schonfeld, Y. Kwak, N.I. Bohnen, R. Seidler, Dopamine overdose hypothesis: Evidence and clinical implications, Mov. Disord. 28 (2013) 1920–1929. https://doi.org/10.1002/MDS.25687.

[37] C. Zhang, J. Liu, X. Huang, D. Chen, S. Xu, Multistage Polymerization Design for g-C3N4 Nanosheets with Enhanced Photocatalytic Activity by Modifying the Polymerization Process of Melamine, ACS Omega. 4 (2019) 17148–17159. https://doi.org/10.1021/ACSOMEGA.9B01510.

[38] M.H. Alfaruqi, S. Islam, J. Gim, J. Song, S. Kim, D.T. Pham, J. Jo, Z. Xiu, V. Mathew, J. Kim, A high surface area tunnel-type α-MnO2 nanorod cathode by a simple solvent-free synthesis for rechargeable aqueous zinc-ion batteries, Chem. Phys. Lett. 650 (2016) 64–68. https://doi.org/10.1016/J.CPLETT.2016.02.067.

[39] Q. Han, C. Hu, F. Zhao, Z. Zhang, N. Chen, L. Qu, One-step preparation of iodine-doped graphitic carbon nitride nanosheets as efficient photocatalysts for visible light water splitting †, (2015). https://doi.org/10.1039/c4ta06093h.

[40] J. Shi, H. Wang, J. Nie, T. Yang, C. Ju, K. Pu, J. Shi, T. Zhao, H. Li, J. Xue, Alkali-assisted engineering of ultrathin graphite phase carbon nitride nanosheets with carbon vacancy and cyano group for significantly promoting photocatalytic

hydrogen peroxide generation under visible light: Fast electron transfer channel, J. Colloid Interface Sci. 643 (2023) 47–61. https://doi.org/10.1016/j.jcis.2023.03.209.

[41] S. Sunasee, K.H. Leong, K.T. Wong, G. Lee, S. Pichiah, I.W. Nah, B.H. Jeon, Y. Yoon, M. Jang, Sonophotocatalytic degradation of bisphenol A and its intermediates with graphitic carbon nitride, Environ. Sci. Pollut. Res. 26 (2019) 1082–1093. https://doi.org/10.1007/S11356-017-8729-7.

[42] Y. Chen, Y. Qu, P. Xu, X. Zhou, J. Sun, Insight into the influence of donor-acceptor system on graphitic carbon nitride nanosheets for transport of photoinduced charge carriers and photocatalytic H2 generation, J. Colloid Interface Sci. 601 (2021) 326–337. https://doi.org/10.1016/j.jcis.2021.05.145.

[43] C. Cheng, S. Zong, J. Shi, F. Xue, Y. Zhang, X. Guan, B. Zheng, J. Deng, L. Guo, Facile preparation of nanosized MoP as cocatalyst coupled with g-C3N4 by surface bonding state for enhanced photocatalytic hydrogen production, Appl. Catal. B Environ. 265 (2020) 118620. https://doi.org/10.1016/J.APCATB.2020.118620.

[44] S. Hu, A. Yu, R. Lu, A comparison study of sodium ion- and potassium ion-modified graphitic carbon nitride for photocatalytic hydrogen evolution, RSC Adv. 11 (2021) 15701–15709. https://doi.org/10.1039/D1RA01395E.

[45] T. Xing, L.H. Li, L. Hou, X. Hu, S. Zhou, R. Peter, M. Petravic, Y. Chen, Disorder in ball-milled graphite revealed by Raman spectroscopy, Carbon N. Y. 57 (2013) 515–519. https://doi.org/10.1016/J.CARBON.2013.02.029.

[46] S. Baskar, C.W. Liao, J.L. Chang, J.M. Zen, Electrochemical synthesis of electroactive poly(melamine) with mechanistic explanation and its applicability to functionalize carbon surface to prepare nanotube-nanoparticles hybrid,

Electrochim. Acta. 88 (2013) 1–5. https://doi.org/10.1016/j.electacta.2012.10.040.

[47] W. Huang, J. Li, Y. Xu, Nucleation and growth of porous MnO2 coatings prepared on nickel foam and evaluation of their electrochemical performance, Materials (Basel). 11 (2018). https://doi.org/10.3390/ma11050716.

[48] S. Nijjer, J. Thonstad, G.M. Haarberg, Oxidation of manganese(II) and reduction of manganese dioxide in sulphuric acid, Electrochim. Acta. 46 (2000) 395–399. https://doi.org/10.1016/S0013-4686(00)00597-1.

[49] M. Clark, D.G. Ivey, Nucleation and growth of electrodeposited Mn oxide rods for supercapacitor electrodes, Nanotechnology. 26 (2015) 384001. https://doi.org/10.1088/0957-4484/26/38/384001.

[50] M.F. Dupont, S.W. Donne, Nucleation and Growth of Electrodeposited Manganese Dioxide for Electrochemical Capacitors, Electrochim. Acta. 120 (2014) 219–225. https://doi.org/10.1016/J.ELECTACTA.2013.12.014.

[51] L. Wen-Zhi, L. You-Qin, H. Guang-Qi, Preparation of Manganese Dioxide Modified Glassy Carbon Electrode By a Novel Film Plating/Cyclic Voltammetry Method for H(2)0(2) Detection, J. Chil. Chem. Soc. 54 (2009) 2–7. https://doi.org/10.4067/s0717-97072009000400009.

[52] T.O.L. Sunde, E. Garskaite, B. Otter, H.E. Fossheim, R. Sæterli, R. Holmestad, M.A. Einarsrud, T. Grande, Transparent and conducting ITO thin films by spin coating of an aqueous precursor solution, J. Mater. Chem. 22 (2012) 15740–15749. https://doi.org/10.1039/C2JM32000B.

[53] F. Fina, S.K. Callear, G.M. Carins, J.T.S. Irvine, Structural investigation of graphitic carbon nitride via XRD and neutron diffraction, Chem. Mater. 27 (2015) 2612–2618. https://doi.org/10.1021/ACS.CHEMMATER.5B00411.

[54] H. Zhu, Y. An, M. Shi, Z. Li, N. Chen, C. Yang, P. Xiao, Porous N-doped

carbon/MnO2 nanoneedles for high performance ionic liquid-based supercapacitors, Mater. Lett. 296 (2021) 129837. https://doi.org/10.1016/J.MATLET.2021.129837.

[55] Y. Hang, C. Zhang, X. Luo, Y. Xie, S. Xin, Y. Li, D. Zhang, J.B. Goodenough, α-MnO2 nanorods supported on porous graphitic carbon nitride as efficient electrocatalysts for lithium-air batteries, J. Power Sources. 392 (2018) 15–22. https://doi.org/10.1016/J.JPOWSOUR.2018.04.078.

[56] Y. Li, S. Cao, L. Fan, J. Han, M. Wang, R. Guo, Hybrid shells of MnO2 nanosheets encapsulated by N-doped carbon towards nonprecious oxygen reduction reaction catalysts, J. Colloid Interface Sci. 527 (2018) 241–250. https://doi.org/10.1016/j.jcis.2018.05.056.

[57] H. Wang, G. Yan, X. Cao, Y. Liu, Y. Zhong, L. Cui, J. Liu, Hierarchical Cu(OH)2@MnO2 core-shell nanorods array in situ generated on three-dimensional copper foam for high-performance supercapacitors, J. Colloid Interface Sci. 563 (2020) 394–404. https://doi.org/10.1016/j.jcis.2019.12.095.

[58] X. Dai, J. Rao, Z. Bao, K. Li, L. Feng, D. Song, L. Zhao, W. Li, X. Liu, S. Yi, P. Dong, Y. Zhang, Magnetic double-core@shell MnO2@NiFe@DE as a multifunctional scavenger for efficient removal of tetracycline, anionic and cationic dyes, J. Colloid Interface Sci. 628 (2022) 769–783. https://doi.org/10.1016/j.jcis.2022.07.187.

[59] F. Yang, M. Lublow, S. Orthmann, C. Merschjann, T. Tyborski, M. Rusu, S. Kubala, A. Thomas, R. Arrigo, M. Hävecker, T. Schedel-Niedrig, Metal-free photocatalytic graphitic carbon nitride on p-type chalcopyrite as a composite photocathode for light-induced hydrogen evolution, ChemSusChem. 5 (2012) 1227–1232. https://doi.org/10.1002/cssc.201100691.

[60] X. Li, J. Zhang, L. Shen, Y. Ma, W. Lei, Q. Cui, G. Zou, Preparation and characterization of graphitic carbon nitride through pyrolysis of melamine, Appl. Phys. A Mater. Sci. Process. 94 (2009) 387–392. https://doi.org/10.1007/S00339-008-4816-4.

[61] Y. Liu, S. Zhao, C. Zhang, J. Fang, L. Xie, Y. Zhou, S. Zhuo, Hollow tubular carbon doping graphitic carbon nitride with adjustable structure for highly enhanced photocatalytic hydrogen production, Carbon N. Y. 182 (2021) 287–296. https://doi.org/10.1016/J.CARBON.2021.06.008.

[62] K. Yadav, S. Garg, A.K. Singh, S. Singh, A. Singh Parmar, Rosy, Protein nano Dots conjugated AuNP, poly-Lysine biointerface for the selective voltammetric estimation of Melatonin in pharmaceutical and food samples, Microchem. J. 179 (2022) 107563. https://doi.org/10.1016/J.MICROC.2022.107563.

[63] M. Wang, M. Zhang, J. Zhu, J. Wang, L. Hu, T. Sun, M. Wang, Y. Tang, g-C3N4/Co Nanohybrids for Ultra-sensitive Simultaneous Detection of Uric Acid and Dopamine, ChemElectroChem. 7 (2020) 1373–1377. https://doi.org/10.1002/CELC.201902165.

[64] S. Vinoth, R. Ramaraj, A. Pandikumar, Facile synthesis of calcium stannate incorporated graphitic carbon nitride nanohybrid materials: A sensitive electrochemical sensor for determining dopamine, Mater. Chem. Phys. 245 (2020) 122743. https://doi.org/10.1016/j.matchemphys.2020.122743.

[65] H. Zhang, Q. Huang, Y. Huang, F. Li, W. Zhang, C. Wei, J. Chen, P. Dai, L. Huang, Z. Huang, L. Kang, S. Hu, A. Hao, Graphitic carbon nitride nanosheets doped graphene oxide for electrochemical simultaneous determination of ascorbic acid, dopamine and uric acid, Electrochim. Acta. 142 (2014) 125–131. https://doi.org/10.1016/J.ELECTACTA.2014.07.094.

[66] L. Zhang, C. Liu, Q. Wang, X. Wang, S. Wang, Electrochemical sensor based on an electrode modified with porous graphitic carbon nitride nanosheets (C3N4) embedded in graphene oxide for simultaneous determination of ascorbic acid, dopamine and uric acid, Microchim. Acta. 187 (2020). https://doi.org/10.1007/s00604-019-4081-6.

[67] Q. Li, Y. Xia, X. Wan, S. Yang, Z. Cai, Y. Ye, G. Li, Morphology-dependent MnO2/nitrogen-doped graphene nanocomposites for simultaneous detection of trace dopamine and uric acid, Mater. Sci. Eng. C. 109 (2020) 110615. https://doi.org/10.1016/J.MSEC.2019.110615.

[68] Z. Yao, X. Yang, Y. Niu, F. Wu, Y. Hu, Y. Yang, Voltammetric dopamine sensor based on a gold electrode modified with reduced graphene oxide and Mn3O4 on gold nanoparticles, Microchim. Acta. 184 (2017) 2081–2088. https://doi.org/10.1007/s00604-017-2210-7.

[69] B. Yang, J. Wang, D. Bin, M. Zhu, P. Yang, Y. Du, A three dimensional Pt nanodendrite/graphene/MnO2 nanoflower modified electrode for the sensitive and selective detection of dopamine, J. Mater. Chem. B. 3 (2015) 7440–7448. https://doi.org/10.1039/c5tb01031d.

[70] Rosy, R.N. Goyal, Estimation of Amoxicillin in Presence of High Concentration of Uric Acid and Other Urinary Metabolites Using an Unmodified Pyrolytic Graphite Sensor, J. Electrochem. Soc. 162 (2015) G8–G13. https://doi.org/10.1149/2.0691501JES.

Chapter 2

Second Part

2.2. Introduction

The commercialization of SPEs into the market greatly transformed the use of electrochemical sensors in portable sensing devices. Since their inception in the 1990s[1], screen-printed electrodes (SPEs) have been widely used in several sectors, such as microbiology[2], environmental[3,4], clinical[5], food measurement[6] and industrial analyses[7]. In contrast to the conventional electrode substrates, SPE offers several advantages. A few are, their cost-effectiveness, portability, and trace volume requirements[8,9]. However, SPEs are often associated with low sensitivity, surface instability, and fouling issues. Therefore, it is crucial to improve the SPE's stability, reliability, and discrimination ability, especially for point-of-care (PoC) applications. One of the primary approach to enhance the electrochemical efficacy in terms of sensitivity and selectivity is the surface modification of the electrode[10].

2D materials have emerged as a potential recognition element for various sensing techniques[11,12]. Graphitic carbon nitride (gCN), a well-established 2D polymeric material has recently surged interest owing to its exceptional and distinctive characteristics. It's π-conjugated structure allows it to engage with a diverse array of organic molecules via π-π interaction [13]. The presence of N atoms and strong C-N covalent nature of bonds, in lieu of the C-C bonds, further adds to its superior chemical and mechanical characteristics. The ability of nitrogen atoms to function as effective electron-donating site makes them specifically appealing for catalytic processes[14]. Nevertheless, the practical application of gCN is constrained by its low electrical conductivity, obstructed charge transfer, and inadequate solubility in solvents which restricts its applicability in electrochemical systems[15,16]. To effectively address these constraints, it was ascertained that the optimal approach would involve tailoring gCN with heteroatoms through doping or surface impregnation[17].

Manganese oxide (Mn_xO_y) nanoparticles are particularly advantageous for electrochemical applications. Their diverse structural configurations and mixed manganese valencies (+4, +3, +2) facilitate multiple redox processes. Over the years, a range of Mn_xO_y nanostructures has been effectively synthesized and employed as electrode material in super capacitors and electrochemical sensor [18–24]. Nevertheless, the limited electrochemical faradaic capabilities of Mn_xO_y can be ascribed to its insufficient electronic conductivity, inadequate interfacial contact, and chemical and structural instabilities. On careful analysis, it was realized that its hybridization with gCN can mitigate the chemical and structural instabilities of the Mn_xO_y. Abundant N-sites within gCN are expected to offer increased metal coordination sites[25,26]. However, Mn_xO_y will preferentially engage with the π-conjugated electrons of the gCN to electrocatalyze the oxidation of biomolecules. It is anticipated that unbound loan pair electron density of Nitrogen in gCN coating will engender a proclivity for connection with Mn_xO_y, ultimately results to the production of a robust composite synergistically inheriting the beneficial traits of both materials.

Our group has recently published a study on a single-step process for electrodeposition of gCN and its simultaneous decorating with MnO_2 on indium tin oxide coated glass.[27] The reported electrodeposition was effective for the creation of gCN modified coating. The method, however, relied on two components: gCN suspension and manganese (II) acetate. As a result, optimizing both components made the process tedious. The inadequate dispersibility of gCN was another problem that hindered the material's effective mass transfer. Instead of merely implementing surface decoration, Mn_xO_y could have been incorporated within the gCN to increase the observed improvement. Therefore, as a continuation of our previous work, we present the synthesis, characterization, and electrodeposition of Mn_xO_y incorporated gCN. Due to the synergistic interaction of

Mn_xO_y and gCN during the synthesis, significantly improved dispersibility and exfoliated structures were observed, eliminating the need for single-component optimization. To capitalize on the broad applicability of the suggested strategy, its effectiveness in enhancing the sensing properties of commercial screen-printed electrodes has been further examined.

Dopamine (DA) has been selected as the test analyte to assess the practical feasibility of the modified electrode. DA is a well-established neurotransmitter within the central nervous system, and it holds significant influence over various physiological processes [28,29]. An optimal level of DA contributes to the regularity of movements, while abnormally high DA levels are a warning sign of cardiotoxicity, erratic cardiac rhythms, elevated blood pressure, cardiac failure, and drug addiction.[30,31]. Conversely, a diminished level of DA is implicated in the development of Parkinson's disease[32], Alzheimer's disease[33], HIV infection[34], restless legs syndrome (RLS)[35], attention deficit hyperactivity disorder (ADHD)[36], schizophrenia[37], anorexia[38], Huntington's disease[39], and various other neurological disorders. Many dopamine stimulants/dopamine-receptor antagonists are also prohibited, as per the world anti-doping agency.

Therefore, testing DA is vital for medical diagnosis and unethical practices in sports, clubs, etc. Consequently, the developed gCN.MnO_2 modified SPE was employed for both the qualitative and quantitative estimation of DA. The pragmatic applicability was also tested by checking the efficacy of the designed sensor for quantifying DA in clinical and food samples.

2.2.2. Experimental

2.2.2.1 Materials

Indium Tin Oxide (ITO) coated glass slides having a resistance of 18 Ω were obtained from DTech Solutions (Kanpur, India). Carbon based SPEs with working electrode of 3 mm diameter disk were procured from Zensor R&D Co., Ltd. Analytical grade dopamine hydrochloride, melamine, manganese acetate, ethanol, potassium ferricyanide, potassium chloride, uric acid, tryptophan, melatonin, lysine, cysteine, creatinine, p-nitrophenol, sodium chloride, Urea, dextrose anhydrous, sodium dihydrogen phosphate, ortho-phosphoric acid, and disodium hydrogen phosphate were purchased from Alfa Aesar. The chemicals were utilized as-received without undergoing additional purification procedures. A 0.1 M phosphate buffer solution was prepared using the procedure described by Christian and Purdy.[40] Deionized water obtained from Milli-Q ultrapure water purifier was used for preparing all the stock solution and test aliquots.

2.2.2.2 Synthesis of gCN.Mn_xO_y composites

The gCN and Mn_xO_y composites were prepared through direct thermal treatment of melamine and manganese acetate, with certain modifications as previously documented in existing literature[27]. In summary, a mixture comprising 7 grams of melamine powder and 3 grams of manganese acetate was loaded into an alumina crucible and introduced into a muffle furnace. The furnace was subjected to a gradual increase in temperature at a ramp rate of 6 ℃/min until it reached 600 ℃, where it was maintained constant for a period of 6 hours. After cooling the furnace to ambient temperature, the crucible was taken out and a dark-hued powder was extracted and labelled as 7:3 gCN.Mn_xO_y. The obtained material was pulverized using a mortar and pestle and subsequently utilised for characterization. The same procedure was repeated for a mixture comprising 9 grams of melamine powder and 1 grams of manganese acetate and the obtained powder is titled as 9:1 gCN.Mn_xO_y.

2.2.2.3 Characterization details

The X-ray Diffractometer (Rigaku miniflex 600, Japan) was utilized to obtain the crystallographic data of the synthesized material, employing a Cu-Kα radiation source. The surface functionalities of gCN. Mn_xO_y were analyzed through Fourier-transform infrared (FT-IR) spectroscopy, which was conducted within the wavenumber range of 550 – 4000 cm^{-1} with a resolution of 4 cm^{-1}, utilizing the Thermo ScientificTM Nicolet iD7 spectrometer. The ZEISS EVO scanning electron microscope was utilized at 20 kV to extract surface and morphological information. The elemental analysis of the material, and modified electrode surfaces was conducted using a K-Alpha X-ray photon spectrophotometer manufactured by Thermo Fisher Scientific. The device was equipped with a micro-focused X-ray source that utilised monochromatic Al Kα radiation with an energy range of 100-4000 eV. The atomic force microscopy was opted for surface analysis using the NTEGRA Prima scanning probe microscope, manufactured by NT-MDT Service & Logistics Ltd.

2.2.2.4 Electrochemical measurements

The electrochemical measurements were conducted using a PalmSens3 voltammetric analyzer. The optimisation study employed a three-electrode system comprising of a reference electrode of Ag/AgCl (3M KCl), a counter electrode of platinum wire, and a working electrode of ITO-coated glass. After careful optimization and characterization of the electrodeposition protocol, it is then tested for improving commercial carbon ink based SPE's with a 3 mm diameter disk as working electrode manufactured by Zensor R&D Co. Ltd. Qualitative and quantitative voltammetric analysis of DA was carried out using the unmodified and modified SPE. The electrodeposition processes were facilitated by the use of 1M KCl as a supporting electrolyte. Phosphate buffer with a pH of 7.4 was used as the supporting electrolyte for all other investigations.

2.2.2.4.1 Electrodeposition of gCN.MnO_2 composite

The ITO coated glass slides were cleaned with deionized water (DI), ethanol, and isopropyl alcohol prior to electrodeposition. 10 mg/mL gCN.Mn_xO_y suspension was prepared by ultrasonically suspending 100 mg of gCN.Mn_xO_y composite in 10 mL of DI using a bath sonicator for 4 hours. The aliquot for electrodeposition was prepared by adding 1 mL of the prepared gCN.Mn_xO_y suspension in an electrochemical cell containing 1 mL of 1M KCl. The electrodeposition was carried out employing cyclic voltammetry (CV). The potential was scanned between -1.0 V and +1.6 V at a scan rate of 100 $mV.s^{-1}$ in the prepared aliquot using pre-cleaned ITO/SPE as the working electrode. The requisite number of scans (n) utilised for electrodeposition was optimized by varying 'n' in the range of n = 5 to 25. The SPE has been electro-functionalized by running the optimized number of CV cycles (n=20) at a scan rate of 100 mV/s using 60 µL of 1 mg/mL 7:3 gCN.Mn_xO_y suspension.

Following the completion of the necessary scans, the ITO/SPE was rinsed using DI water and was subsequently dried at ambient temperature. The electrodeposited electrode is referred as gCN.MnO_2|ITO or gCN.MnO_2|SPE in the subsequent text.

2.2.2.4.2 Electroanalytical technique and sample preparation

The optimum number of electrodeposition cycles was chosen using a comparative assessment of the electrochemical response of the modified electrodes. In order to conduct a comparative evaluation, the SWV response of the individually modified scaffold was recorded in 1:1 solution of 1 mM $K_3[Fe(CN)_6]$ and 1 M KCl, at a scan rate of 100 mV/s. The measurements were taken within a potential range of -0.2 V to +0.6 V. 50 µL of the prepared solutions were drop-casted on to SPE for all the electrochemical measurements.

The suitability of the electrodeposited surface for voltammetric sensing applications was assessed by utilising DA as the test analyte. A 5 mM stock solution of DA was prepared by dissolving the appropriate amount of dopamine hydrochloride in DI for the purpose of conducting qualitative and quantitative electroanalytical investigations. To prevent light induced degradation of DA, the stock solution was stored in a dark environment. The dilution method was employed to prepare DA solutions of varying concentrations. A consistent volume of PB-7.4, specifically 1 mL, was maintained across all aliquots. The remaining 1 mL comprised the necessary amount of DA stock solution and deionized water. The electrochemical characteristics of DA were examined using square wave voltammetry (SWV). The SWV were recorded within the voltage range of 0.0 to 0.5 V, with a step size of 6 mV. The most favourable values for amplitude and frequency were determined to be 25 mV and 10.0 Hz. Following each SWV scan, the sensor surface was rinsed with deionized water and was subsequently stabilised by recording five SWVs in a buffer solution, all within the working potential range.

2.2.2.4.3 Real sample preparation and validation:

Dopamine hydrochloride injection (Domin, Neon Laboratories Limited, India) was purchased from the local medical store and used for preparing the test solution.

25 g of banana peel was first chopped into small pieces, crushed using a mortar-pestle, then diluted with 10 mL of DI water. The solution was then filtered to extract the DA. Then, 100 µL of the filtered extract solution was poured in a glass cell already having 1 mL of PB 7.4. The solution was made to 2 mL by adding the remaining volume of DI water.

Urine sample of a healthy volunteer was collected, filtered and diluted 5-fold with DI. The sample was used as such without any pre-treatment process.

UV absorbance spectra of dopamine hydrochloride was recorded. The absorbance spectrum showed a λ_{max} = 280 nm.[41] The band was found to increase with increasing DA concentration. The observed absorbance versus concentration was plotted and the resulting calibration curve was used to calculate the concentration of unknown sample.

2.2.3. Results and Discussion

2.2.3.1 Material Characterization: Examining the two gCN.Mn_xO_y composites

The physical, chemical, and topographical properties of the synthesized gCN.Mn_xO_y composites were investigated using various characterization methods. X-ray diffraction analysis (XRD) was first carried out to ascertain the crystallinity and composition of the two composites. **Figure 2.2.1(a)** shows the characteristic diffraction patterns of the synthesized gCN.Mn_xO_y composites. The X-ray diffractogram of 7:3 gCN.Mn_xO_y showcases characteristic peaks of gCN, MnO_2, and, Mn_2O_3. The most intense peak at 32.9° along with other peaks at 23.1°, 45.1°, and 55.1° corresponds to the (222), (211), (332), (440), planes of Mn_2O_3 (denoted by Ψ)[42,43], respectively. Whereas, peaks at 2θ values at 17.9°, 28.8°, 36.0°, 38.1°, 49.4°, and 65.6° correspond to (200), (310), (400), (211), (411), (002) planes of MnO_2 (denoted by ∗)[44], respectively. A small peak at ca. 27.6° signifies the (002) plane of gCN (denoted by #) arising due to the stacked layered arrangement of a typical conjugated aromatic ring[45]. The low intensity of the gCN peak is attributed to its significantly low crystallinity compared to Mn_2O_3 and MnO_2. Compared to 7:3 gCN.Mn_xO_y, 9:1 samples exhibited more prominent peaks corresponding to graphitic carbon nitride with a visible in-plane packing of aromatic triazine ring peak at 13.1°. Additionally, the XRD peaks for Mn_2O_3 were less intense in the case of 9:1 gCN.Mn_xO_y. It was observed that the increased Mn concentration in the 7:3 gCN.Mn_xO_y facilitated the formation of Mn_2O_3 in addition to MnO_2 and reduced the content of graphitic-like stacked layer structures of the conjugated aromatic systems at

ca. 27.6°. The absence of gCN peaks indicates its existence in amorphous state. The increased amorphous character of gCN can be explained on the basis of increased defects and creation of N vacancies with increasing Mn content.[46]

Subsequently, Fourier-transform infrared (FT-IR) spectroscopy was employed to get valuable insights on the chemical bonds and functional groups present in the material under investigation. The FT-IR spectra of the two gCN.Mn_xO_y composites are depicted in **Figure 2.2.1(b)**. Both the spectra showcased a broad peak in the frequency range of 3000 and 3500 cm^{-1} arising because of the O-H bonds and the NH_2 group in close proximity to the sp^2 hybridized carbon atom. Several peaks within the spectral range of 1100-1600 cm^{-1} can be attributed to the different vibration modes of the C-N bonds present in the polymeric triazine rings of gCN and are discussed below. The spectral bands located at 1245 cm^{-1} and 1322 cm^{-1} are attributed to the stretching vibrations of C-NH-C or (N-$(C)_3$), respectively. The intense bands at 1419 cm^{-1} and 1629 cm^{-1} have been attributed to the aromatic C=N vibrations of stretching mode. The signal observed at a wavenumber of 810 cm^{-1} corresponds to the distinctive tris-triazine breathing mode confirming the presence of gCN in the composites[47,48]. The weak absorption bands observed at 1033 cm^{-1} and 1617 cm^{-1} have been speculated to be due to O-H bending vibrations bound to Mn atoms. Furthermore, the intense absorption band at 520 cm^{-1} is a signature of Mn-O vibrations which manifests the presence of Mn_xO_y in the synthesised composite[49]. Interestingly, the FT-IR spectra of 9:1 gCN.Mn_xO_y exhibited two main differences. Firstly, the multiple peaks arising from the gCN moieties are much more intense, suggesting that the 9:1 sample contains more gCN like structures than the 7:3 sample. Secondly, the peak at 520 cm^{-1} is much weaker compared to 7:3 sample, which can be ascribed to the low manganese content. Thus, the FT-IR analysis supports the inferences made from XRD, confirming the formation of composite having

characteristics of both gCN and Mn_xO_y. As expected, the 7:3 gCN.Mn_xO_y manifests more Mn_xO_y content compared to the 9:1 sample.

The X-ray photoelectron spectroscopy was next employed to get more insights about the chemical composition and chemical state of the elements present in the synthesised materials. A detailed comparison was made using the high-resolution XPS spectra of the Mn, C, N, and O as presented in **Figure 2.2.1(c-f)**. **Figure 2.2.1(c)** illustrates the comparative analysis of Mn 2p XPS spectra corresponding to 9:1 and 7:3 gCN.Mn_xO_y. The spectra showcase two peaks corresponding to Mn $2p_{3/2}$ and $2p_{1/2}$ indicating the presence of Mn_xO_y. The more intense peaks

in 7:3 sample suggests a higher concentration of Mn_xO_y. The Mn $2p_{3/2}$ for the 7:3 sample was found to be shifted to 641.4 eV compared to 641.2 eV for 9:1 sample. Similarly, the $Mn2p_{1/2}$ in the 9:1 sample exhibit peaks at a binding energy of 652.7 eV, whereas the 7:3 sample displays peaks at a binding energy of 653.1 eV[50]. The shift in binding energies to higher values hints towards the partial change in the oxidation state of Mn and can be explained on the basis of increase in the number of electronegative oxygen atoms which was also interpreted from the O1s spectra shown in **Figure 2.2.1(d)**[51]. As witnessed from the O1s, Both the samples showed two signals, one at the binding energy of 529.3 eV, associated with the Mn-O-Mn link, and another at the binding energy of 531.5 eV, associated with the Mn-O-H bond[52]. Both of these peaks are more prominent in the 7:3 sample compared to 9:1, indicating a higher concentration of Mn_xO_y.

The N 1s spectra (**Figure 2.2.1(e)**) of the 9:1 sample showcased three signals at binding energies of 398.2 eV, 400.8 eV, and 403.6 eV that arises from various nitrogen environments in the triazine structural unit of gCN. The N atoms that are sp^2-bonded to two carbon atoms (C=N-C) are responsible for the peak at 398.2 eV. The N-H groups of

open ends in the graphitic carbon nitride network are responsible for the peak at 400.8 eV.

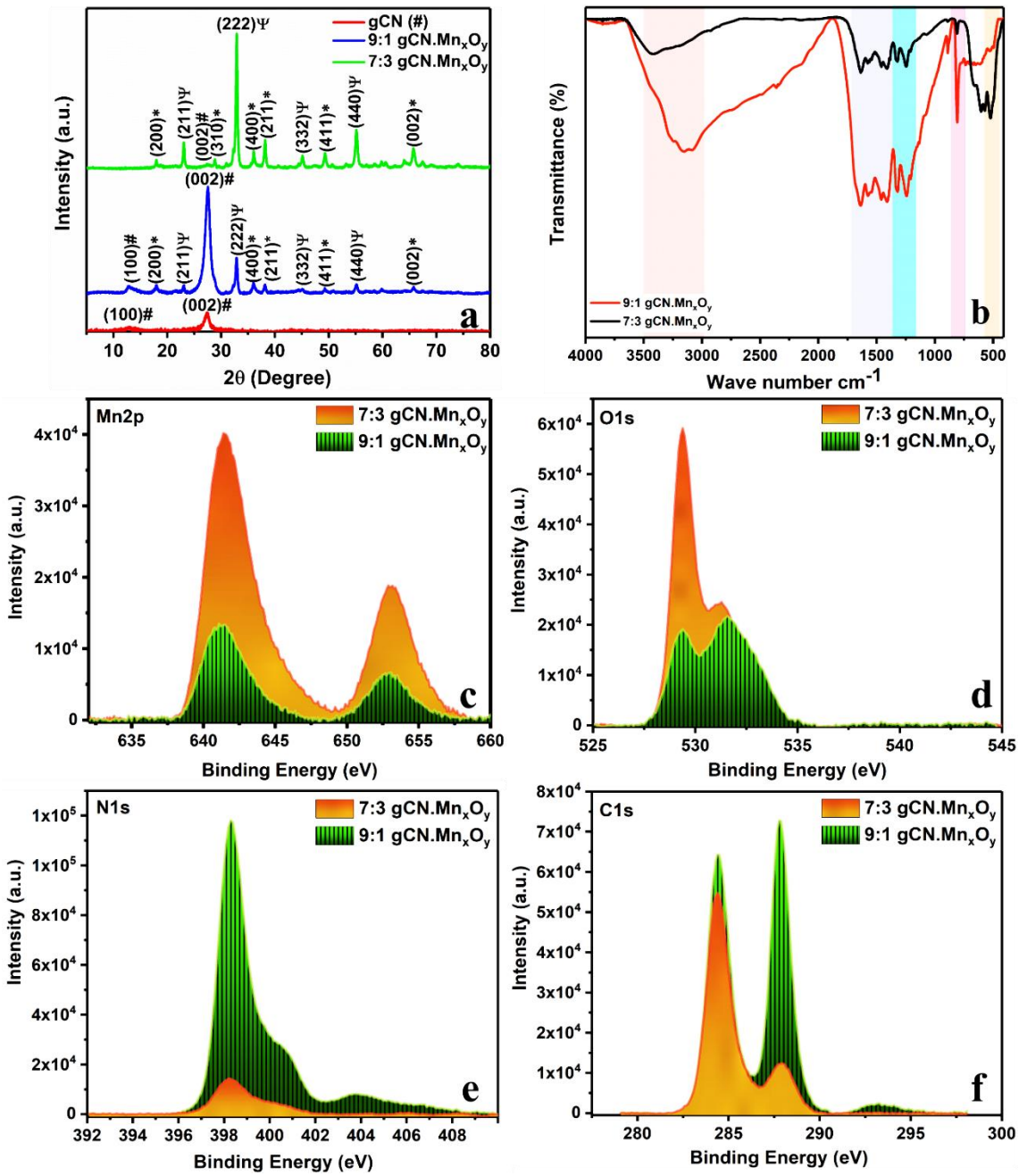

Figure 2.2.1: (a) X-ray diffractogram of gCN, and gCN.Mn_xO_y composites. (b) FT-IR spectra of synthesized 9:1 and 7:3 gCN.Mn_xO_y composites. Comparative XPS plots of (c) Mn 2p, (d) O1s, (e) N1s and (f) C1s corresponding to 9:1 and 7:3 gCN.Mn_xO_y composites.

The oxidised nitrogen species, such as pyridine-N-oxides, emerge in the N 1s spectra at the binding energy 403.6 eV, suggesting the interaction of N with the oxygen-containing species (Mn_xO_y). In contrast, in the 7:3 sample, the intensity of the first two peaks

decreases, and the peak at 403.6 eV disappeared. The decreased intensity of the N1s suggests the decreased amount of gCN in 7:3 sample which was also concluded from the XRD and FT-IR analysis. This was further confirmed from the comparative analysis of C1s as shown in **Figure 2.2.1(f)**. Both the spectra show two common peaks at 284.6 eV and 288.2 eV. The binding energies at 284.6 eV can be attributed to the C-C coordination of the surface adventitious carbon, and the signal at 288.2 eV can be assigned to sp^2-bonded carbon (N-C=N) in the aromatic rings. The lower intensity of these two peaks in the 7:3 sample further indicates a composition containing less graphitic carbon nitride. In addition to this peak, the 9:1 sample also shows an additional peak at binding energy of 293.3 eV that could be caused by π electron delocalization in heptazine units sp^2 carbon[53]. This peak does not appear in the 7:3 sample because of the low levels of gCN.

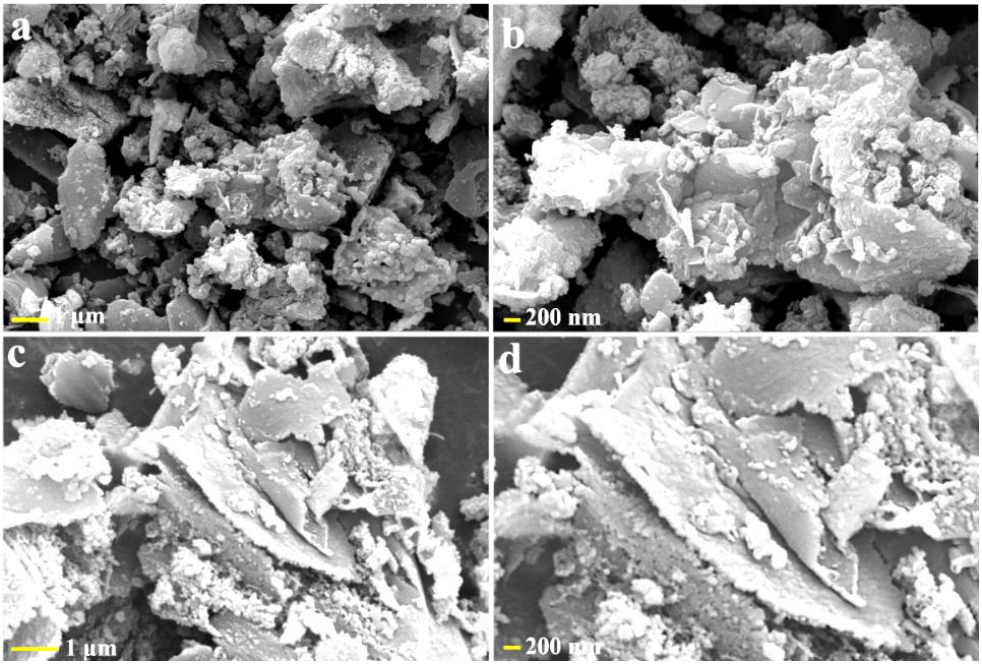

Figure 2.2.2: Scanning electron microscopy images of (a,b) 9:1 gCN.Mn_xO_y and (c,d) 7:3 gCN.Mn_xO_y composite.

The structural morphology of the as-synthesized composite was then investigated using scanning electron microscopy (SEM). **Figure 2.2.2** shows scanning electron micrographs of both the gCN.Mn_xO_y composite. The 9:1 gCN.Mn_xO_y composite was found to exist in

micron sized thick rock like structures. Whereas, thin 1-4 µm sized sheets of gCN were found to be uniformly decorated with Mn_xO_y nanoparticles in case of 7:3 gCN.Mn_xO_y. The elemental mapping shown in **Figure 2.2.3** confirms the uniform distribution of carbon, nitrogen, oxygen, and manganese over the scanned area, demonstrating the synthesis of gCN.Mn_xO_y composite. The energy dispersive X-ray spectroscopy (EDX) also confirmed nearly three times higher atomic percentage of Mn in 7:3 sample compared to 9:1 gCN.Mn_xO_y validating the conclusions obtained from XRD, FT-IR and XPS analysis. In addition, the 7:3 gCN.Mn_xO_y exhibited substantially improved dispersibility in water compared to bulk gCN as well as 9:1

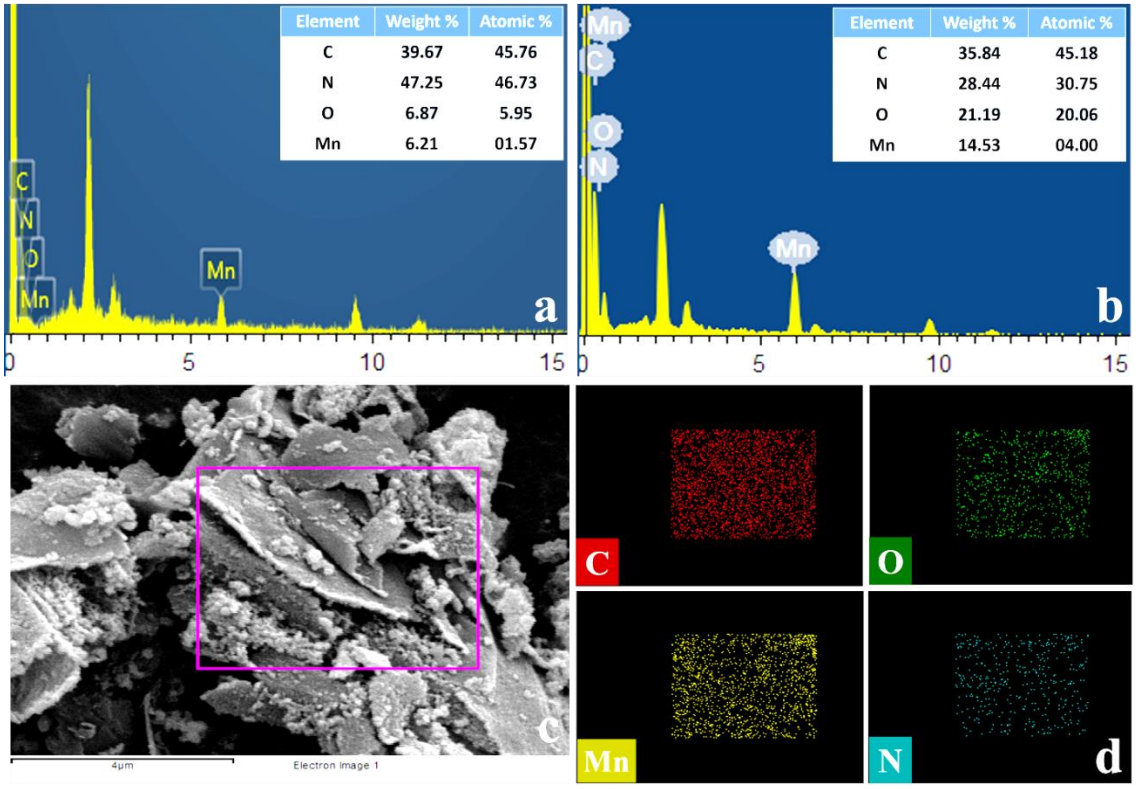

Figure 2.2.3: EDX of (a) 9:1 gCN.Mn_xO_y (b) 7:3 gCN.Mn_xO_y material. (c-d) Elemental mapping of 7:3 gCN.Mn_xO_y showing uniform distribution of C, O, Mn and N over the scanned area.

gCN.Mn_xO_y. The increased Mn content, thin sheet like morphology and improved dispersibility of 7:3 gCN.Mn_xO_y materials are expected to be favourable for electrochemical surface decoration. Therefore, following a comprehensive analysis of the

material properties, the potential advantages of gCN.MnO_2 composite in augmenting the electrochemical traits of a conducting framework was explored.

2.2.3.2 gCN.MnO_2 electrodeposition and unveiling the underlying mechanism:

The protocols opted for the electrodeposition of gCN.MnO_2 using both the gCN.Mn_xO_y composites have been described in the experimental section.

Figure 2.2.4(a-d) presents the cyclic voltammograms observed during the electrodeposition of gCN.Mn_xO_y for both the compositions. The electrochemical traits of both gCN and Mn_xO_y were observed during the electrodeposition. The first cyclic voltammograms of both the compositions hints towards four major electrochemical processes as shown in **Figure. 2.2.4(a)**. The first peak observed at 0.30 V corresponds to the oxidation of Mn (II) to Mn (III). A weak bump centred at ~0.5 V represents the oxidation of unbound amino groups of gCN monomer units. The Mn (III) so formed being metastable in the mildly acidic conditions chemically hydrolyses to MnOOH and oxidises to MnO_2 on scanning the potential leading to the next peak at ~0.8 V. An additional small peak indicating formation of radical cations at around 1.12 V was observed explicitly during the first cycle which is responsible for initiating the electropolymerization of gCN moieties[54]. In the reverse sweep, the reduction of MnO_2 to MnOOH and Mn^{2+} takes place corresponding to the peak at 0.8 V, 0.4 V, and 0 V, respectively[55–58]. The comparative analysis of the first and second electrodeposition cycle (**Figure 2.2.4(a,b)**) showcase the more pronounced peak at 0.8 V in case of 7:3 gCN.Mn_xO_y, which univocally confirms the increased Mn content especially in +3 state (as Mn_2O_3) compared to 9:1 gCN.Mn_xO_y. **Figure 2.2.4(c,d)** presents the complete electrodeposition cycles for both the materials. In both the cases, the observed currents for the peak at 0.8 V increased with the increasing number of deposition cycles indicating the successful electrodeposition of conducting gCN.MnO_2. Conversely, the peak current of Mn (II) to

Mn (III) was found to decrease with the increasing number of cycles indicating the decreasing availability or consumption of free Mn (II) with the progress of electrodeposition. As the electrodeposition progresses, the oxidation peak of MnOOH was found to shift to higher potentials. This can be attributed to the stabilization of Mn^{+3} by gCN that can potentially be explained by the interaction between the lone pairs of nitrogen and the manganese atom. It was evident from the cyclic voltammograms that both the composites proceed through similar electrodeposition mechanistic. However, the currents observed for 7:3 was significantly larger than that of 9:1 gCN.Mn_xO_y.

Next, the effect of surface modification on the electrochemical performance of the electrode was monitored. **Figure 2.2.4(e)** presents the comparative electrochemical response of 0.5 mM $K_3[Fe(CN)_6]$ in KCl observed using Bare ITO, gCN modified ITO, 9:1 and 7:3 gCN.Mn_xO_y modified ITO as the working electrode. As evident form the figure, all the three surface modifications resulted in improved peak current. However, 7:3 gCN.Mn_xO_y exhibited the highest improvement with approximately 2 fold higher peak current compared to the bare. As a result, the electrodeposition of gCN.MnO_2 using 7:3 gCN.Mn_xO_y was further optimised to achieve the best possible electrochemical response. During the electrodeposition, all possible Mn^{x+} state is being converted to MnO_2, the modified electrode is thus referred to gCN.MnO_2|ITO in the following text.

2.2.3.2.1 Protocol Optimization

The electrocatalytic behaviour of a modified electrode is influenced by the thickness of the electrodeposited layer. Therefore, in order to get the desirable electrochemical performance, it is necessary to optimise the thickness of the electrodeposited layers by varying the electrodeposition parameters namely, scan rate and number of scans. Where the number of scans is directly related to the repeated cycles of electro-functionalization, scan rate offers a control over the extent of redox process during one such scan. Thus, the

electro-functionalization protocol was optimized by carrying out a series of electro-functionalization experiments, first by varying the number of deposition cycles (n) from 15 to 25 and then by varying the scan rate from 25-200 mV/s. A comparative assessment was made by measuring the SWV peak current of 0.5 mM $K_3[Fe(CN)_6]$ solution using the electro-functionalized ITO as the working electrode. **Figure 2.2.4(f)** illustrates the increase in peak current with increasing number of deposition cycles up to n = 20. However, a slight decrease in current response was observed for n > 20 owing to the electrodeposition of a thicker $gCN.MnO_2$ layer. This thicker layer act as a mechanical barrier hindering electron transfer from the working electrode to the analyte. As a result, a compromised electrochemical performance was observed. Based on the obtained results, it can be concluded that the optimised surface modification process necessitated a total of 20 scans.

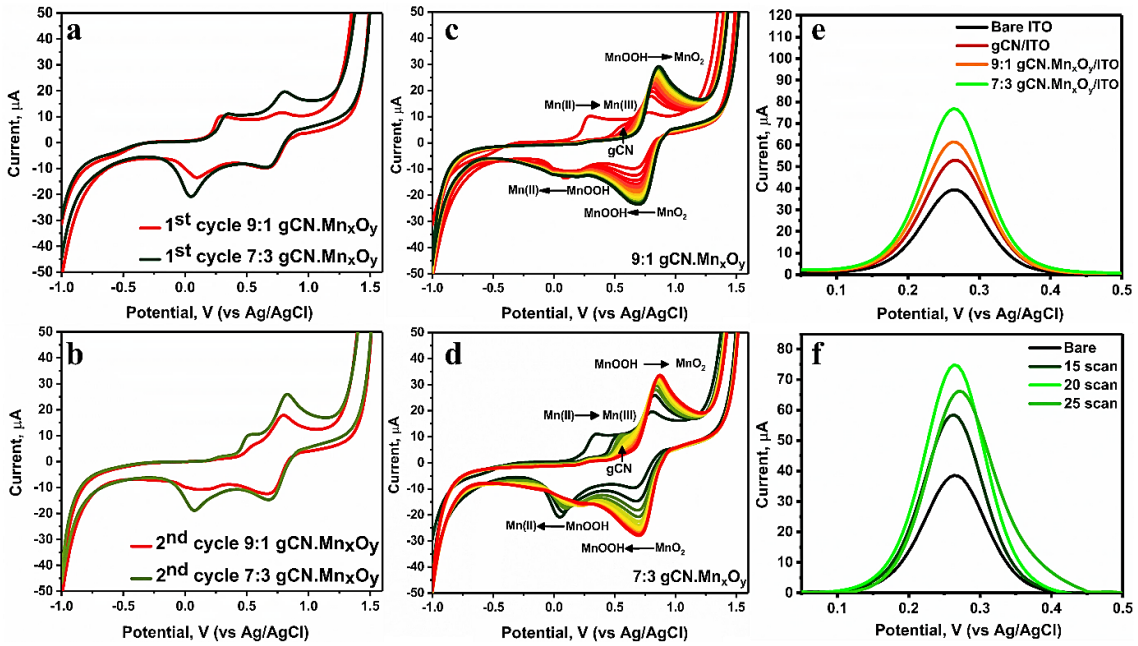

Figure 2.2.4: (a,b) Comparative first (a) and second (b) cyclic voltammograms observed during electrodeposition of 9:1 and 7:3 $gCN.Mn_xO_y$ composite. Full electrodeposition cyclic voltammograms observed for (c) 9:1 $gCN.Mn_xO_y$ (d) 7:3 $gCN.Mn_xO_y$. (e) Square wave voltamograms observed for Bare ITO, gCN|ITO, 9:1 $gCN.Mn_xO_y$|ITO and 7:3 $gCN.Mn_xO_y$|ITO for 0.5 mM $K_3[Fe(CN)_6]$ in KCl. (f) Square wave voltammograms observed for 0.5 mM $K_3[Fe(CN)_6]$ in KCl as a function of different number of electrodeposition scans using 7:3 $gCN.MnO_2$|ITO.

Next the scan rate was optimised by fixing the electrodeposition cycles to 20. As depicted in **Figure 2.2.5**, gCN.MnO_2 exhibited the highest peak current when the scan rate was set at 100 mV/s, outperforming all other scan rates. A two-fold increase was observed in comparison to the unmodified electrode. The findings suggest gCN.MnO_2 modified ITO fabricated using 20 electrodeposition cycles at a scan rate of 100 mV/s exhibits the best electrochemical performance owing to the increased number of electrochemically accessible sites and facilitated electron transfer.

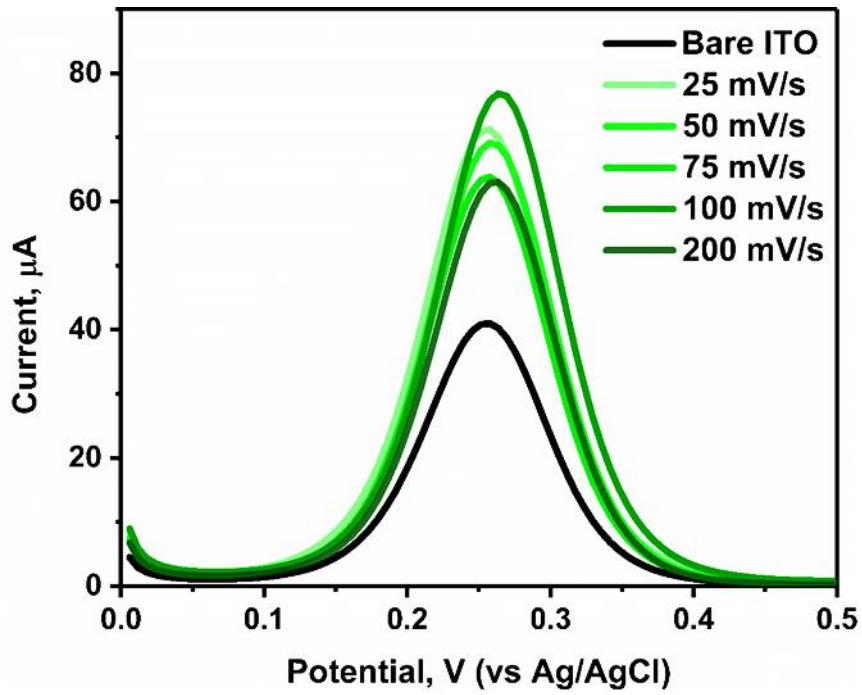

Figure 2.2.5: Square wave voltammograms observed for 0.5 mM $K_3[Fe(CN)_6]$ in KCl as a function of scan rate employed for the electrodeposition of gCN.MnO_2 using 7:3 gCN.Mn_xO_y.

2.2.3.2.2 Surface Characterization

Next, the surface morphology, composition and topography of the electrodeposited layer was analysed employing several techniques like Scanning Electron Microscopy (SEM), X-ray Photoelectron Spectroscopy (XPS), and Atomic Force Microscopy (AFM). The changes brought by electro-functionalization were visually attested by HR-SEM images of the uncoated ITO and the gCN.MnO_2|ITO shown in **Figure 2.2.6(a,b)**. Compared to

blank ITO, a clear topographical changes were observed in the HR-SEM images of gCN.MnO_2. The gCN.MnO_2 electro-functionalised ITO demonstrated the plate like characteristic structures similar to gCN which were found to be decorated with the nano-petals of MnO_2. The energy dispersive spectroscopy revealed ~20 atomic % of Mn to 39.2 atomic % of oxygen manifesting the formation of MnO_2 on the electrode surface. The elemental mapping demonstrated uniform distribution of Mn, O, C and N over the scanned area confirming the efficient electro-functionalization of ITO with gCN.MnO_2.

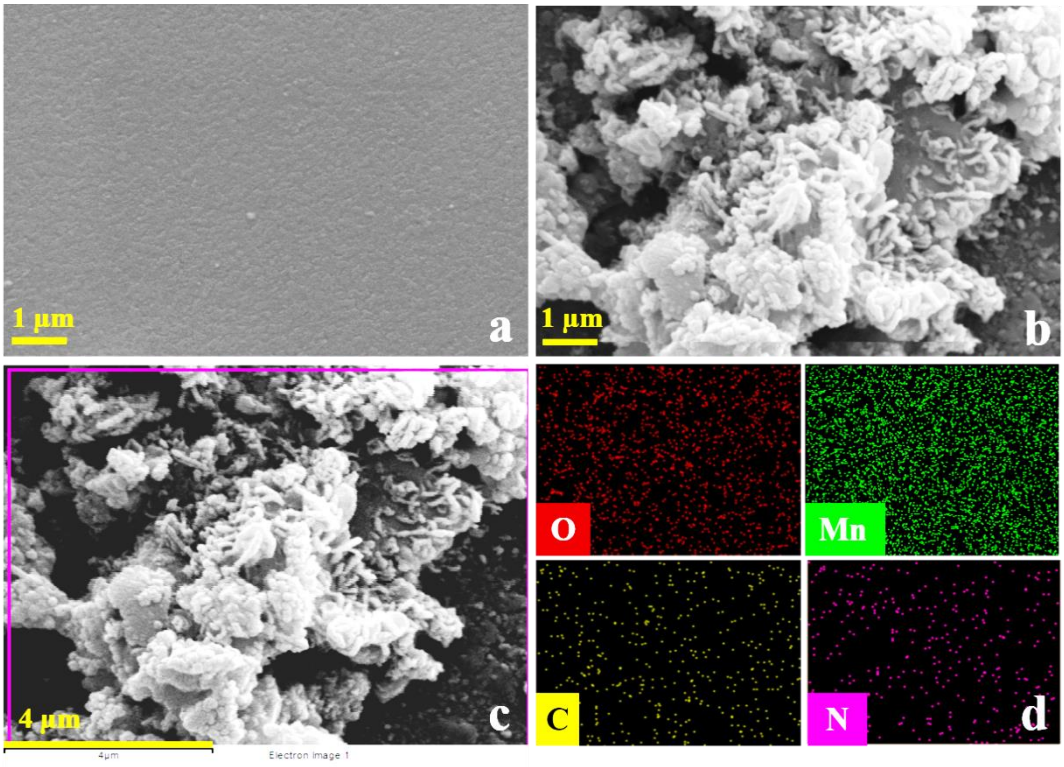

Figure 2.2.6: HR-SEM images of (a) Bare ITO at 1µm, (b) gCN.MnO_2 coated ITO at 1 µm, (c,d) The scanned area and corresponding elemental mapping of gCN.MnO_2|ITO.

After conducting a visualisation of the surface morphology using scanning electron microscopy (SEM), the modified ITO surface was characterised using XRD. **Figure 2.2.7(a)** illustrates the XRD spectra of both the blank and modified ITO samples. The ITO exhibited peaks at 21.6°, 30.0°, 35.0°, 50.4°, and 59.9°, corresponding to the crystallographic planes (211), (222), (400), (440), and (622) of indium and tin oxide coating[59]. In addition to ITO peaks, the XRD of gCN.MnO_2|ITO showcased five

additional peaks at angles of 26.6°, 38.2°, 44.5°, 64.7°, and 77.8°, labelled with *. These peaks are associated with (220), (211), (202), (002) and (402), crystallographic planes of MnO_2, respectively in agreement with JCPDS 44-0141 and JCPDS 44-0142[60–63]. The absence of gCN peak can be explained on the basis of its poor crystallinity. Thus, the XRD analysis offers supporting evidence to validate the claim that the proposed protocol resulted in the electrodeposition of a MnO_2 containing surface layer on the top of ITO.

X-ray photoelectron spectroscopy was next employed for carrying out a detailed compositional analysis of the electrodeposited layer. The full survey of the blank and coated ITO is depicted in **Figure 2.2.7(b)**. The presence of a surface layer on the top of ITO was evidenced by the observed reduction in the intensity of both indium (In) and tin (Sn) peaks in comparison to the blank ITO sample. The high-resolution deconvoluted XPS spectra of individual elements were further analysed for the comprehensive analysis of the surface layer. **Figure 2.2.7(c)** presents the Mn 2p spectrum showcasing two prominent peaks at 640.8 eV and 652.5 eV. These peaks correspond to the Mn $2p_{3/2}$ and Mn $2p_{1/2}$ of Mn_xO_y, respectively. The difference of 11.7 eV between the Mn $2p_{3/2}$ and Mn $2p_{1/2}$ indicates the presence of Mn^{4+} confirming the electrodeposition of MnO_2 containing surface layer[64]. The presence of MnO_2 was also hinted from the peak at 529.4 eV in O1s spectra (**Fig 2.2.7(d)**)[65]. The other two peaks at 530.94 and 532.2 eV corresponds to SnO_2 and In_2O_3 of the ITO, respectively.

The deconvoluted N 1s spectra (**Figure 2.2.7(e)**) displayed three different signals at binding energies of 397.6 eV, 398.8 eV and 400.2 eV, respectively. All the three signals were found to be associated with different chemical environment of N in the polymeric triazine structure of gCN. The N atoms that form sp^2 bonds with two carbon atoms (C=N-C) are responsible for the peak at 398.8 eV. The peak at 399.6 eV corresponds to N atoms trigonally bonded to three sp^2 carbon atoms in the C–N network (N-$(C)_3$). The presence

of N-H groups located at the open ends within the gCN network is accountable for the observed peak at 400.0 eV. Next, C 1s spectra (**Figure 2.2.7(f)**) was studied to validate the C-N bonding observed in N 1s as well as to confirm the presence of gCN in the surface layer. The peak at 285.7 eV indicates the presence of sp^2-bonded carbon (N-C=N) in the triazine units. Whereas, the peak at 287.9 eV was reported to arise from (N-$(C)_3$) indicating the presence of gCN[25,66,67]. The XPS data serves as further substantiation for the conclusions drawn from XRD and HR-SEM and manifests the successful electrodeposition of gCN.MnO_2 on the ITO surface layer.

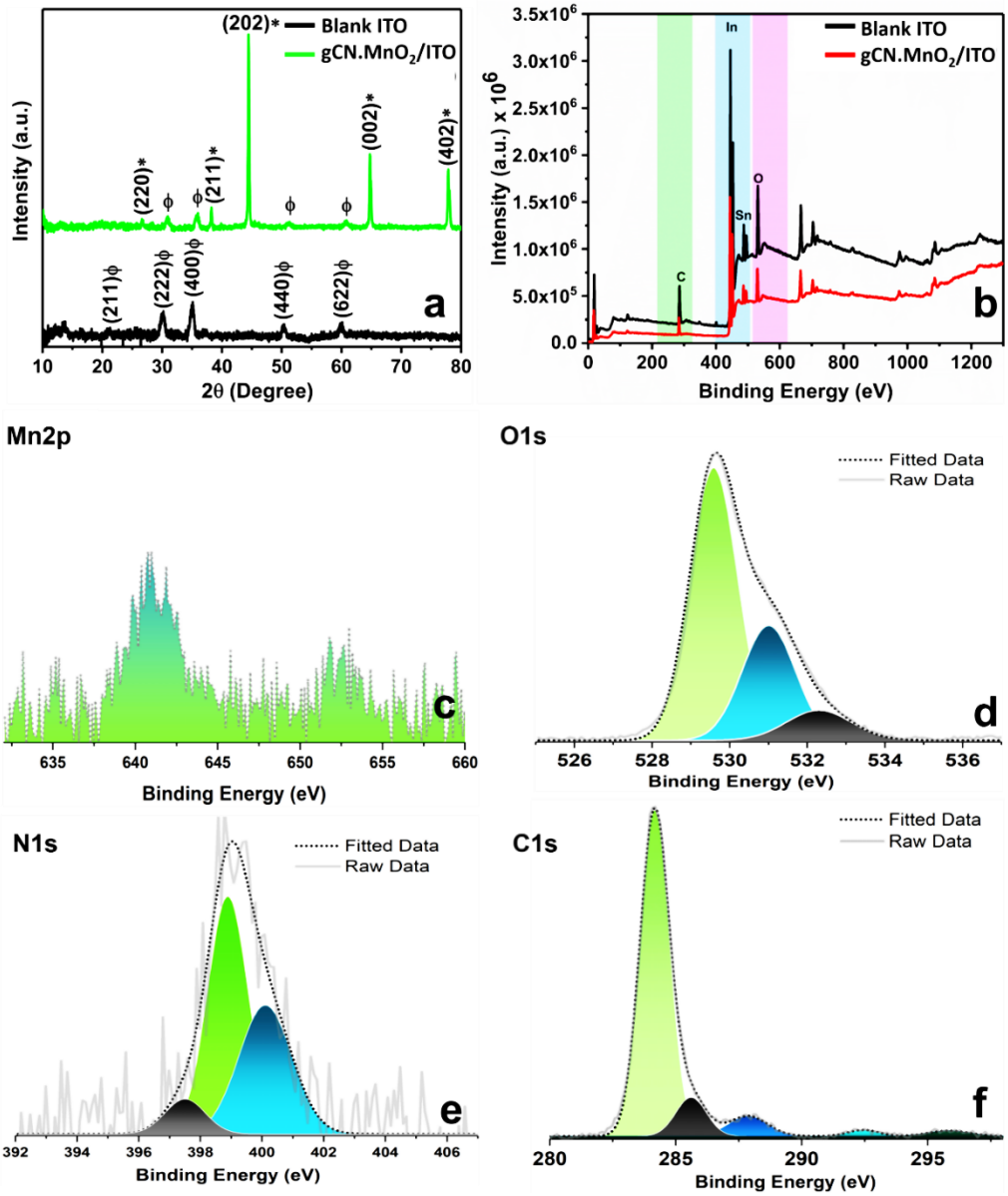

Figure 2.2.7: (a) X-ray diffraction patterns observed for ITO and gCN.MnO_2|ITO. XPS (b) Full survey, (c) Mn 2p, (d) O 1s, (e) N 1s and (f) C 1s spectra of gCN.MnO_2|ITO

Next, atomic force microscopy (AFM) was employed to investigate the changes in the surface roughness and thickness of the surface layer.

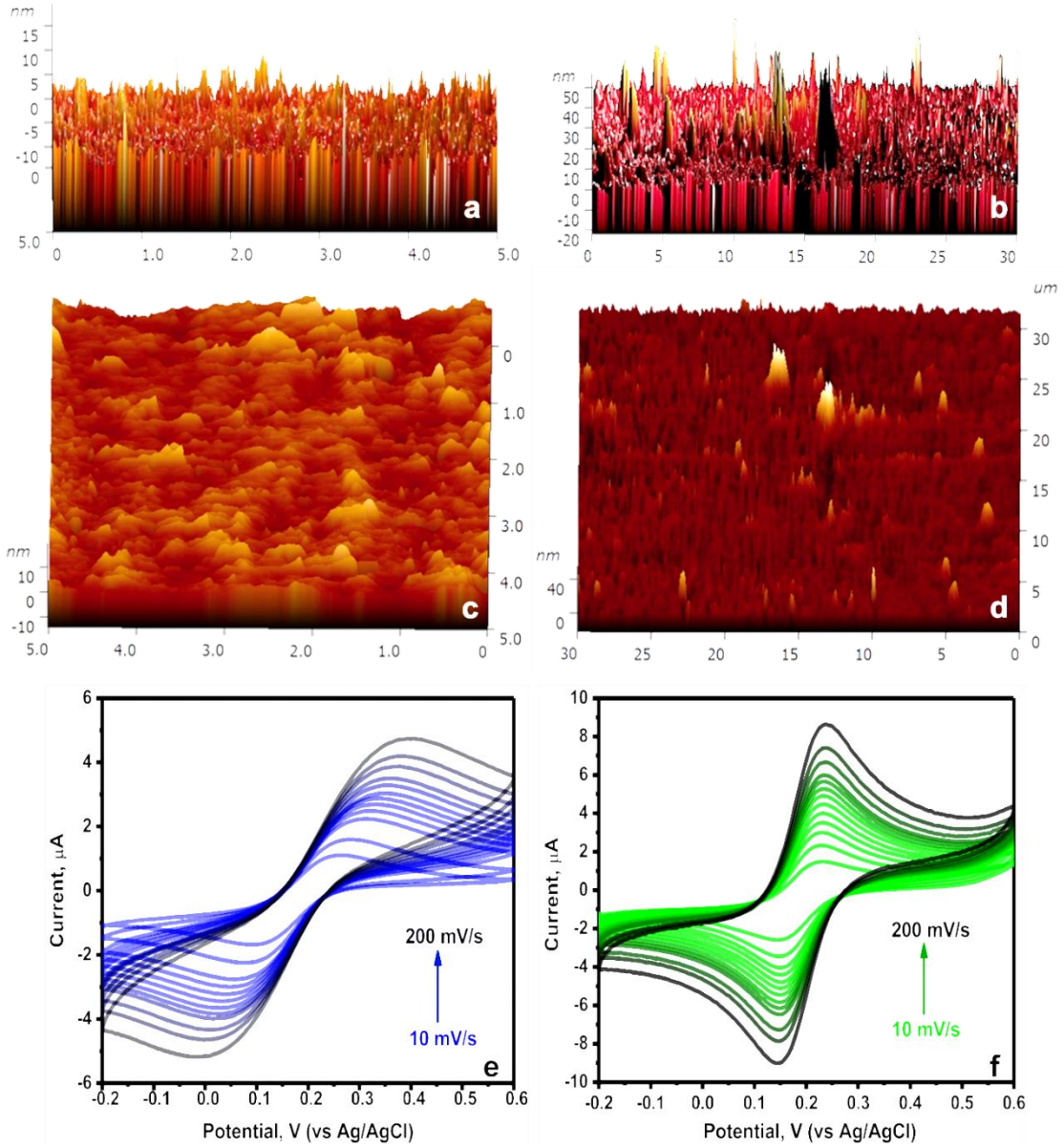

Figure 2.2.8: AFM 3D profiles observed for the (a, c) ITO and (b, d) gCN.MnO_2|ITO. Cyclic Voltammograms recorded at different scan rates ranging from 10 mV/s to 200 mV/s using (e) Bare, and (f) gCN.MnO_2|SPE in 0.5 mM $K_3[Fe(CN)_6]$ solution.

From the AFM peak profile analyses (**Figure 2.2.8(a-d)**), it is observed that the gCN.MnO_2|ITO composite exhibits a significantly greater average peak height of 35.11 nm, in contrast to the uncoated ITO peak height which measures only 5.44 nm. The root mean square roughness of the electrochemically tailored sample was also found to be >2

times higher compared to the uncoated sample. The observed increase in peak height and surface roughness confirms the electrodeposition on the ITO surface, with a layer thickness of approximately 30 nm. The increased roughness as manifested from AFM analysis hints towards increased surface area of the electro-functionalized substrate which is expected to be conducive for the electrochemical performance. After the comprehensive understanding of the electrodeposition protocol and its efficiency in improving the electrochemical performance and surface roughness of a conducting surface, it was applied to a practical sensing platform, i.e. the flexible screen-printed electrode (SPE). After electrochemical surface functionalisation of SPE, cyclic voltammetry (CV) technique was employed to assess the electrochemically active surface area of both the modified and unmodified electrode. To do so, $K_3[Fe(CN)_6]$ was used as an ideal redox couple having a known diffusion coefficient of 7.4 x 10^{-6} cm^2s^{-1}.[40] By monitoring the variation of peak current with the scan rate, the electrochemical surface area was calculated employing Randles Sevcik equation. **Figure 2.2.8(e,f)** illustrates the electrochemical redox processes of $K_3[Fe(CN)_6]$ recorded using both modified and unmodified screen-printed electrodes.

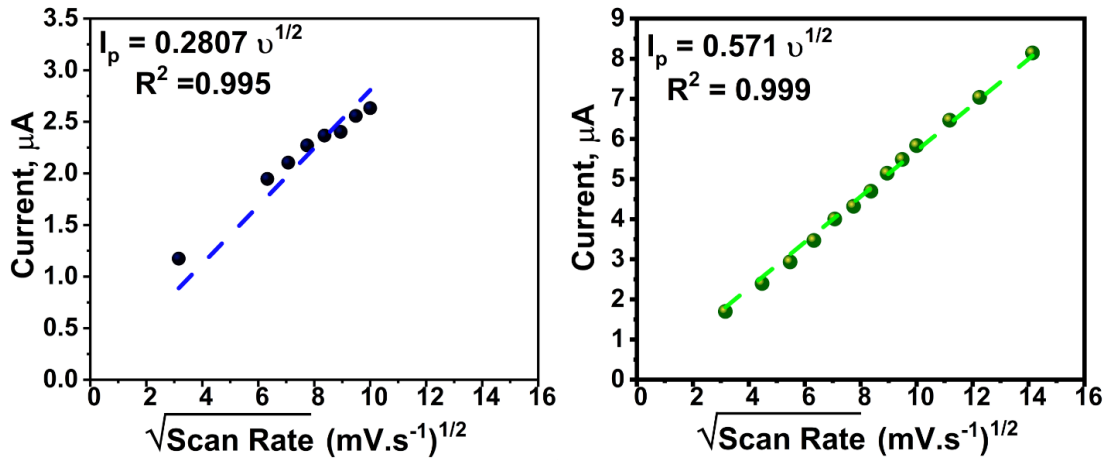

Figure 2.2.9: Linear regression plot of current vs (scan rate(υ))$^{1/2}$ for (a) bare SPE (b) gCN.MnO_2|SPE recorded for various scan rate in $K_3[Fe(CN)_6]$ solution.

Figure 2.2.9 presents the variation of peak current with the square root of the scan rate as observed for the bare and gCN.MnO_2|SPE, respectively. The Randles-Ševčík equation for the reversible process may be expressed as:

$$I_p = \pm 0.466\, n\, F\, A\, C\, \sqrt{\frac{nFD\upsilon}{RT}} \quad \text{.....[68]}$$

At 25° C, the Randles-Ševčík equation may be rewritten as:

$$I_p = \pm\ 2.69 \times 10^5\ n^{3/2}\ AD^{1/2}C\ \upsilon^{1/2} \quad \text{.....[69]}$$

As per the **:** Randles-Ševčík equation[69], the slope of I_p (μA) vs $\upsilon^{1/2}$ can be represented as

Slope = $2.69 \times 10^5\ n^{3/2}\ AD^{1/2}C$

Where, the variables I_p, n, A, D, C, and υ represent the peak current (A), number of electrons transferred, electro-active area (cm^2), diffusion coefficient of $[Fe(CN)_6]^{3-}$ in KCl solution ($cm^2\ s^{-1}$), probe molecule concentration (M), and scan rate ($V\ s^{-1}$), respectively. The active area of the bare electrode and the modified electrode were determined by calculating the slope of the I_p vs. $\upsilon^{1/2}$ linear plots. The active area of the bare electrode was found to be 0.0243 cm^2, while the modified electrode had an area of 0.0494 cm^2 which is ~ 2 times higher than bare SPE. As anticipated, due to its distinctive stoichiometry, and nanostructured morphology, the surface modification of SPE with gCN.MnO_2 composite results in a significantly increased number of potential sites for facilitated interfacial electron transfer.

The effect of gCN.MnO_2 electrodeposition on the electrochemical performance was then monitored by recording the comparative cyclic and square wave voltammograms using bare and gCN.MnO_2|SPE in 0.5 mM $K_3[Fe(CN)_6]$ solution. The CV shown in **Figure 2.2.10(a)** clearly shows a two-fold higher peak current for gCN.MnO_2|SPE compared to bare SPE. The substantially enhanced peak current attests the improved electrochemical performance of the gCN.MnO_2|SPE. Furthermore, a decreased peak to peak separation

and improved peak shape observed for gCN.MnO_2|SPE manifests the facilitated redox processes at the modified surface.

A clearer difference was observed from the square wave voltammetry (SWV) plots of the bare and modified SPE as presented in **Figure 2.2.10(b)**. The figure univocally illustrates the substantially improved electrochemical performance of the modified SPE showcasing a five times higher peak current compared to bare SPE. The five-fold enhancement in the current can partially be ascribed to the increased surface area as I_p is directly dependent on the electroactive surface area in accordance to the Randles-Ševčík equation. However, the synergistic interaction between MnO_2 and gCN are also expected to improve the charge transfer.

The comparative analysis of the electrochemical performance of bare, drop-casted and electrofunctionalized gCN.MnO_2|SPE is shown in **Figure 2.2.10(c)**. Substantially higher peak currents were observed for the electro-functionalization compared to the drop-casting methodology. This enhanced performance can be ascribed to conformal surface modification with a precise control on the thickness of the surface layer in case of electro-functionalization. On the other hand, drop casting is plagued by agglomeration, non-uniform material loading, human error, and poor interfacial contact[70,71]. Furthermore, the significant improvement after electrodeposition manifests that the electrochemical/chemical redox processes occurred during the course of electrodeposition of the composite material are crucial for witnessing the improved electrochemical performance.

2.2.3.3 Analytical performance of modified electrode: Sensing of Dopamine

The findings from the extensive chemical, structural and electrochemical investigation manifested the successful electro-functionalization of SPE with gCN.MnO_2 composite that leads to substantially improved electrochemical performance. The observed

enhancement can be ascribed to the increased electroactive surface area due to the nanostructured electrodeposited layer as well as the synergistic interaction between MnO_x and gCN. Both the structural and chemical alteration at the electrode interface results in aided electron transfer as well as electrocatalytic ability. Therefore, the superior traits of gCN.MnO_2|SPE were next employed for the selective and sensitive detection of DA, serving as a case study within a real-world context.

The voltammograms obtained for 100 µM DA using both unmodified and modified SPE are depicted in **Figure 2.2.10(d)**. The comparative analysis demonstrates that the gCN.MnO_2 electro-functionalization resulted in approximately 15 times higher current response compared to bare SPE. Furthermore, the bare SPE exhibited a peak at 0.16 V corresponding to the DA oxidation. Whereas, at modified electrode, the DA oxidation peak was found at 0.01 V. A negative potential shift of ~ 0.15 V attested the electro-catalytic ability of the modified scaffold towards DA oxidation. The significantly enhanced current and potential shift are synergistically dependent on the contribution of various factors like π-π interactions between the aromatic structures of the gCN and DA molecules, H-bonding, electrostatic interaction, enhanced surface area, and facilitated electron transfer at the MnO_2.gCN composite. All these interactions serve to bring the DA molecule in close proximity to the interface, thereby facilitating the charge transfer leading to the facilitated oxidation of dopamine to dopamine quinone (DQ)[41] at lower potentials.

In order to establish the reliability of the quantitative analysis, a calibration curve was constructed by investigating the influence of DA concentrations on the corresponding current responses. For both the bare and modified SPE electrodes, a linear increase in the peak current with the increasing DA concentration was observed. Interestingly, electrochemical response of DA concentration as low as 50 nM was observed using the

modified SPE. In contrast, the bare SPE was able to sense DA concentrations of 30 µM or higher.

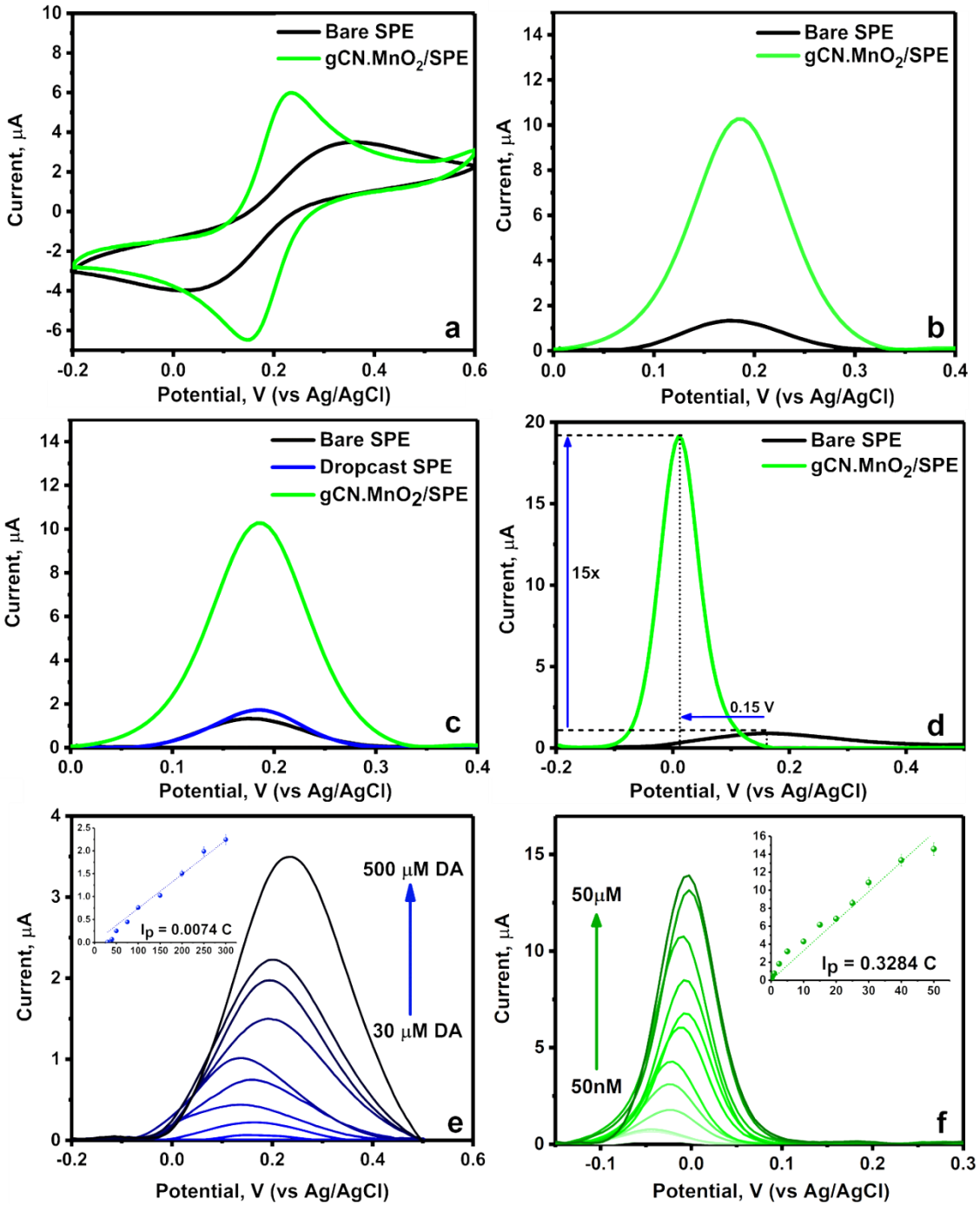

Figure 2.2.10: A comparative (a) Cyclic Voltammograms (b and c) Square Wave Voltammograms of 0.5 mM of $K_3[Fe(CN)_6]$ recorded using bare SPE, $gCN.MnO_2|SPE$ and SPE modified by drop-casting 10 µL of 7:3 $gCN.Mn_xO_y$ suspension. (d) Square Wave Voltammograms of 100 µM of DA observed in PB 7.4 buffer at bare SPE and $gCN.MnO_2$ coated SPE. SWV observed using (e) bare SPE at different concentrations ranging from 30 µM to 500 µM and (f) using modified SPE at different concentrations ranging from 50 nM to 50 µM.

The increase in the peak current with increaing DA concentration is illustrated in **Figure 2.2.10(e,f)**.

The following regression equations were formulated by analysing the relationship between the peak current (I_p) and DA concentration (C):

$\boldsymbol{I_p}$ (μA) = 0.3284 **C** [0.05-50 µM] ; R^2 = 0.984……..**:** gCN.MnO_2|SPE

$\boldsymbol{I_p}$ (μA) = 0.0074 **C** [30-300 µM] ; R^2 = 0.988……..**:** SPE

The slope of the regression equation represents the sensitivity of the developed sensor towards the particular analyte. Comparing the observed values, the gCN.MnO_2 modified electrode was found to be 44 times more sensitive than the unmodified SPE electrode. In addition, limit of detection (LOD) was calculated using the formula 3σ/b, where 'σ' denotes the standard deviation of five blank measurements and 'b' represents the slope of the regression equation[72]. The experimental findings suggest that the gCN.MnO_2 composite exhibited a significantly lower limit of detection (LOD) of 10 nM, indicating its superior sensitivity in detecting DA. In contrast, the bare SPE had a LOD of 5.36 µM. To have a better idea about the superiority of the developed sensor, its performance was compared with some of the previously documented DA electrochemical sensors that utilised gCN and similar surface modifiers. As seen from **Table 2.2.1**, the developed sensor exhibited better traits in terms of ease of fabrication and sensitivity. Furthermore, all of the methodologies reported in the literature involve the individual synthesis of constituent materials, followed by the subsequent process of mixing and drop-casting the prepared material. On the other hand, the proposed protocol presents the ability to carry out electrodeposition in a single step with a precise control on the layer thickness, thereby enhancing its reproducibility, practicality and scalability.

Table 2.2.1: Comparison of the reported electrochemical sensors developed for DA estimation using gCN, metal oxides, and similar surface modifications with the proposed gCN.MnO_2|SPE scaffold.

Electrode Material	***Technique***	***Linear range (µM)***	***LOD (µM)***	***Modification method***	***Ref.***
GGQDs/IL-SPCE	DPV	0.2-15	0.06	Multistep Synthesis + Drop cast	[73]
PCN/GO/GCE	DPV	0.25-40	0.07	Multistep Synthesis + Drop cast	[74]
Fe_3C@NGCSs/GCE	DPV	3-104	0.075	Multistep Synthesis + Drop cast	[75]
GNP/CNT-SPE	DPV	0.4-40	0.4	Multistep Synthesis + Drop cast	[76]
Pd@α-MnO_2/G	DPV	0.2-425	0.086	Multistep Synthesis + Drop cast	[77]
ZnO-rGO-AuNPs@SPE	DPV	0.5-100	0.294	Multistep Synthesis + Drop cast	[78]
NanoDiaSens	SWV	0-100	0.068	Complex step procedure	[79]
N-GDY/GCE	i-t	1-550	0.46	Multistep Synthesis + Drop cast	[80]
D-PdMo/GCE	DPV	0.05-100	0.029	Multistep Synthesis + Drop cast	[81]
$AgBiS_2$/PEDOT:PSS/GCE	Amperometry	0.08–937.5	0.0026	Multistep Synthesis + Drop cast	[82]
gCN.MnO_2/ITO (Our Recent Work)	SWV	5-500	0.02	Two component electrodeposition	[27]
gCN.MnO_2|SPE	SWV	0.05-50	0.01	Single step electrodeposition	This work

Although increased surface area and functionality are helpful for electron transfer, they can also make surfaces more porous and encourage surface adsorption, which can lead to undesirable capacitive current and surface fouling. A frequency study was used to investigate the impact of surface modification on the mass-transfer mechanism involved in the oxidation of DA. When the frequency was changed from 5 to 100 Hz, square wave

voltammograms of 100 µM DA in a pH 7.4 buffer solution were recorded. The frequency and the observed change in peak current were shown to be correlated using following linear regression equations (**Figure 2.2.11**):

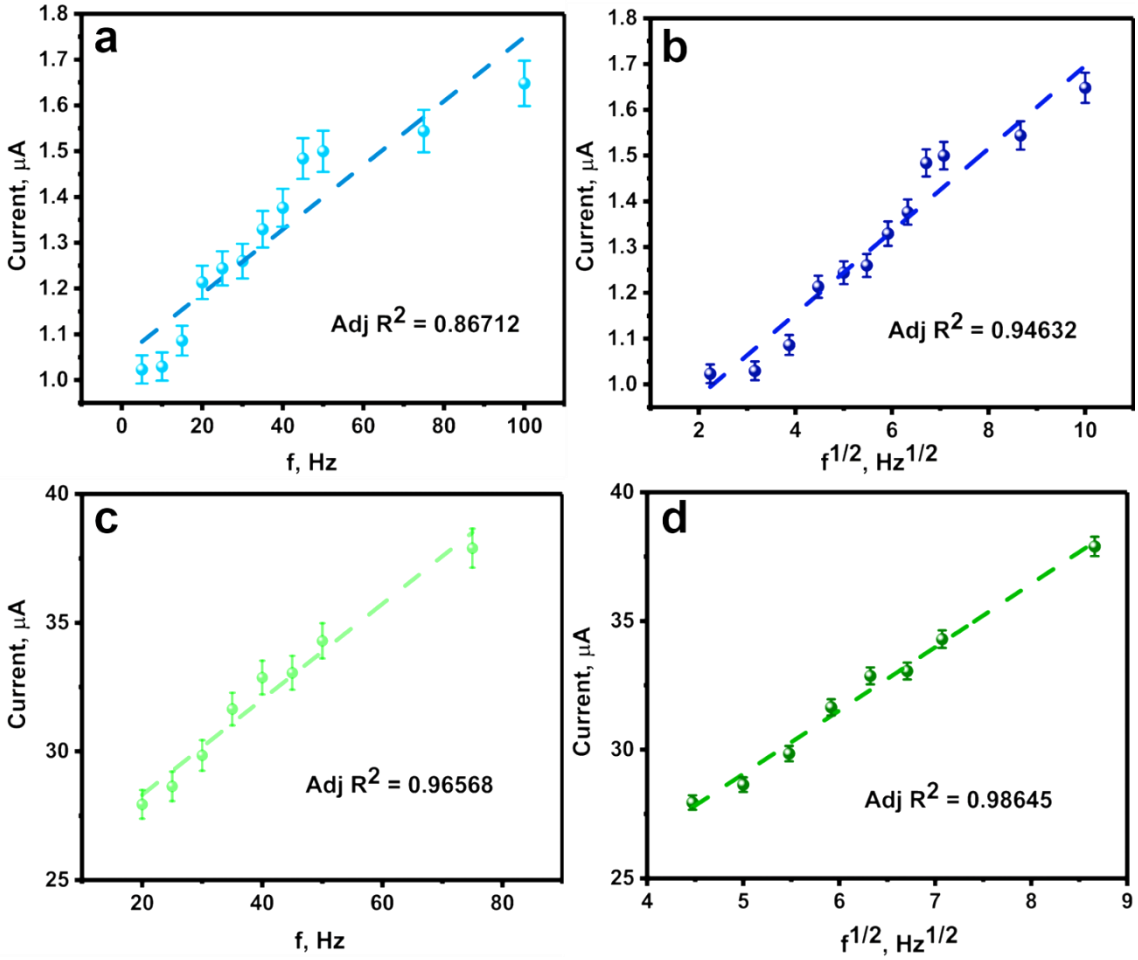

Figure 2.2.11: Linear regression plot of current vs f and current vs $f^{1/2}$ for (a) bare SPE (b) gCN.MnO_2|SPE recorded using 100 µM DA in a pH 7.4 buffer solution.

I_p (μA) = 0.007 f [5-100 Hz] + 1.048 R^2 = 0.867 ……...**:** SPE

I_p (μA) = 0.090 $f^{½}$ [5-100 Hz] + 0.792 R^2 = 0.946 ……..**:** SPE

I_p (μA) = 0.185 f [20-75 Hz] + 24.609 R^2 = 0.965 ……**:** gCN.MnO_2|SPE

I_p (μA) = 2.463 $f^{½}$ [20-75 Hz] + 16.744 R^2 = 0.986 ……..**:** gCN.MnO_2|SPE

Both the scaffolds that were modified and unmodified exhibit a linear variation of **Ip** vs. ($f^{½}$) that is more pronounced when compared to I_p vs. f. The linear relationship between the current (I_p) and the square root of the frequency ($f^{½}$), in accordance with the Randles

Sevcik equation, suggests the occurrence of diffusion controlled mass transfer[83], without any additional complexities arising from adsorption. Thus, the present research eliminates any adverse effects linked to the increased electroactive region and supplementary surface functionalities of the gCN.MnO_2|SPE. The aforementioned findings demonstrate the distinctive capability of the modified SPE surface to qualitatively and quantitatively evaluate the low concentration of DA.

In addition to sensitivity, a discerning analysis is necessary to fully grasp the practical implications of the proposed sensor to quantitatively assay, DA in presence of other influencing species. Therefore, the efficacy of the developed sensor to assay DA in presence of other potential interfering compounds commonly present in blood plasma, and urine was investigated. Four interferants, namely uric acid (UA), ascorbic acid (AA), melatonin (MEL), and tryptophan (TRP), were first used, and their influence on the peak current of 20 µM DA was monitored. **Figure 2.2.12(a)** depicts the SWV plot recorded for 20 µM DA in the presence of increasing concentrations of all four interferants. The SWV demonstrates that the current response of DA did not exhibit any significant deviation in the presence of 3 fold higher concentrations of interferants. Nevertheless, only a slight decline in the DA peak current was observed in the presence of 80 µM each of AA, UA, MEL, and TRP. No significant deviation in the peak current further confirms the interference-free estimation of DA. Therefore, building on the results, it can be univocally inferred that the gCN.MnO_2|SPE exhibits high efficacy in accurately quantifying DA, even in the complex matrix.

2.2.3.4 Real Sample Study

To ensure the real world application, the developed sensor was tested for estimation of DA in pharmaceutical samples, food product, and human biological fluids.

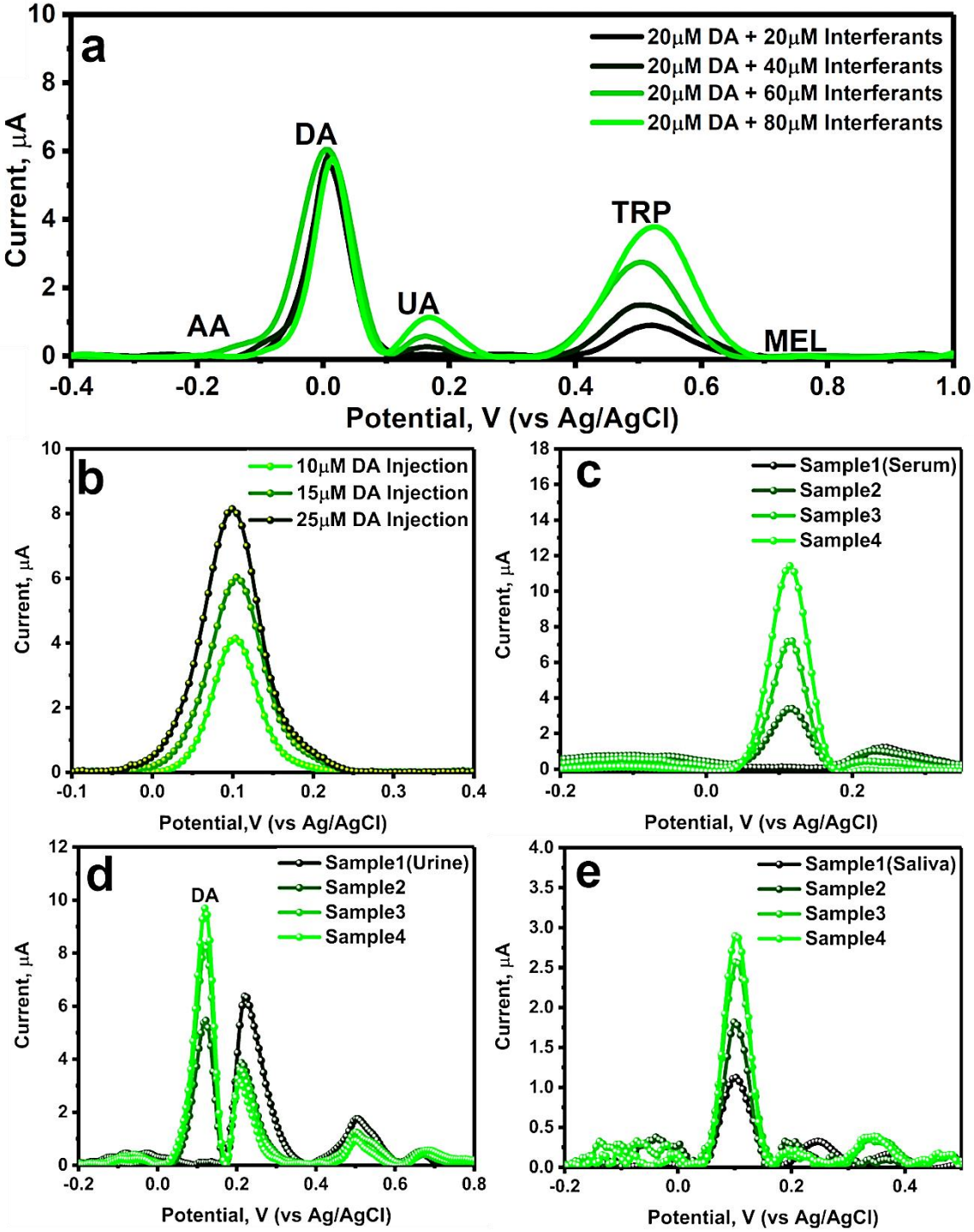

Figure 2.2.12: (a) Interference Study: Square wave voltammogram representing the variation in the DA (20 μM) peak currents recorded in presence of different concentration of Ascorbic Acid (AA), Uric Acid (UA), Tryptophan (TRP) and Melatonin (MEL) using gCN.MnO_2|SPE. (b-e) Real sample analysis: square wave voltammograms representing the presence of DA in (b) commercial DA hydrochloride injection, (c) human blood serum, (d) urine, and (e) human saliva.

DA hydrochloride injections is a commonly used pharmaceutical formulations for overcoming hemodynamic imbalances resulting from shock during/after surgeries. The

dosage of the injection is critical for the patients' health. Therefore, the developed sensor was used to validate DA content in the commercial sample. To do so a stock solution was prepared using the reported content of the DA on the injection specifications. Using the prepared solution, test solutions were prepared corresponding to 10 µM, 15 µM, and 25 µM DA concentrations. **Figure 2.2.12(b)** illustrates the SWV showcasing a peak at ~ 0.1 V arising because of DA. With the increasing DA concentration, the peak current was found to increase confirming its association with DA. The observed and used current were compared to calculate the deviations. The results are tabulated in **Table 2.2.2**.

Also, the first peak was found to increase with the increasing volume of banana peel further attesting its origin from the oxidation of DA. The observed peak currents were than used to find out the amount of DA in the banana peel and the results are tabulated in **Table 2.2.2**.

Next, the clinical application of the developed sensor was tested by carrying out DA estimation in complex human fluids like serum, urine, and saliva. The serum sample of healthy volunteer was collected and used for further analysis. The voltammetric analysis was performed by using PB 7 as the supporting electrolyte. As presented in **Figure 2.2.12(c)**, DA was not detected in the serum sample. Therefore, standard addition method was employed and three sample was made with by spiking different volumes of DA stock solution. A clear peak at 0.114 V was observed after mixing the serum with 10 µM DA solution. The peak was found to increase with increasing

DA concentration that was spiked externally. The observed current was then used to back calculate the DA levels using the calibration plot and the results are tabulated in **Table 2.2.2**. The results are found in good agreement with the spiked values confirming the applicability of developed sensor in monitoring DA levels in the serum sample.

Table 2.2.2: Quantification of DA in real samples using gCN.MnO_2|SPE.

Sample	Current (μA)	Detected (μM)	Actual (μM)	Error (%)
DA hydrochloride injection				
10 μM	4.15	10.81	10	8.10
15 μM	5.85	15.98	15	6.53
25 μM	8.19	23.11	25	7.56
Sample	Current (μA)	Spiked (μM)	Detected (μM)	Error (%)
Human Serum				
1	ND	0	0	-
2	3.59	10	9.12	8.80
3	7.33	20	20.47	2.35
4	11.26	30	32.46	8.20
Human Urine				
1	ND	0	0	-
2	5.46	15	14.81	1.26
3	8.37	25	23.66	5.36
4	9.78	30	27.94	6.87
Human Saliva				
1	1.14	0	1.66	-
2	1.83	0.5	2.10	2.77
3	2.57	2.5	4.35	4.56
4	2.91	4	5.38	4.94

The actual DA content in human serum, urine and saliva sample were validated from UV-Vis spectroscopy.

The elevated level of urinary dopamine levels is found to be associated with drug effects/overdoze or clinical reasons like tumours, phaeochromocytoma or pregnancy. Thus, the estimation of DA in urine samples is of great significance for medical reasons. Therefore, the DA analysis was next carried out in the urine sample of a healthy volunteer. Initially, the sample was filtered and diluted 5-fold with DI. Subsequently, a specific volume of the urine sample was promptly injected into the PB 7 electrolyte. The obtained solutions were subsequently examined utilising SWV. **Figure 2.2.12(d)** demonstrated the presence of uric acid and other metabolites but no peak corresponding to DA was observed. Thus, 15, 25 and 30 μM of DA was used and the SWV was recorded,

respectively. The peak at 0.11 V corresponding to DA oxidation was observed in sample which was found to increase with the increasing DA levels. The concentration of DA was then back calculated using the observed current and the results are shown in **Table 2.2.2**. The different concentration levels are in well agreement with the calculated DA concentrations manifesting the efficacy of developed sensor to monitor changes in DA level in complex matrix and in presence of several other electrochemically active biological metabolites.

Dopamine levels in saliva is considered as a potential biomarker for the early detection of neurodegenerative diseases in humans. So, here, the developed sensor was also tested for estimating the DA concentration in saliva of a healthy human volunteer. We directly injected 100 µL of saliva sample into 100 µL of PB 7 electrolyte, and 50 µL of it was dropped on the SPE for further SWV analysis. Interestingly, the presence of DA was manifested by the peak at 0.11 V in the saliva sample. To confirm that peak corresponds to DA and not any other salivary catecholamine, the three saliva sample was made with different DA stock solution. As seen from the **Figure 2.2.12(e)** the same peak was found to increase with increasing DA levels confirming its origin from the salivary DA oxidation. To quantify the salivary DA levels, the observed current was put in the linear regression equation obtained from the calibration plot. The obtained results are tabulated in **Table 2.2.2** demonstrating an error percentage of < 1-9 % indicating the wide applicability of the developed sensor in clinical analysis.

2.2.3.5 Reliability Studies

The long term durability of the gCN.MnO_2|SPE was tested by recording repeated cyclic voltammograms in a buffer solution having a pH of 7.4. The observed voltammograms shown in **Figure 2.2.13(a)** reveals that the gCN.MnO_2 scaffolds retained a significant amount of their initial durability even after being subjected to a total of 100 CV cycles.

The constant blank voltammograms provide evidence that the changed surface will maintain its long-term stability even after being subjected to repeated use. **Figure 2.2.13(b,c)** presents the first fifty SWV and the corresponding peak currents of $K_3[Fe(CN)_6]$ recorded using the single gCN.MnO_2 modified SPE. As illustrated from the bar diagram, even being a single use disposable electrode, the modified SPE demonstrated appreciable stability showcasing a drop of only 6 % of initial peak current.

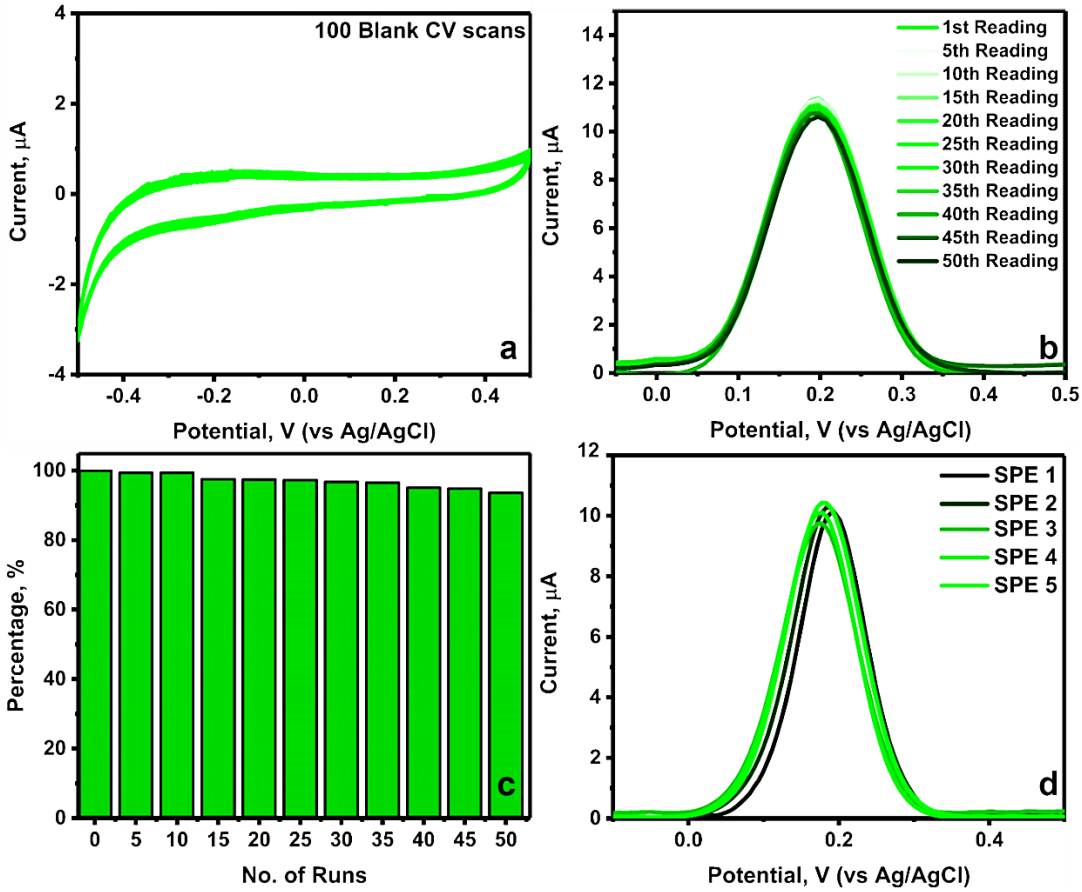

Figure 2.2.13: (a) 100 consecutive cyclic voltammograms recorded in Phosphate Buffer (PB 7.4) using gCN.MnO_2|SPE. (b) First fifty square wave voltammograms and (c) respective variation in current percentages as observed for 0.5 mM $K_3[Fe(CN)_6]$ using single gCN.MnO_2|SPE. (d) Square wave voltammograms recorded for 0.5 mM $K_3[Fe(CN)_6]$ using 5 different gCN.MnO_2|SPE.

The reproducibility of the proposed protocol was also tested by modifying five different SPE's. The SWV in $K_3[Fe(CN)_6]$ was recorded and compared using multiple SPE electrodes modified using the same protocol. As witnessed from **Figure 2.2.13(d**), all the SPE's showcased concurrent peak currents featuring excellent reproducibility of the

proposed protocol for surface modification of large number of SPEs. Both the studies confirmed the extensive stability and reproducibility of the modified electrode signifying the applicability of the proposed protocol for commercial applications.

2.2.4. Conclusions

The current study looks into the synthesis, characterization, and use of gCN.Mn_xO_y composites for improving the sensing performance of commercial SPE. The proposed methodology investigates and compares the electro-functionalization mechanisms of 9:1 and 7:3 gCN.Mn_xO_y, as well as their impact on the electrochemical performance of the conducting substrate. The structural, compositional, and electrochemical characterization evinced the surface changes and electrodeposition of gCN.MnO_2 on the conducting substrate. Out of all the tested surface modifiers, the gCN.MnO_2|SPE fabricated using 7:3 gCN.Mn_xO_y composite exhibits the best electrochemical performance. With a 15 fold higher current and a 0.15 V negative potential shift, the gCN.MnO_2|SPE demonstrated 44 times more sensitivity than bare SPE and facilitated dopamine oxidation at the tailored interface. As a result of this, the gCN.MnO_2 modified electrode manifests a LOD of 10 nM, compared to 5.36 µM of the unmodified SPE. The substantial improvement can be attributed to the synergistic combination of π-conjugated network of gCN and the facilitated redox processes offered by the MnO_2 resulting in, augmented catalytically active sites, ~2-times higher electroactive surface area and π-π interaction between DA and the tailored interface. The developed sensor's accuracy was demonstrated by measuring the DA content of pharmaceutical DA hydrochloride injection, and, three spiked clinical samples namely, urine, saliva and blood serum. The electrodeposition protocol's practicability was also aided by the gCN.MnO_2|SPE's stability, repeatability, and reproducibility.

2.2.5. References:

[1] G. Paimard, E. Ghasali, M. Baeza, Screen-Printed Electrodes: Fabrication, Modification, and Biosensing Applications, Chemosensors. 11 (2023) 113. https://doi.org/10.3390/chemosensors11020113.

[2] M.A. Alonso-Lomillo, O. Domínguez-Renedo, M.J. Arcos-Martínez, Screen-printed biosensors in microbiology; A review, Talanta. 82 (2010) 1629–1636. https://doi.org/10.1016/j.talanta.2010.08.033.

[3] J. Barton, M.B.G. García, D.H. Santos, P. Fanjul-Bolado, A. Ribotti, M. McCaul, D. Diamond, P. Magni, Screen-printed electrodes for environmental monitoring of heavy metal ions: a review, Microchim. Acta. 183 (2016) 503–517. https://doi.org/10.1007/s00604-015-1651-0.

[4] M. Li, D.W. Li, G. Xiu, Y.T. Long, Applications of screen-printed electrodes in current environmental analysis, Curr. Opin. Electrochem. 3 (2017) 137–143. https://doi.org/10.1016/j.coelec.2017.08.016.

[5] F. Arduini, L. Micheli, D. Moscone, G. Palleschi, S. Piermarini, F. Ricci, G. Volpe, Electrochemical biosensors based on nanomodified screen-printed electrodes: Recent applications in clinical analysis, TrAC - Trends Anal. Chem. 79 (2016) 114–126. https://doi.org/10.1016/j.trac.2016.01.032.

[6] A. Smart, A. Crew, R. Pemberton, G. Hughes, O. Doran, J.P. Hart, Screen-printed carbon based biosensors and their applications in agri-food safety, TrAC - Trends Anal. Chem. 127 (2020) 115898. https://doi.org/10.1016/j.trac.2020.115898.

[7] A. García-Miranda Ferrari, S.J. Rowley-Neale, C.E. Banks, Screen-printed electrodes: Transitioning the laboratory in-to-the field, Talanta Open. 3 (2021) 100032. https://doi.org/10.1016/J.TALO.2021.100032.

[8] A. García-Miranda Ferrari, S.J. Rowley-Neale, C.E. Banks, Screen-printed

electrodes: Transitioning the laboratory in-to-the field, Talanta Open. 3 (2021) 100032. https://doi.org/10.1016/j.talo.2021.100032.

[9] S. Cinti, F. Arduini, Graphene-based screen-printed electrochemical (bio)sensors and their applications: Efforts and criticisms, Biosens. Bioelectron. 89 (2017) 107–122. https://doi.org/10.1016/j.bios.2016.07.005.

[10] S. Garg, A. Singh, A.S. Parmar, N. Rosy, Boron Carbon Nitride-Assisted Electro-Functionalization of Screen-Printed Electrode for Tryptophan Sensing, ACS Appl. Nano Mater. 7 (2023) 2023. https://doi.org/10.1021/acsanm.3c02396.

[11] S. Su, Q. Sun, X. Gu, Y. Xu, J. Shen, D. Zhu, J. Chao, C. Fan, L. Wang, Two-dimensional nanomaterials for biosensing applications, TrAC - Trends Anal. Chem. 119 (2019) 115610. https://doi.org/10.1016/j.trac.2019.07.021.

[12] P.K. Kalambate, P. Thirabowonkitphithan, P. Kaewarsa, K. Permpoka, A.B. Radwan, R.A. Shakoor, R.P. Kalambate, H. Khosropour, Y. Huang, W. Laiwattanapaisal, Progress, challenges, and opportunities of two-dimensional layered materials based electrochemical sensors and biosensors, Mater. Today Chem. 26 (2022) 101235. https://doi.org/10.1016/j.mtchem.2022.101235.

[13] R. Umapathi, C. Venkateswara Raju, S. Majid Ghoreishian, G. Mohana Rani, K. Kumar, M.H. Oh, J. Pil Park, Y. Suk Huh, Recent advances in the use of graphitic carbon nitride-based composites for the electrochemical detection of hazardous contaminants, Coord. Chem. Rev. 470 (2022) 214708. https://doi.org/10.1016/j.ccr.2022.214708.

[14] A.K. Mrinalini Kalyani, R. Rajeev, L. Benny, A.R. Cherian, A. Varghese, Surface tuning of nanostructured graphitic carbon nitrides for enhanced electrocatalytic applications: a review, Mater. Today Chem. 30 (2023) 101523. https://doi.org/10.1016/j.mtchem.2023.101523.

[15] J. Lv, C. Li, S. Feng, S.M. Chen, Y. Ding, C. Chen, Q. Hao, T.H. Yang, W. Lei, A novel electrochemical sensor for uric acid detection based on PCN/MWCNT, Ionics (Kiel). 25 (2019) 4437–4445. https://doi.org/10.1007/s11581-019-03010-8.

[16] T. Ahmad, S. Khan, T. Rasheed, N. Ullah, Graphitic carbon nitride nanosheets as promising candidates for the detection of hazardous contaminants of environmental and biological concern in aqueous matrices, Microchim. Acta. 189 (2022) 1–28. https://doi.org/10.1007/s00604-022-05516-x.

[17] T. Fidan, M. Torabfam, Q. Saleem, C. Wang, H. Kurt, M. Yüce, J. Tang, M.K. Bayazit, Functionalized Graphitic Carbon Nitrides for Environmental and Sensing Applications, Adv. Energy Sustain. Res. 2 (2021) 2000073. https://doi.org/10.1002/aesr.202000073.

[18] Q.Z. Zhang, D. Zhang, Z.C. Miao, X.L. Zhang, S.L. Chou, Research Progress in MnO2–Carbon Based Supercapacitor Electrode Materials, Small. 14 (2018) 1702883. https://doi.org/10.1002/smll.201702883.

[19] R. Yang, Y. Fan, R. Ye, Y. Tang, X. Cao, Z. Yin, Z. Zeng, MnO2-Based Materials for Environmental Applications, Adv. Mater. 33 (2021) 1–53. https://doi.org/10.1002/adma.202004862.

[20] M. Diantoro, I. Istiqomah, Y. Al Fath, N. Nasikhudin, Y. Alias, W. Meevasana, Potential of MnO2-based composite and numerous morphological for enhancing supercapacitors performance, Int. J. Appl. Ceram. Technol. 20 (2023) 2077–2098. https://doi.org/10.1111/ijac.14377.

[21] Y.H. Bai, J.J. Xu, H.Y. Chen, Selective sensing of cysteine on manganese dioxide nanowires and chitosan modified glassy carbon electrodes, Biosens. Bioelectron. 24 (2009) 2985–2990. https://doi.org/10.1016/J.BIOS.2009.03.008.

[22] N. Jaiswal, I. Tiwari, C.W. Foster, C.E. Banks, Highly sensitive amperometric

sensing of nitrite utilizing bulk-modified MnO2 decorated Graphene oxide nanocomposite screen-printed electrodes, Electrochim. Acta. 227 (2017) 255–266. https://doi.org/10.1016/J.ELECTACTA.2017.01.007.

[23] Z. Yong, C. Cui-rong, W. Shi-wen, G. Hai-li, Y. Ji, J. Xiao-dong, L. He-wei, G. Ke-zheng, Z. Ai-qin, Z. Yong, C. Cui-rong, W. Shi-wen, G. Hai-li, Y. Ji, J. Xiao-dong, L. He-wei, G. Ke-zheng, Z. Ai-qin, Preparation and supercapacitive performance of pinecone-like $NiMoO_4/MnO_2$ composite material, Chinese J. Eng. 2019, Vol. 41, Issue 5, Pages 646-651. 41 (2019) 646–651. https://doi.org/10.13374/J.ISSN2095-9389.2019.05.011.

[24] Z. Long-fei, Q. Hong-mei, X. Mei, L. Yan-zhen, H. Jian-ling, W. Zi-ya, W. Feng-ping, Z. Long-fei, Q. Hong-mei, X. Mei, L. Yan-zhen, H. Jian-ling, W. Zi-ya, W. Feng-ping, Synthesis and electrochemical properties of graphene/MnO_2 composites, Chinese J. Eng. 2016, Vol. 38, Issue 9, Pages 1300-1305. 38 (2016) 1300–1305. https://doi.org/10.13374/J.ISSN2095-9389.2016.09.015.

[25] G. Elmacı, A.S. Ertürk, M. Sevim, Ö. Metin, MnO2 nanowires anchored on mesoporous graphitic carbon nitride (MnO2@mpg-C3N4) as a highly efficient electrocatalyst for the oxygen evolution reaction, Int. J. Hydrogen Energy. 44 (2019) 17995–18006. https://doi.org/10.1016/j.ijhydene.2019.05.089.

[26] M. Keerthi, S. Manavalan, S.-M. Chen, P.-W. Shen, A Facile Hydrothermal Synthesis and Electrochemical Properties of Manganese dioxide@graphitic Carbon Nitride Nanocomposite toward Highly Sensitive Detection of Nitrite, J. Electrochem. Soc. 166 (2019) B1245–B1250. https://doi.org/10.1149/2.0251914jes.

[27] A.K. Singh, P. Keshari, A. Saroj, V. Ramanathan, Rosy, Electrodeposition of Graphitic Carbon Nitride and its In situ Decoration with MnO2 Nanostructures: A

Tailored Interface for Dopamine Sensing, Surfaces and Interfaces. 42 (2023) 103316. https://doi.org/10.1016/j.surfin.2023.103316.

[28] R.A. Wise, M.A. Robble, Dopamine and addiction, Annu. Rev. Psychol. 71 (2020) 79–106. https://doi.org/10.1146/annurev-psych-010418-103337.

[29] X. Lin, Y. Zhang, W. Chen, P. Wu, Electrocatalytic oxidation and determination of dopamine in the presence of ascorbic acid and uric acid at a poly (p-nitrobenzenazo resorcinol) modified glassy carbon electrode, Sensors Actuators, B Chem. 122 (2007) 309–314. https://doi.org/10.1016/j.snb.2006.06.004.

[30] X. Liu, J. Liu, Biosensors and sensors for dopamine detection, VIEW. 2 (2021) 20200102. https://doi.org/10.1002/VIW.20200102.

[31] Irkham, K. Nasa, I. Kurnia, Y.W. Hartati, Y. Einaga, Low-interference norepinephrine signal on dopamine detection using nafion-coated boron doped diamond electrodes, Biosens. Bioelectron. 220 (2023) 114892. https://doi.org/10.1016/j.bios.2022.114892.

[32] T.C. Napier, A. Kirby, A.L. Persons, The role of dopamine pharmacotherapy and addiction-like behaviors in Parkinson's disease, Prog. Neuro-Psychopharmacology Biol. Psychiatry. 102 (2020) 109942. https://doi.org/10.1016/j.pnpbp.2020.109942.

[33] X. Pan, A.C. Kaminga, S.W. Wen, X. Wu, K. Acheampong, A. Liu, Dopamine and dopamine receptors in Alzheimer's disease: A systematic review and network meta-analysis, Front. Aging Neurosci. 10 (2019) 450684. https://doi.org/10.3389/fnagi.2019.00175.

[34] P.J. Gaskill, T.M. Calderon, A.J. Luers, E.A. Eugenin, J.A. Javitch, J.W. Berman, Human immunodeficiency virus (HIV) infection of human macrophages is increased by dopamine: A bridge between HIV-associated neurologic disorders

and drug abuse, Am. J. Pathol. 175 (2009) 1148–1159. https://doi.org/10.2353/ajpath.2009.081067.

[35] W.A. Hening, R.P. Allen, C.J. Earley, D.L. Picchietti, M.H. Silber, An update on the dopaminergic treatment of restless legs syndrome and periodic limb movement disorder, Sleep. 27 (2004) 560–583. https://doi.org/10.1093/sleep/27.3.560.

[36] M. Gill, G. Daly, S. Heron, Z. Hawi, M. Fitzgerald, Confirmation of association between attention deficit hyperactivity disorder and a dopamine transporter polymorphism, Mol. Psychiatry 1997 24. 2 (1997) 311–313. https://doi.org/10.1038/sj.mp.4000290.

[37] S.A. Buck, M. Quincy Erickson-Oberg, R.W. Logan, Z. Freyberg, Relevance of interactions between dopamine and glutamate neurotransmission in schizophrenia, Mol. Psychiatry. 27 (2022) 3583–3591. https://doi.org/10.1038/s41380-022-01649-w.

[38] D. Kontis, E. Theochari, Dopamine in anorexia nervosa: A systematic review, Behav. Pharmacol. 23 (2012) 496–515. https://doi.org/10.1097/FBP.0B013E328357E115.

[39] Y. Zhang, Y. Lv, Y. Chen, Y. Li, Y. Wang, H. Zhao, Trimetallic Ag@Pt-Rh core-shell nanocubes modified anode for voltammetric sensing of dopamine and sulfanilamide, Chem. Eng. Sci. 249 (2022) 117326. https://doi.org/10.1016/j.ces.2021.117326.

[40] G.D. Christian, W.C. Purdy, The residual current in orthophosphate medium, J. Electroanal. Chem. 3 (1962) 363–367. https://doi.org/10.1016/0022-0728(62)80012-6.

[41] S. Schindler, T. Bechtold, Mechanistic insights into the electrochemical oxidation of dopamine by cyclic voltammetry, J. Electroanal. Chem. 836 (2019) 94–101.

https://doi.org/10.1016/J.JELECHEM.2019.01.069.

[42] Y. Hanifehpour, M.A. Cheney, S.W. Joo, Sonocatalytic Decolorization of Azo Dye by Ultrasound-Assisted Ytterbium-Substituted Mn2O3 Nanocatalyst, J. Inorg. Organomet. Polym. Mater. 28 (2018) 2143–2153. https://doi.org/10.1007/s10904-018-0881-0.

[43] R. Najjar, R. Awad, A.M. Abdel-Gaber, Physical Properties of Mn2O3 Nanoparticles Synthesized by Co-precipitation Method at Different pH Values, J. Supercond. Nov. Magn. 32 (2019) 885–892. https://doi.org/10.1007/s10948-018-4765-x.

[44] H.U. Shah, F. Wang, M.S. Javed, M.A. Ahmad, M. Saleem, J. Zhan, Z.U.H. Khan, Y. Li, In-situ growth of MnO2 nanorods forest on carbon textile as efficient electrode material for supercapacitors, J. Energy Storage. 17 (2018) 318–326. https://doi.org/10.1016/j.est.2018.03.015.

[45] F. Fina, S.K. Callear, G.M. Carins, J.T.S. Irvine, Structural Investigation of Graphitic Carbon Nitride via XRD and Neutron Diffraction, Chem. Mater. 27 (2015) 2612–2618. https://doi.org/10.1021/acs.chemmater.5b00411.

[46] Y. Zheng, Q. Ruan, J. Ren, X. Guo, Y. Zhou, B. Zhou, Q. Xu, Q. Fu, S. Wang, Y. Huang, Plasma- assisted liquid-based growth of g-C3N4/Mn2O3 p-n heterojunction with tunable valence band for photoelectrochemical application, Appl. Catal. B Environ. 323 (2023) 122170. https://doi.org/10.1016/j.apcatb.2022.122170.

[47] J. Wang, M. Li, M. Qian, S. Zhou, A. Xue, L. Zhang, Y. Zhao, W. Xing, Simple Synthesis of High Specific Surface Carbon Nitride for Adsorption-Enhanced Photocatalytic Performance, Nanoscale Res. Lett. 13 (2018) 1–7. https://doi.org/10.1186/s11671-018-2654-7.

[48] A. Rashidizadeh, H. Ghafuri, H.R. Esmaili Zand, N. Goodarzi, Graphitic Carbon Nitride Nanosheets Covalently Functionalized with Biocompatible Vitamin B1: Synthesis, Characterization, and Its Superior Performance for Synthesis of Quinoxalines, ACS Omega. 4 (2019) 12544–12554. https://doi.org/10.1021/acsomega.9b01635.

[49] K.M. Racik, K. Guruprasad, M. Mahendiran, J. Madhavan, T. Maiyalagan, M.V.A. Raj, Enhanced electrochemical performance of MnO 2 /NiO nanocomposite for supercapacitor electrode with excellent cycling stability, J. Mater. Sci. Mater. Electron. 30 (2019) 5222–5232. https://doi.org/10.1007/s10854-019-00821-3.

[50] S. Zhan, D. Zhu, M. Qiu, H. Yu, Y. Li, Highly efficient removal of NO with ordered mesoporous manganese oxide at low temperature, RSC Adv. 5 (2015) 29353–29361. https://doi.org/10.1039/c4ra17300g.

[51] G. Greczynski, L. Hultman, A step-by-step guide to perform x-ray photoelectron spectroscopy, J. Appl. Phys. 132 (2022) 11101. https://doi.org/10.1063/5.0086359.

[52] G. Periyasamy, I.M. Patil, B. Kakade, P. Veluswamy, J. Archana, H. Ikeda, K. Annamalai, Reduced graphene oxide-wrapped α-Mn2O3/α-MnO2 nanowires for electrocatalytic oxygen reduction in alkaline medium, J. Mater. Sci. Mater. Electron. 33 (2022) 8644–8654. https://doi.org/10.1007/s10854-021-06721-9.

[53] R.A. Fernandes, M.J. Sampaio, E.S. Da Silva, H. Boumeriame, T. Lopes, L. Andrade, A. Mendes, J.L. Faria, C.G. Silva, Sustainable production of value-added chemicals and fuels by using a citric acid-modified carbon nitride optical semiconductor, Appl. Catal. A Gen. 609 (2021) 117912. https://doi.org/10.1016/j.apcata.2020.117912.

[54] S. Baskar, C.W. Liao, J.L. Chang, J.M. Zen, Electrochemical synthesis of electroactive poly(melamine) with mechanistic explanation and its applicability to functionalize carbon surface to prepare nanotube-nanoparticles hybrid, Electrochim. Acta. 88 (2013) 1–5. https://doi.org/10.1016/j.electacta.2012.10.040.

[55] W. Huang, J. Li, Y. Xu, Nucleation and growth of porous MnO2 coatings prepared on nickel foam and evaluation of their electrochemical performance, Materials (Basel). 11 (2018). https://doi.org/10.3390/ma11050716.

[56] S. Nijjer, J. Thonstad, G.M. Haarberg, Oxidation of manganese(II) and reduction of manganese dioxide in sulphuric acid, Electrochim. Acta. 46 (2000) 395–399. https://doi.org/10.1016/S0013-4686(00)00597-1.

[57] L. WEN-ZHI, L. YOU-QIN, H. GUANG-QI, Preparation of Manganese Dioxide Modified Glassy Carbon Electrode By a Novel Film Plating/Cyclic Voltammetry Method for H(2)0(2) Detection, J. Chil. Chem. Soc. 54 (2009) 2–7. https://doi.org/10.4067/s0717-97072009000400009.

[58] M.F. Dupont, S.W. Donne, Nucleation and growth of electrodeposited manganese dioxide for electrochemical capacitors, Electrochim. Acta. 120 (2014) 219–225. https://doi.org/10.1016/j.electacta.2013.12.014.

[59] Z. Ghorannevis, E. Akbarnejad, M. Ghoranneviss, Structural and morphological properties of ITO thin films grown by magnetron sputtering, J. Theor. Appl. Phys. 9 (2015) 285–290. https://doi.org/10.1007/s40094-015-0187-3.

[60] J. Zhao, Z. Tao, J. Liang, J. Chen, Facile synthesis of nanoporous γ-MnO2 structures and their application in rechargeable Li-ion batteries, Cryst. Growth Des. 8 (2008) 2799–2805. https://doi.org/10.1021/cg701044b.

[61] X. Huang, W. Cui, J. Yu, S. Lu, X. Liao, Preparation of Mesoporous MnO2 Catalysts with Different Morphologies for Catalytic Ozonation of Organic

Compounds, Catal. Letters. 152 (2022) 1441–1450. https://doi.org/10.1007/s10562-021-03745-y.

[62] Y. Yang, J. Jia, Y. Liu, P. Zhang, The effect of tungsten doping on the catalytic activity of A-MnO2 nanomaterial for ozone decomposition under humid condition, Appl. Catal. A Gen. 562 (2018) 132–141. https://doi.org/10.1016/j.apcata.2018.06.006.

[63] R.A. Davoglio, G. Cabello, J.F. Marco, S.R. Biaggio, Synthesis and characterization of α-MnO2 nanoneedles for electrochemical supercapacitors, Electrochim. Acta. 261 (2018) 428–435. https://doi.org/10.1016/j.electacta.2017.12.118.

[64] X. Dai, M. Zhang, T. Li, X. Cui, Y. Shi, X. Zhu, P. Wangyang, D. Yang, J. Li, Effect of current on electrodeposited MnO2 as supercapacitor and lithium-ion battery electrode, Vacuum. 195 (2022) 110692. https://doi.org/10.1016/j.vacuum.2021.110692.

[65] S. Sopčić, R. Peter, M. Petravić, Z. Mandić, New insights into the mechanism of pseudocapacitance deterioration in electrodeposited MnO2 under negative potentials, J. Power Sources. 240 (2013) 252–257. https://doi.org/10.1016/j.jpowsour.2013.04.008.

[66] E. Alwin, W. Nowicki, R. Wojcieszak, M. Zieliński, M. Pietrowski, Elucidating the structure of the graphitic carbon nitride nanomaterialsviaX-ray photoelectron spectroscopy and X-ray powder diffraction techniques, Dalt. Trans. 49 (2020) 12805–12813. https://doi.org/10.1039/d0dt02325f.

[67] Y. Liu, S. Zhao, C. Zhang, J. Fang, L. Xie, Y. Zhou, S. Zhuo, Hollow tubular carbon doping graphitic carbon nitride with adjustable structure for highly enhanced photocatalytic hydrogen production, Carbon N. Y. 182 (2021) 287–296.

https://doi.org/10.1016/j.carbon.2021.06.008.

[68] R.D. Crapnell, C.E. Banks, Perspective: What constitutes a quality paper in electroanalysis?, Talanta Open. 4 (2021) 100065. https://doi.org/10.1016/J.TALO.2021.100065.

[69] K. Yadav, S. Garg, A.K. Singh, S. Singh, A. Singh Parmar, Rosy, Protein nano Dots conjugated AuNP, poly-Lysine biointerface for the selective voltammetric estimation of Melatonin in pharmaceutical and food samples, Microchem. J. 179 (2022) 107563. https://doi.org/10.1016/j.microc.2022.107563.

[70] A. Kaliyaraj Selva Kumar, Y. Zhang, D. Li, R.G. Compton, A mini-review: How reliable is the drop casting technique?, Electrochem. Commun. 121 (2020) 106867. https://doi.org/10.1016/J.ELECOM.2020.106867.

[71] W. Abbasi, Electrode Modification Through Chemical and Electrochemical Deposition of Polytyramine Film for Biosensing Application, (n.d.). www.ijert.org (accessed July 30, 2023).

[72] Rosy, R.N. Goyal, Y.B. Shim, Glutaraldehyde sandwiched amino functionalized polymer based aptasensor for the determination and quantification of chloramphenicol, RSC Adv. 5 (2015) 69356–69364. https://doi.org/10.1039/c5ra11131e.

[73] K. Kunpatee, S. Traipop, O. Chailapakul, S. Chuanuwatanakul, Simultaneous determination of ascorbic acid, dopamine, and uric acid using graphene quantum dots/ionic liquid modified screen-printed carbon electrode, Sensors Actuators, B Chem. 314 (2020) 128059. https://doi.org/10.1016/j.snb.2020.128059.

[74] L. Zhang, C. Liu, Q. Wang, X. Wang, S. Wang, Electrochemical sensor based on an electrode modified with porous graphitic carbon nitride nanosheets (C3N4) embedded in graphene oxide for simultaneous determination

of ascorbic acid, dopamine and uric acid, Microchim. Acta. 187 (2020). https://doi.org/10.1007/s00604-019-4081-6.

[75] Y. Chen, X.F. Zhang, A.J. Wang, Q.L. Zhang, H. Huang, J.J. Feng, Ultrafine Fe3C nanoparticles embedded in N-doped graphitic carbon sheets for simultaneous determination of ascorbic acid, dopamine, uric acid and xanthine, Microchim. Acta. 186 (2019) 1–9. https://doi.org/10.1007/s00604-019-3769-y.

[76] W. Zhu, A. Zhu, Y. Shu, GNP/CNT nanocomposite coated screen-printed electrode for point-of-care testing of dopamine in human serum, Prog. Org. Coatings. 170 (2022) 106983. https://doi.org/10.1016/j.porgcoat.2022.106983.

[77] A. Kader Mohiuddin, M. Shamsuddin Ahmed, S. Jeon, Palladium doped α-MnO2 nanorods on graphene as an electrochemical sensor for simultaneous determination of dopamine and paracetamol, Appl. Surf. Sci. 578 (2022) 152090. https://doi.org/10.1016/j.apsusc.2021.152090.

[78] M. Gu, H. Xiao, S. Wei, Z. Chen, L. Cao, A portable and sensitive dopamine sensor based on AuNPs functionalized ZnO-rGO nanocomposites modified screen-printed electrode, J. Electroanal. Chem. 908 (2022) 116117. https://doi.org/10.1016/j.jelechem.2022.116117.

[79] H. Li, Z. Deng, Z. Jiao, R. Zhu, L. Ma, K. Zhou, Z. Yu, Q. Wei, Engineering a Au-NPs/Nafion modified nanoporous diamond sensing interface for reliable voltammetric quantification of dopamine in human serum, Chem. Eng. J. 446 (2022) 136927. https://doi.org/10.1016/J.CEJ.2022.136927.

[80] M. Cui, P. Xin, Z. Che, M. Zou, M. Zhang, X. Sun, Y. Yuan, Z. Zou, G. Lv, S. Wang, W. Hu, Highly anti-interference electrocatalytic sensing for dopamine with nitrogen-doped graphdiyne directly in biofluids, Chem. Eng. J. 464 (2023) 142629. https://doi.org/10.1016/J.CEJ.2023.142629.

[81] Y. Zhang, H. Wang, L. Jiao, N. Wu, W. Xu, Z. Wu, Y. Wu, P. Hu, W. Gu, C. Zhu, Defect engineering of PdMo metallene for sensitive electrochemical detection of dopamine, Chem. Eng. J. 466 (2023) 143075. https://doi.org/10.1016/J.CEJ.2023.143075.

[82] V. Mishra, A. Krishnapandi, B. Arumugam, S.C. Kim, Flexible non-invasive sensor for neurotransmitter monitoring inspired by AgBiS2/PEDOT:PSS, Chem. Eng. J. 476 (2023) 146591. https://doi.org/10.1016/J.CEJ.2023.146591.

[83] Rosy, F. Singh, R.N. Goyal, Structural and electrochemical characterization of carbon ion beam irradiated reduced graphene oxide and its application in voltammetric determination of norepinephrine, RSC Adv. 5 (2015) 87504–87511. https://doi.org/10.1039/c5ra17909b.